DISTRIBUTION STATEMENT A
Approved for public release;
Distribution Unlimited

GaInAsP-InP Double Heterostructure Lasers on Si Substrate Grown by LP-MOCVD

ONR Contract # N00014-93-1-0176

1993

Principal Investigator: Manijeh Razeghi

Center for Quantum Devices
Northwestern University, Evanston, IL 60208

Personnel:

K. Mobarhan	(completed Ph.D. in 1994)
J. Diaz	(completed Ph.D. in 1997)
I. Eliashevich	(completed Ph. D in 1997)

Technology Transfer:

E. Kolev	(currently at SDL)
R. Sudharsanan	(currently at SPIRE Corp.)

DTIC QUALITY INSPECTED 2

Final Report

19970616 061

CONTENTS

List of Tables and Figure iv

1 **Introduction** **3**

- 1.1 Preview 3
- 1.2 Fundamentals of III-V epitaxy on Si substrate 8

2 **MOCVD Growth and Material Characterization of InGaAsP-InP Double Heterostructure on Si** **15**

- 2.1 Optimum growth parameters of the laser structure 15
- 2.2 Structural characterization 17
- 2.3 Photoluminescence measurements 21

3 **Laser Diode Processing and Fabrication** **27**

- 3.1 Introduction 27
- 3.2 Preparation of broad area lasers by direct patterning 27
- 3.3 Processing of broad area lasers using the liftoff process 31
- 3.4 Fabrication of double channel ridge lasers 35
  - 3.4.1 Chemical etching of the channels 35
  - 3.4.2 Dielectric passivation using SiO_2 37
  - 3.4.3 Opening of windows in the SiO_2 layer using reactive ion etching 38
- 3.5 Lapping and polishing of the Si substrate 43
- 3.6 Annealing 46

3.7 Scribing and cleaving 46

3.8 Development of heat sink and packaging technology 50

4 Characterization of Broad Area Lasers and Analysis of the Results 57

4.1 Preview 57

4.2 Analysis of Light versus Current Curve 57

4.2.1 Experimental setup and procedure 57

4.2.2 Threshold current density

4.2.3 Output light versus injection current curve 64

4.2.4 External differential quantum efficiency 66

4.3 Temperature Sensitivity of the Threshold Current and External Differential Quantum Efficiency 70

4.3.1 Calculation of the characteristic temperature T_O of a laser operating under pulse condition 70

4.3.2 Temperature dependency of Jth and h_d 73

4.3.3 Effect of intervalence band absorption 75

4.3.4 Auger recombination process 76

4.3.5 Heterojunction leakage mechanism 79

4.4 Longitudinal Spectrum Analysis 82

4.4.1 Experimental measurement setup 82

4.4.2 Mode spacing 84

4.4.3 Multimode rate equations 86

4.4.4 Gain spectrum 87

4.4.5 Shape of the spectral envelope 89

4.4.6 Spectral linewidth 92

4.4.7 Linewidth enhancement factor 95

4.4.8 Effects of temperature on the longitudinal spectrum 96

4.5 Observation of the near field emission pattern 97

Summary **101**

References **105**

Appendix A: List of Symbols **115**

Appendix B: List of Publications **118**

List of Tables and Figures

Table 1.1 First experimental device results of GaAs on Si. 6

Table 1.2 First experimental device results of InP on Si 7

Table 1.3 Comparison of the physical properties of GaAs and InP with Si. 8

Table 2.1 Optimum growth parameters. 16

Figure 1.1 Schematic diagram showing two types of dislocation at the interface of GaAs and Si. In the first type the Burgers vector, shown with an arrow, is parallel to the epilayers while in the second type the vector is at an angle. 10

Figure 1.2a The diamond crystal structure. 11

Figure 1.2b The zincblende crystal structure. 12

Figure 1.3 Schematic representation of the anti phase boundaries (APB) at the interface of GaAs layer and Si substrate. In the above diagram, for clarity, the lattice mismatch between GaAs and Si has not been shown. 13

Figure 2.1 Electrochemical doping profile of the epitaxial layers. 17

Figure 2.2 Schematic representation of the ball polishing technique. The thickness of each epilayer is determined by measuring the diameters d1, d2, and d3 of the circular bevels under the microscope and relating these to the diameter of the steel ball which is known to be exactly 4 mm. 18

Figure 2.3 Top view of the circular bevels under the microscope at a magnification of 200. 19

Figure 2.4. High resolution x-ray diffraction showing lattice matching between the quaternary layers. The inset shows the FWHM of the peaks given in units of arc seconds. The intensity is indicated in counts per second (cps). 20

Figure 2.5 Photoluminescence spectra of the laser structure before the removal of the contact layer. The only peak observed at any temperature is the one due to the InGaAs. 22

Figure 2.6 Room temperature photoluminescence spectrum peaks at a wavelength of 1.35 μm with a FWHM of 75 meV. The inset shows the schematic of the structure and the thickness of each layer after the 0.4 μm InGaAs contact layer was removed. 23

Figure 2.7 Photoluminescence spectra at four different temperatures ranging from 4 to 200 K. 24

Figure 2.8 Schematic diagram showing excess carrier concentration in the InP layer and diffusion into the neighboring InGaAsP layer at temperatures of (I) 4 K and (II) 300 K. 25

Figure 3.1 The laser after the AuZn/Au metalization contact has been deposited and patterned on the epilayer side of the sample. 30

Figure 3.2 Sample after deposition of Au layer used as passivation through formation of a Schottky barrier. 31

Figure 3.3 a) deposition of Ti/Pt/Au layers over patterned photoresist layers, b) lift-off of preselected regions of metalization through chemical treatment of the sample, c) etching of the InGaAs contact layer. 33

Figure 3.4 Top view photograph showing the 20 μm wide Ti/Pt/Au stripes deposited on the p-side surface of the sample and patterned using a liftoff process. 34

Figure 3.5 The different steps involved in etching of the double channels a) deposition of a 1 μm thick positive photoresist layer, b) exposure with UV light, c) development of double channels in the photoresist, d) chemical etching of the cap and cladding layers. 36

Figure 3.6 The top view of the double channels etched in the sample and the wafer then coated with about 6000 Å SiO_2 using PECVD method. The width of the channels shown in this photo is 10 μm with a separation of about 10 μm. 36

Figure 3.7 The steps involved in opening of a window over the SiO_2 coated ridge. a) deposition of about 6000 Å of SiO_2 using the PECVD method, b) deposition of 1 μm thick positive photoresist layer, c) exposure with UV light, d) development of the photoresist and finally the etching of the SiO_2 layer using RIE technique. 40

Figure 3.8.a Top view of the sample showing a window etched through the SiO_2 covered ridge using RIE method. The width of the channels is 10 μm. 40

Figure 3.8.b Cross section view of the double channels showing the etched window in the SiO_2 layer. The cross section photo is taken under the same magnification as the top view photo. 41

Figure 3.9 Deposition of metal contacts on the two sides of the sample in addition to lapping and polishing down to a thickness of about 50 μm results in a final product schematically shown here. 42

Figure 3.10 The laser sample wax bonded onto a glass puck as a preparation to lapping and polishing. 44

Figure 3.11 Schematic diagram showing the polishing jig positioned over the rotating disk during the lapping procedure. The container at the top contains the abrasive solution. Aluminum oxide powder mixed with water is used for lapping and sodium hydrochloride solution is used for polishing. 45

Figure 3.12 a) Approximately 50 μm long scribe lines are scratched at the edge of the sample, b) Application of pressure cleaves the sample along the scribe lines. 47

Figure 3.13 Schematic diagram of the scribing machine followed by the list of different parts. 48

Figure 3.14 Schematic structure of InGaAsP/InP surface emitting laser with vertical and 45° mirrors created by reactive ion beam etching. 50

Figure 3.15 Schematic diagram showing the details of the system used to bond a laser diode onto the surface of an indium coated heatsink. 53

Figure 3.16 The schematic representation of the die bonding machine followed by the list and description of various parts. The details of the ceramic capillary system used to pick up the die is shown in the previous figure. 54

Figure 3.17 Scribing and cleaving into individual diodes and mounting them on indium coated heat sinks results in a package suitable for efficient removal of excess heat. 56

Figure 4.1 Experimental setup for measurement of the output light power of laser diodes emitting at 1.3 μm wavelength. An integrating sphere equipped with a germanium detector is used to collect the light in order to ensure optimum measurement. The laser probe station is equipped with a thermoelectric cooler-heater for temperature adjustment. 59

Figure 4.2 Pulsed (100ns-5kHz) light-current characteristic for a 170 μm long (20 μm side stripe) laser with both facets as cleaved. Output power exceeds 200 mW per facet. The inset shows the laser structure. 60

Figure 4.3 The threshold current density J_{th} versus the inverse cavity length 1/L for lasers with cavity lengths between 95 μm and 590 μm. 63

Figure 4.4 The cavity length dependence of the inverse external differential quantum efficiency. The extrapolated internal quantum efficiency is 33 % and the internal loss is 39 cm^{-1}. 82

Figure 4.5 Light-current characteristic for a 95 μm long (20 μm wide stripe) broad area laser at various temperatures ranging from 15 °C up to 75 °C. 71

Figure 4.6 Variations of J_{th} with rising temperature for a 95 μm long laser operating under pulse condition. The solid line is a linear fit and from its slope T_o is deduced. 73

Figure 4.7 Absorption of emitted photons by transitions from the split-off band into the heavy hole band at energy E_1. This absorption is referred to a_1. The transition into the acceptor level at energy E_A is referred to as a_2. 75

Figure 4.8 Three different band to band processes shown schematically. Electrons are represented by closed circles and holes by open circles. 77

Figure 4.9 Schematic bandgap diagram showing the electron and hole leakage currents over the heterobarrier. 80

Figure 4.10 The experimental setup used in driving the laser diode and measuring its output light spectrum. 83

Figure 4.11 Lasing spectrum of a 170 μm cavity length laser operating at slightly above threshold. The peak wavelength is at 1.357 μm. 84

Figure 4.12 The illustration of gain spectrum indicating the gain peak and the cavity loss level. 88

Figure 4.13 Experimental setup for observation of laser diode near field emission pattern and the list of components. 98

Figure 4.14 Stimulated emission near field pattern of a 1.3 μm laser. The intensity profile is measured along theline passing through the emission pattern. The position and the tilt of this line can be adjusted using the video analyzer. 100

GaInAsP-InP Double Heterostructure Lasers on Si Substrate Grown by LP-MOCVD

Principle Investigator: Manijeh Razeghi

ONR Contract number: N00014-93-1-0176

This report summarizes the results of experimental research work on material, processing technology, and laser characterization performed at the Center for Quantum Devices under ONR contract #N00014-93-1-0176 "GaInAsP-InP double heterostructure lasers on Si substrate grown by MOVCD". In order to achieve this goal of the contract, the CQD research group split the divided research work into three phases (with specific tasks) : Material Growth, and Laser Processing and Laser Characterization. The first phase consists of different approaches in order to increase the quality of the buffer layer and laser material. The second phase consists of the fabrication laser structure on Si substrates based on the peculiarities of structures containing residual structural stress and moderate levels of dislocation density. The third phase consists of the laser characterization of these laser diodes. Each phase contains specific tasks that was used in a systematic way to achieve GaInAsP-InP double heterostructure lasers on Si substrate.

Phase 1: (1st year)

- Growth of GaInAsP films
- Growth of InP confinement layers
- Growth of double heterostructure GaInAsP-InP laser structures
- Demonstration of double heterostructure GaInAsP-InP

Phase 2: (1st and 2nd year)

- Growth of laser device structure without superlattice buffer layer
- Characterization of laser structure
- Fabrication of Laser Diodes
- Measurement of laser device characteristics

Phase 3: (2nd and 3rd year)

- Fabrication of Ridge Structures laser diodes

- Measurement of laser device characteristics
- Optimization of device design
- Optimization of fabrication procedures
- Demonstration of cw 1.3 μm laser on Si substrate

In the following Chapters, we will explain in detail the amount of significant work that was done on this ONR contract and the realization of future payoffs that these lasers can accomplish.

CHAPTER 1

Introduction

1.1 Preview

Semiconductor lasers emitting in the range of 1.3 μm up to 1.55 μm wavelength are important sources of light due to their application in fiber optics telecommunication networks using silica fibers. This is due to the fact that the wavelengths of 1.3 μm and 1.55 μm correspond respectively to zero dispersion and minimum attenuation windows of modern silica-based fibers. To achieve emission at these wavelengths InGaAsP/InP material system has been shown to be suitable. In fact InGaAsP quaternary material lattice matched to InP can be used to fabricate semiconductor lasers operating anywhere in the wavelength range of 1.11.65 μm. For example lasers with active layer consisting of $In_xGa_{1-x}As_yP_{1-y}$ with x=0.8 and y=0.6 are expected to emit at 1.3 μm wavelength. These quaternary materials are usually grown lattice-matched on an InP substrate. Pulsed operation of a 1.1 μm InGaAsP laser was first reported in 1975 [1]. In 1976 through the application of stripe geometry the first room temperature continuous wave operation of InGaAsP/InP double heterostructure lasers were reported by Hsieh and Rossi [2] followed by lasers emitting at the desired wavelength of 1.3 μm in 1977 [3].

The double heterostructure is used in order to minimize the loss of carriers from the active region of the laser where stimulated emission takes place due to population inversion. It also provides a means to achieve optical mode confinement and stable fundamental mode operation in the vertical direction (direction of the growth of the epilayers). To achieve even further improvement in carrier and mode confinement in addition to higher output powers more sophisticated structures have been used in which carriers and optical wave are also confined laterally (direction parallel to the growth). These include buried heterostructure, buried ridge stripe structure, V-grooved inner stripe structure, and etc. [4-9].

So far most of such lasers have been grown on InP substrates [4-10] but recently interest has risen in growing these structures on Si substrate instead. In this way it is possible to benefit from the advantages offered by Si which include mechanical strength, high thermal conductivity, the possibility of growth on large diameter substrates and the realization of optoelectronic integrated circuits (OEIC's) entirely on Si substrate.

However, despite much research [11-17], the growth of III-V compounds on silicon is still a difficult task. This is mostly due to the difference in lattice parameter and lattice symmetry between III-V semiconductors and Si and to the problems caused by different thermal expansion coefficients. These problems have been reduced by the use of superlattices between the two semiconductors. These superlattices have been shown to be effective in bending dislocation lines out toward the edges of the crystal, preventing both the cross doping of the epilayer with the Si and dislocation movement in device operation. In 1988 the use of such superlattices led to the first continuous wave room-temperature operation of InGaAsP / InP lasers emitting at 1.3 μm on Si substrate [17]. More recently room temperature operations of GaInAsP double heterostructure [18] and multiple quantum well [19] lasers emitting at 1.5 μm on Si substrate have been reported. In the latter two works, a 13 μm thick InP layer was used in addition to a superlattice in order to further reduce the dislocation spreading. However, very thick buffer layers are not very practical means of obtaining low-cost and easily mass produced optoelectronic devices on Si substrates. In this work a 1.35 μm wavelength InGaAsP / InP double heterostructure has been grown directly on silicon without the use of any superlattice buffer layer. The realization of a reliable laser diode on a Si substrate is an important step towards the industrial development of low cost optical devices on Si substrates and the development of III-V OEIC's on Si. The details of material growth and characterization [20] in addition to laser diode processing and device characterization results [21] are presented further in chapters 2 and 3.

Various growth techniques have been used to fabricate high performance InGaAsP / InP double heterostructure and quantum well lasers emitting in the range of 1.3-1.5 μm. In the growth of these structures low pressure MOCVD is the best method mainly due to the fact that it improves the abruptness of the heterointerfaces and also the material homogeneity over large substrates, in addition to reduction of gas phase parasitic reactions. At very low pressures; down to 10^{-4} Torr, the reactant chemicals begin to be transported in the form of molecular beams rather than gas flows. This results in the technique of Chemical Beam Epitaxy (CBE) which compared to low pressure MOCVD has a lower consumption of chemicals. This growth technique can be also used to efficiently fabricate multiple quantum well lasers emitting at 1.3 μm and 1.55 μm.

Historically the first III-V material based devices grown on Si substrate were those of GaAs on Si as shown in table 1.1. This has been mainly due to the fact that GaAs has only about a 4 % lattice mismatch with Si compared to the InP which has an 8 % lattice mismatch with Si. As a result the problems associated with III-V material epitaxy on Si are less severe in the case of GaAs devices than InP based devices which appeared relatively more recently as shown in table 1.2. These issues and other problems will be elaborated in the next section.

Device	Structure	Growth Method	Reference
LED	GaAs/Ge/Si	MBE	Shinoda et. al. 1983 [22]
DH Laser	GaAs/AlGaAs/Si	MBE	Windhorn et. al. 1984 [23]
SLS Laser	InGaAs/AlGaAs	MOCVD	Choi et. al 1991 [24]
p-i-n Photodiode	GaAs/Si	MBE	Paslaski et. al. 1988 [25]
MESFETs	GaAs/Ge/Si	MBE	Choi et. al 1984 [26]
MODFETs	GaAs/AlGaAs/Si	MBE	Fischer et. al. 1986 [27]
Bipolar Transisitor	GaAs/Si	MBE	Fischer et. al. 1985 [28]
Solar Cell	GaAs/Ge/Si	MOCVD	Gale et. al. 1987 [29]
Modulator	AlGaAs/GaAs/Si	MBE	Dobbelaere et. al. 1988 [30]
Waveguide	GaAs/AlGaAs/Si	MBE	Kim et. al. 1990 [31]

Table 1.1 First experimental device results of GaAs on Si

Device	Structure	Reference
LED at RT	InGaAsP/InP/Si $\lambda = 1.15\,\mu m$	Razeghi et. al. 1987 [32]
DH Laser	InGaAsP/InP/Si $\lambda = 1.3\,\mu m$	Razeghi et. al. 1988 [16]
BRS CW Laser	InGaAsP/InP/Si $\lambda = 1.3\,\mu m$	Razeghi et. al. 1988 [17]
p-i-n Photodiode	InGaAs/InP/Si	Razeghi et. al. 1989 [33]
Waveguide	MQW InGaAs/InP/Si $\lambda = 1.5\,\mu m$	Razeghi et. al. 1989 [11]
Solar Cell	InP/Si	Yamaguchi et. al. 1987 [34]
Bipolar Transistor	InGaAs/InP/Si	Makimoto et. al. 1991 [35]
Heterojunction Phototransistor	InGaAs/InP/Si	Aina et. al. 1991 [36]
MQW Laser at RT	InGaAs/InGaAsP/Si	Sugo et. al. 1991 [19]

Table 1.2 First experimental device results of InP on Si

1.2 Fundamentals of III-V Epitaxy on Si Substrate

The eventual goal is to integrate optoelectronic devices with the already well established silicon integrated circuit technology resulting in Opto-Electronic Integrated Circuits generally referred to as OEIC's. The first step towards the realization of OEIC's is the successful fabrication of one laser on Si substrate in a simple and mass reproducible manner.

Epitaxy on Si has many advantages. In figure 1.1 some of the properties of Si are compared to GaAs and InP which are the two important compounds used in optoelectronic devices.

	Si	GaAs	InP
Thermal coefficient of expansion (K^{-1})	2.6×10^{-6}	5.7×10^{-6}	4.56×10^{6}
Thermal conductivity ($W\ cm^{-1}\ K^{-1}$)	1.5	0.46	0.68
Lattice parameter (Å)	5.43	5.65	5.86
Crystal symmetry	Diamond	Zinc Blende	Zinc Blende
Density (g / cm^3)	2.328	5.32	4.787

Table 1.3. Comparison of the physical properties of GaAs and InP with Si

One advantage of growing lasers on Si substrate is the enhanced heat removal capability that results from the higher thermal conductivity of Si. The thermal conductivity of Si is about three times as high as that of GaAs and about two times as high as that of InP. This means that lasers grown directly on Si substrate will be able to dissipate their excess heat easier and thus their operation, in particular at high temperatures, will be improved. Si also has a lower density and weighs about half as much as either GaAs or InP. In addition Si substrate offers a much higher mechanical strength than GaAs and InP. Another advantage of using Si is the possibility of growing structures on large diameter substrates.

Even though growth of III-V based compounds suitable for optoelectronic device fabrication on Si offers many advantages it is by no means an easy task. From table 1.3 it can be noticed that there exists a lattice mismatch between Si and GaAs and InP. Si has approximately a 4 percent and 8 percent lattice mismatch with GaAs and InP respectively. This lattice mismatch makes the epitaxy of III-V material on Si very problematic due to the dislocations that are generated at the interface of the material with different lattice constants. Figure 1.1 shows a schematic representation of such dislocations. These dislocations in themselves are not the cause of the problem, in fact it is their propagation upward through the active layer that results in poor device performance. In laser structures these threading dislocations often reach all the way to the active layer and by serving as nonradiative recombination centers result in high threshold current density and poor quantum efficiency in addition to short device lifetime. This is why up to now it has been necessary to grow a superlattice structure to serve as a buffer layer. The superlattice essentially deflects the threading dislocations in the direction parallel to the layer interface and considerably reduces their density in the active layer. In addition to the superlattice structure some groups also have used a very thick InP buffer layer to further reduce the number of the dislocations which thread their way to the active layer. However, as mentioned earlier, superlattices and very thick buffer layers are not suitable when the objective is to grow optoelectronic devices monolithically on Si integrated circuits at low cost. For this purpose the structure and fabrication of the device must be simple and feasible enough as to make them mass reproducible and at the same time reliable and cheap.

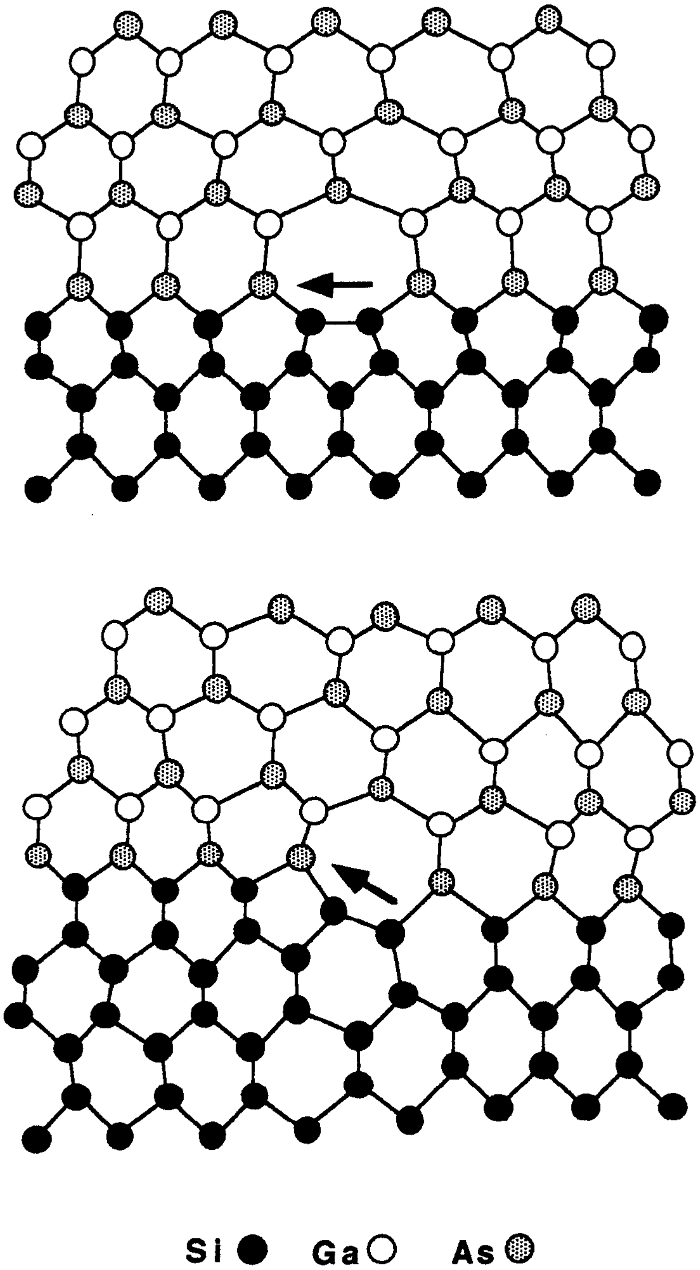

Figure 1.1 Schematic diagram showing two types of dislocation at the interface of GaAs and Si. In the first type the Burgers vector, shown with an arrow, is parallel to the epilayers while in the second type the vector is at an angle.

Another problem associated with the growth of III-V material on Si is the difference in the coefficient of thermal expansion between the two types of crystal. This difference in thermal expansion coefficients result in the GaAs and InP and Si all to expand different amounts when the whole laser structure is subjected to changes of temperature. This could result in small micro cracks forming at the substrate-epilayer interface which, similar to dislocations and defects, can results in an increase in the number of non radiative recombination centers. As a result great care has to be taken when introducing changes of temperature either during growth or during alloying and annealing cycles.

The lattice mismatch between Si and GaAs and InP is a big problem. However the symmetry of the crystals themselves is not the same either. Si has diamond type crystal structure in contrast to GaAs and InP which both have zincblende type crystal structure. The two types of crystal are shown in figures 1.2a and 1.2b.

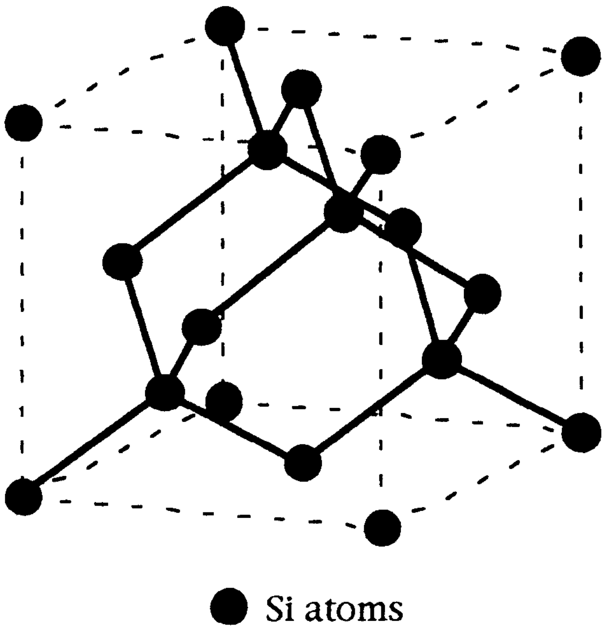

Figure 1.2a The diamond crystal structure.

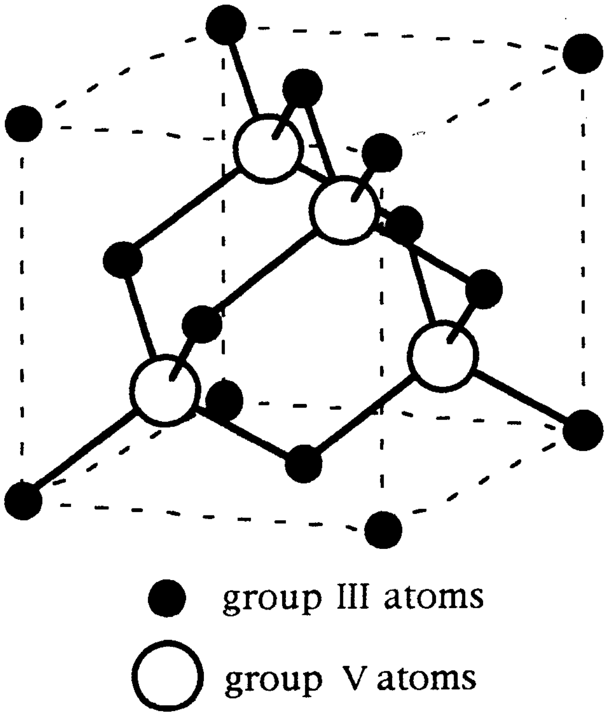

Figure 1.2b The zincblende crystal structure.

When attempting to grow GaAs or InP on Si this difference in symmetry results in the so called antiphase boundaries (APB). These boundaries consist of bonds between two like atoms, for example As-As or Ga-Ga bonds, and typically their formation is very uncontrollable and once appeared in the structure serve as strong scattering centers. Figure 1.3 shows a schematic representation of this situation.

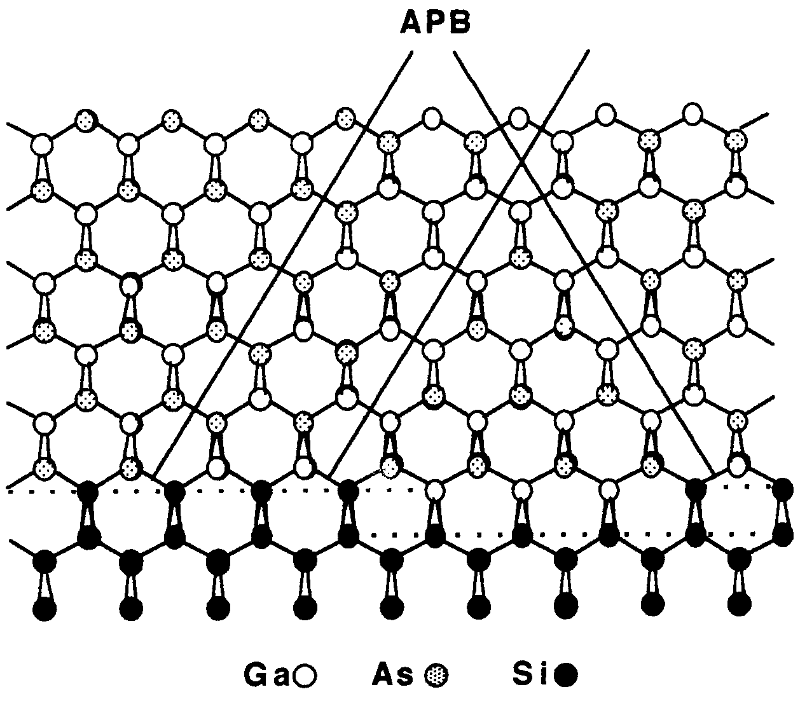

Figure 1.3 Schematic representation of the anti phase boundaries (APB) at the interface of GaAs layer and Si substrate. In the above diagram, for clarity, the lattice mismatch between GaAs and Si has not been shown [37].

As shown in figure 1.3 the presence of monolayer high steps can lead to the formation of antiphase boundaries. In addition it is also possible that antiphase boundaries are formed on an ideal Si surface that has no steps due to nonuniformities on the initial monolayer. In some cases two different antiphase boundaries can mutually annihilate each other resulting in a growth free of antiphase boundaries. This can happen usually on Si surfaces with an exact (100) orientation which have single steps. This mutual annihilation effect is also shown in figure 1.3.

Surface contamination of Si substrate is one cause of antiphase domain formation. It is possible to reduce the antiphase domains by chemically treating the substrate surface prior to epitaxy. For example a powerful oxidant solution such as H_2S0_4 mixed with H_2O_2 could be used to remove the organic contaminants on the substrate surface through oxidation. Simultaneously this process oxidizes the Si surface also. This layer of oxide can then be either removed with HF acid or left as a protective layer until the sample is loaded in the reactor chamber. At that time, immediately before beginning of growth, the sample can be heated to about 1000 ^{o}C to remove this oxide.

The three main problems associated with epitaxial growth of III-V material on Si are summarized below.

(1) The difference of lattice parameter between III-V semiconductors and Si substrate

(2) The difference of lattice symmetry causing antiphase boundaries

(3) The difference of thermal expansion coefficient

In order to increase the crystalline quality of the heterostructure sample and minimize the damage caused due to the above problems great attention must be paid to cleaning and preparation of the substrate surface and optimization of the heating cycles and other growth conditions during the duration of the epitaxial growth process. The optimum growth parameters are presented in the following chapter.

CHAPTER 2

MOCVD Growth and Material Characterization of InGaAsP-InP Double Heterostructure on Si

2.1 Optimum growth parameters

In this work [20] the epilayers were grown by low pressure metalorganic chemical vapor deposition (LP-MOCVD) on (100) silicon (n+) coated with GaAs by the Kopin Corporation. The growth process was carried out at 76 Torr in a horizontal reactor with a substrate temperature of 550 °C. Trimethylindium (TMI) and Triethylgallium (TEG) were used as sources of In and Ga, while pure arsine (AsH_3) and phosphine (PH_3) were used to provide As and P. Hydrogen (H_2) was used as a carrier gas. Silane (SiH_4) and diethylzinc (DEZn) were used as n-type and p-type dopants. The optimum growth parameters are shown in table 2.1.

The structure of the multi-layer, such as shown in the inset of figure 3, includes (i) a 3 μm thick InP cladding layer doped with Si (N_D-N_A≈2.8×10^{18} cm^{-3}), (ii) a 2000 Å thick undoped $Ga_{.0.2}In_{0.8}As_{0.6}P_{0.4}$ quaternary active layer, (iii) a 1 μm thick Zn doped InP cladding layer (N_A-N_D≈2.5×10^{17} cm^{-3}), (iv) and a .0.4 μm Zn doped $In_{0.53}Ga_{0.47}As$ contact layer (N_A-N_D≈$2.3\times10^{19}$$cm^{-3}$).

Figure 2.1 shows the electrochemical doping profile of this structure. Precise control of the doping, such as shown here, is very important to achieving complete confinement of the carriers in the active layer,

Parameters	InP	$\underbrace{Ga_{0.2}In_{0.8}As_{0.6}P_{0.4}}$ ↓	$In_{0.53}Ga_{0.47}$ A
Growth temperature (^{o}C)	550	550	550
Total flow (H_2) (lit. / min.)	4	4	4
H_2 -TMI bubbler flow (cm^3 / min.)	150	150	250
H_2 -TEG bubbler flow (cm^3 / min.)	-	60	150
PH_3 flow (cm^3 / min.)	400	400	-
AsH_3 flow (cm^3 / min.)	-	21	60
Growth rate (Å / min.)	100	150	200
Growth pressure (Torr)	76	76	76

Table 2.1. Optimum growth parameters

which results in improved optical and electrical performance. It can be noticed that the doping concentration on the n-side is approximately ten times higher than the doping concentration on the p-side. The reason for this is to prevent Zn diffusion from the p-type doped region into the n-type doped region which would lead to the undesirable effect of shifting the p-n junction away from the active layer.

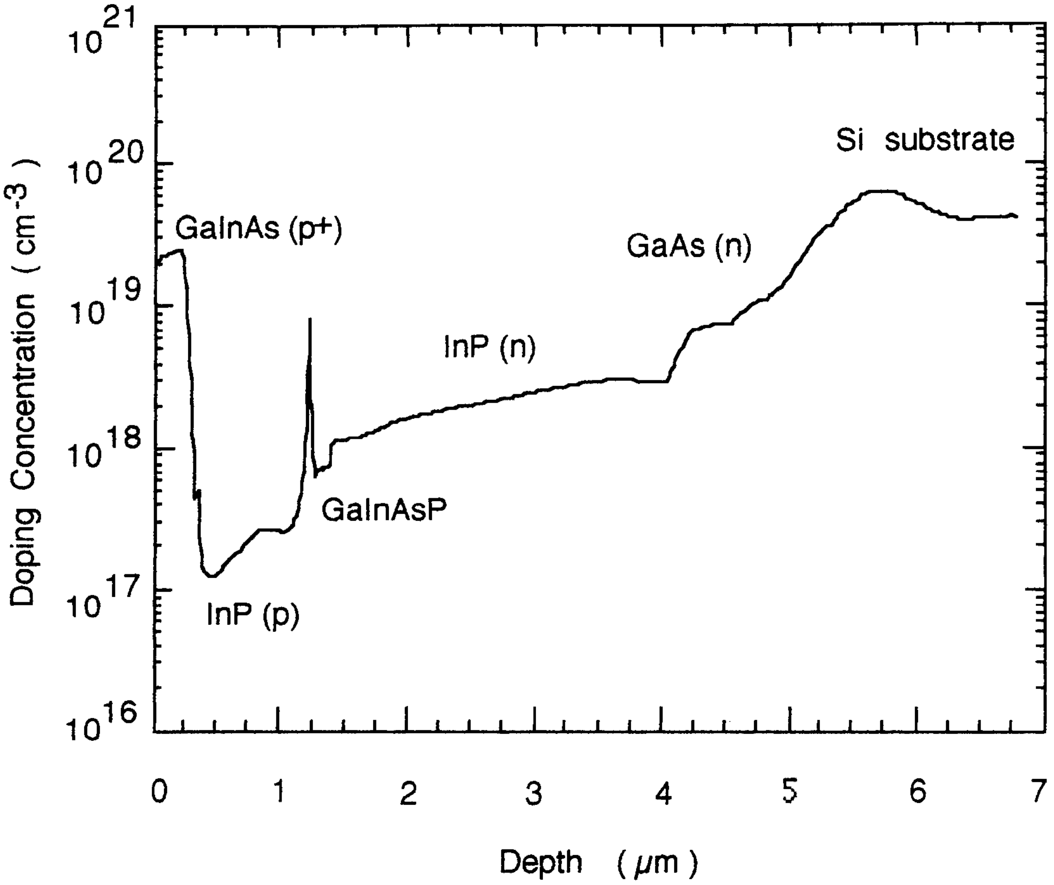

Figure 2.1 Electrochemical doping profile of the epitaxial layers

2.2 Structural characterization

The structure of the epilayers was revealed through a ball polishing thickness measurement technique. To measure thickness by this method, a 4 mm diameter steel ball is brought in contact with the sample and then rotated at high speed, mechanically polishing the sample and creating a circular hole as shown schematically in figure 2.2. A fine diamond paste is used as an abrasive compound. The circular bevel created in this manner is then observed under the microscope, as shown in figure 2.3, and from simple geometrical relationships the thickness of the layers can be calculated to very high accuracy. This is a very quick and highly accurate technique. The layer thicknesses were also measured using a scanning electron microscope and the results obtained were the same as those of the polishing method.

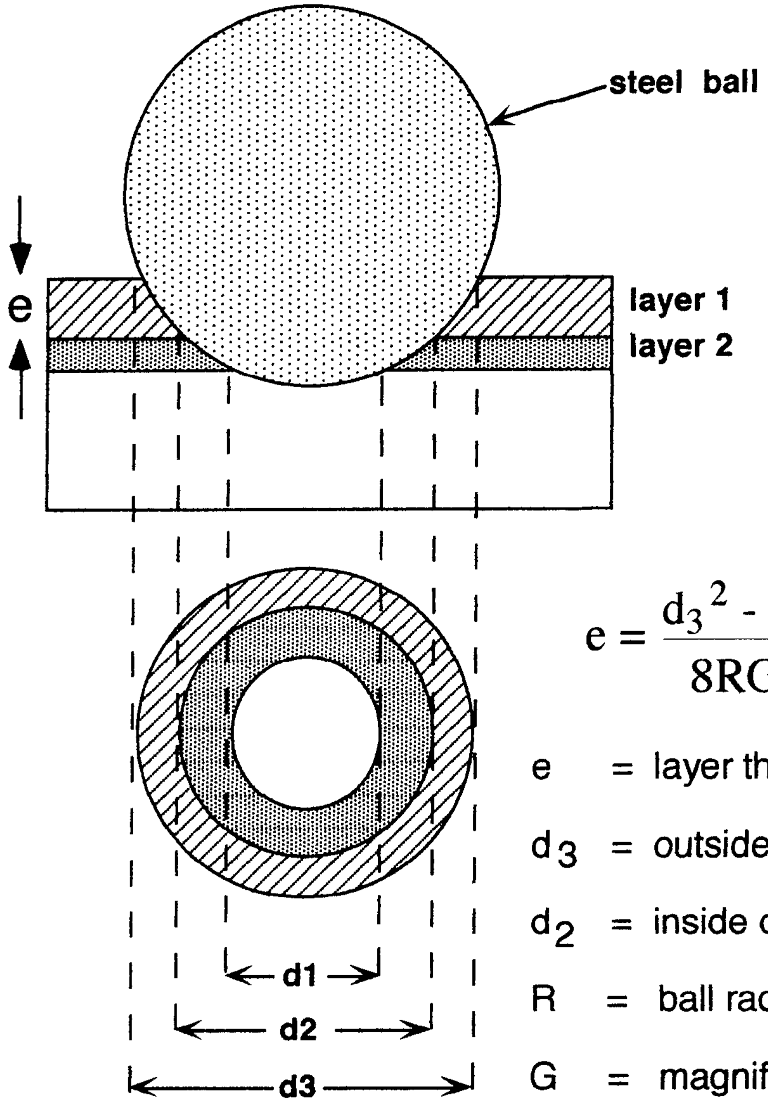

$$e = \frac{d_3{}^2 - d_2{}^2}{8RG^2} \times 1000$$

e = layer thickness in μm

d_3 = outside diameter in mm

d_2 = inside diameter in mm

R = ball radius in mm

G = magnification

Figure 2.2 Schematic representation of the ball polishing technique. The thickness of each epilayer is determined by measuring the diameters d1, d2, and d3 of the circular bevels under the microscope and relating these to the diameter of the steel ball which is known to be exactly 4 mm.

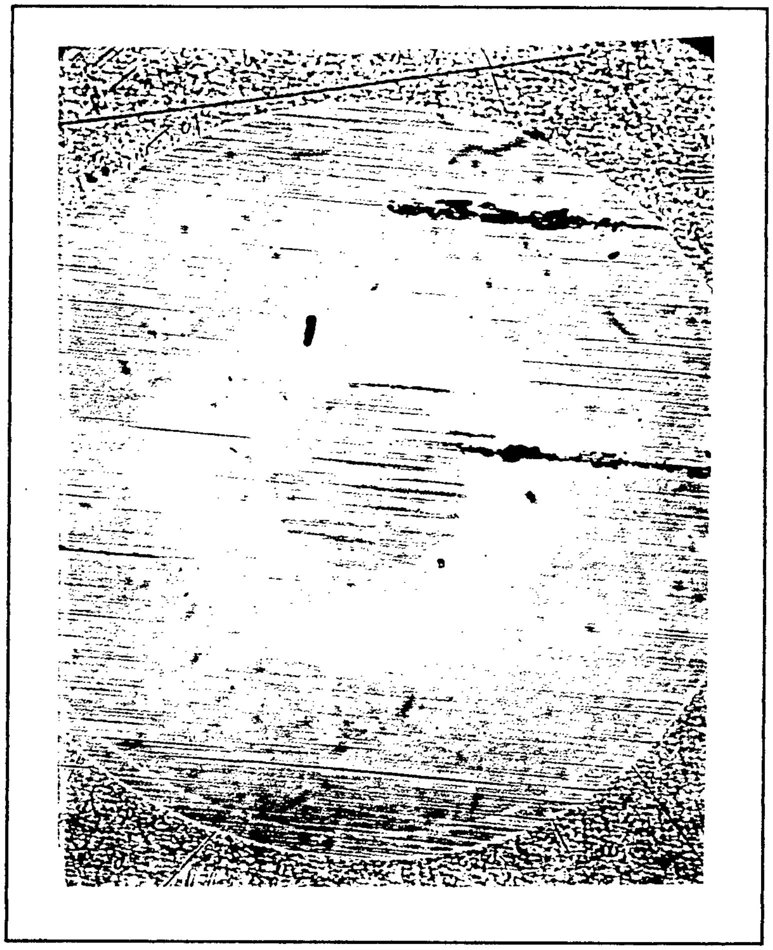

Figure 2.3 Top view of the circular bevels under the microscope at a magnification of 200.

The quality of the crystal structure and the composition of GaInAs (contact layer), and GaInAsP (active layer) was inspected from the X-ray diffraction pattern of the sample. This was done using a five crystal monochrometer Phillips MPD 1880 / High-Resolution X-ray machine. This spectrum is shown in Figure 2.4. X-ray diffraction spectrum indicates a full width at half maximum (FWHM) for the (004) InGaAsP-InP-InGaAs epilayers of 441 arc seconds. This is the evidence for good crystallinity and precise control in the composition of the quaternary layer compounds resulting in very good lattice matching to InP and InGaAs. The dislocation densities of the films were calculated using the relation [38]:

$$D = \beta^2 / 9b^2$$

where D is the actual dislocation density and ß is the FWHM in radians. The parameter b is related to the lattice constant (a) of the material through b=a.√2 for 60° dislocations. We obtain D=2.8x10^7 cm^{-2} for GaAs film with FWHM of 261 arc seconds and D=7.3x10^7 cm^{-2} for InP film with FWHM of 441 arc seconds.

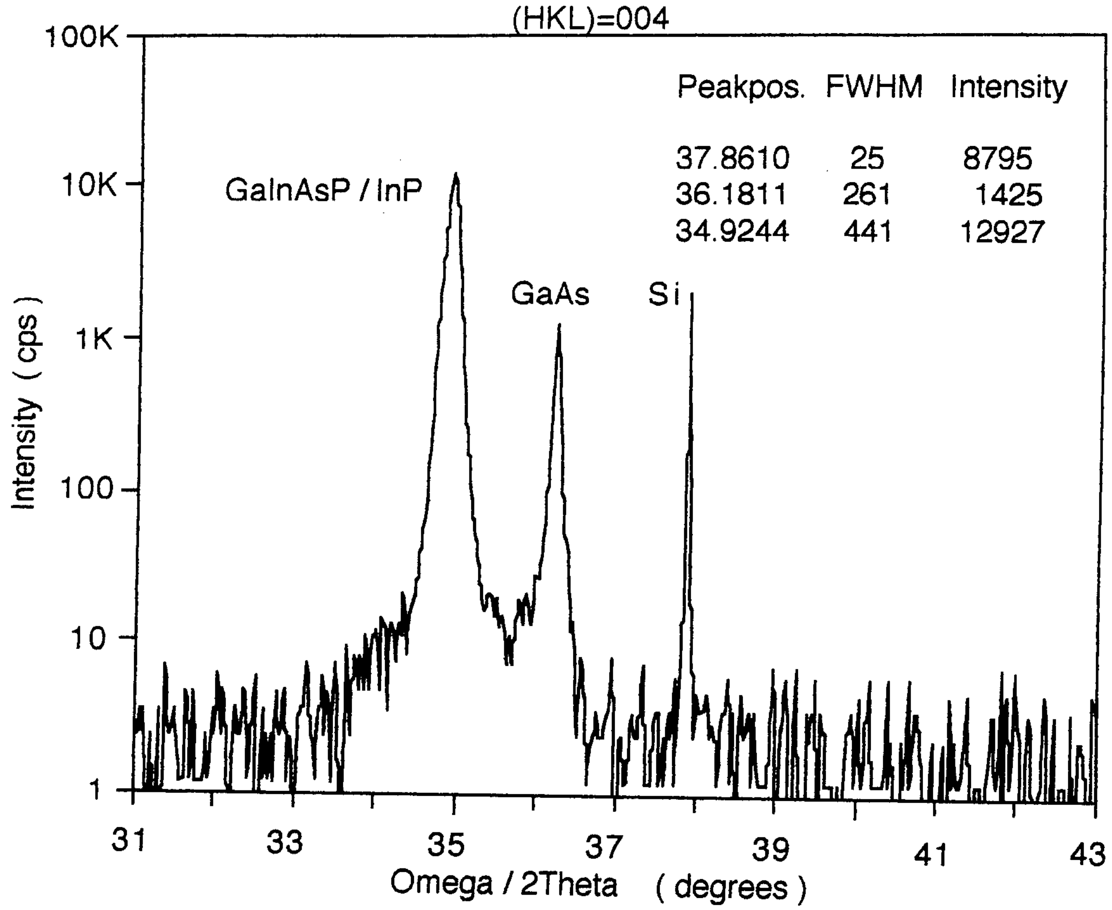

Figure 2.4. High resolution x-ray diffraction showing lattice matching between the quaternary layers. The inset shows the FWHM of the peaks given in units of arc seconds. The intensity is indicated in counts per second (cps).

2.3 Photoluminescence measurements

The photoluminescence (PL) spectra of the double heterostructure laser is shown in figure 2.5. The excitation source was the blue line (l = 488 nm) of an argon laser at an output power of 30 mW. As noticed from figure 2.5 the only peak observed is the one due to the InGaAs contact layer. This is due to the fact that InGaAs absorbs practically all of the argon laser photons. Therefore the InGaAs contact layer had to be etched away in order to observe any luminescence from the lower layers. The etching was done using a 1:1:8 solution of $H_3PO_4 : H_2O_2 : H_2O$. The H_2O_2 content of the solution reacts with the InGaAs to create an oxide which is then etched away by H_3PO_4. This is a selective etching process and the chemical reaction stops upon reaching the InP layer. The etching rate of the InGaAs using this solution with no stirring is approximately 5000 Å / min. Scanning electron microscope pictures confirmed that this etching process leads to effective removal of the InGaAs layer without altering the thickness of the InP layer.

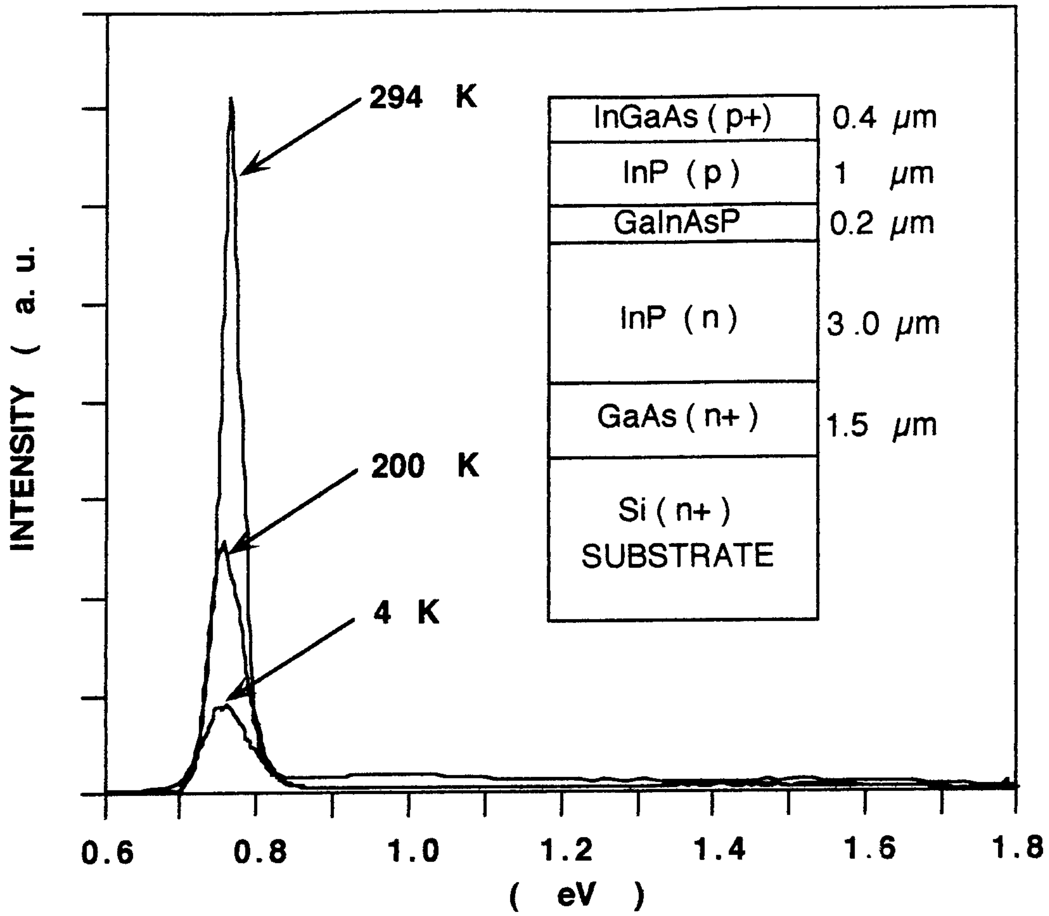

Figure 2.5 Photoluminescence spectra of the laser structure before the removal of the contact layer. The only peak observed at any temperature is the one due to the InGaAs.

After removal of the InGaAs contact layer the sample was once more excited with the argon laser and the room temperature photoluminescence spectrum is shown in figure 2.6. The spectrum peaks at the expected wavelength of 1.35 μm (0.92 eV) with a FWHM of about 75 meV. This peak is caused by recombination in the InGaAsP active layer. The FWHM of the room temperature photoluminescence peak, along with the absence of any other peak, is good evidence of tight carrier confinement in the quaternary active layer.

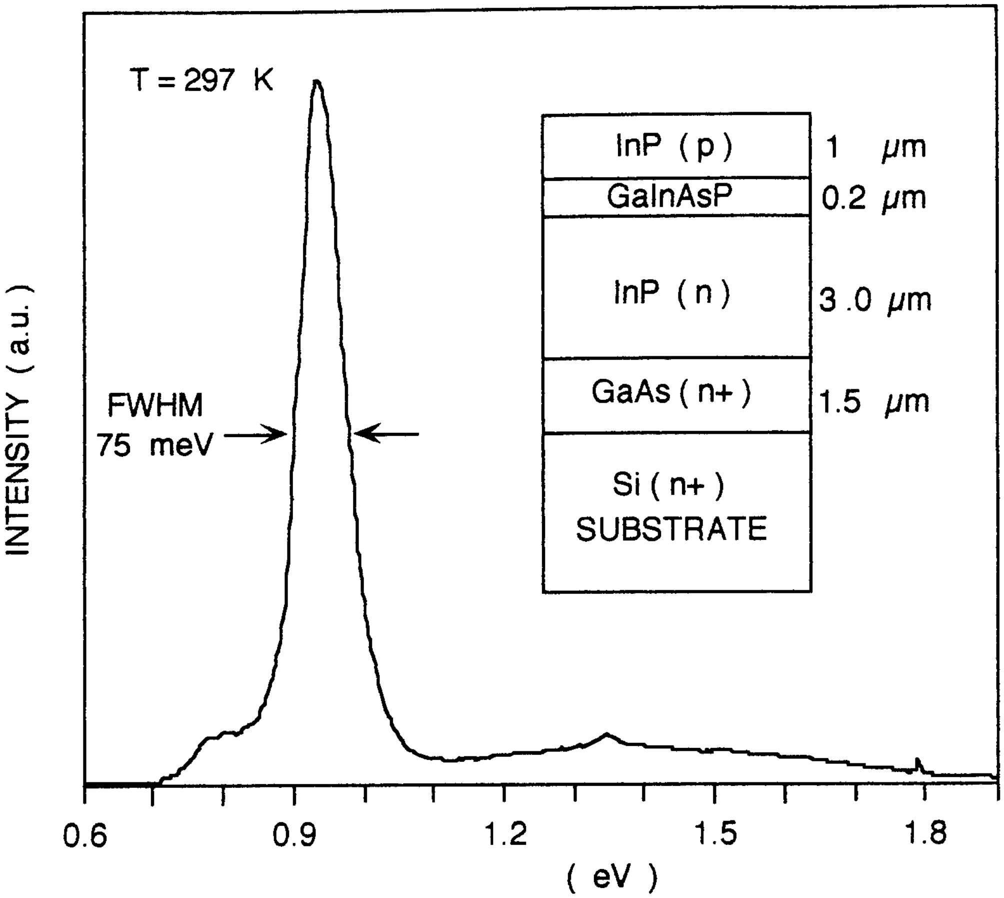

Figure 2.6 Room temperature photoluminescence spectrum peaks at a wavelength of 1.35 μm with a FWHM of 75 meV. The inset shows the schematic of the structure and the thickness of each layer after the 0.4 μm InGaAs contact layer was removed.

To obtain full spectroscopic information it is necessary to cool the sample to very low temperatures. The cooling process has the effect of minimizing thermal line width broadening and thermally activated nonradiative recombination processes. Generally the thermal distribution of carriers excited into a band contributes a width of approximately kT/2 to the emission line originating from that band and therefore in order to reduce the line width it is necessary to cool the sample. Figure 2.7 shows the photoluminescence spectra at different temperatures ranging from 4 K up to 200 K. Two peaks corresponding to extrinsic (946 meV) and intrinsic (980 meV) recombination in the quaternary layer were detected. The peak due to intrinsic electron-hole recombinations does not disappear with rising temperatures. However, the peak due to extrinsic recombinations in the quaternary layer rapidly decreases in intensity as the temperature increases and is evident at the room temperature spectrum only in the form of small shoulder adjacent to the intrinsic quaternary peak.

At low temperatures the InP peak is clearly seen at the expected bandgap energy of 1.35 eV. Deep level defects and shallow impurities in the heavily doped InP cladding layer cause the two peaks at about 0.8 and 1.3 eV respectively. These are observed at low temperatures only. These two peaks gradually disappear as the temperature is increased up to room temperature and disappear completely as the temperature approaches 297 K.

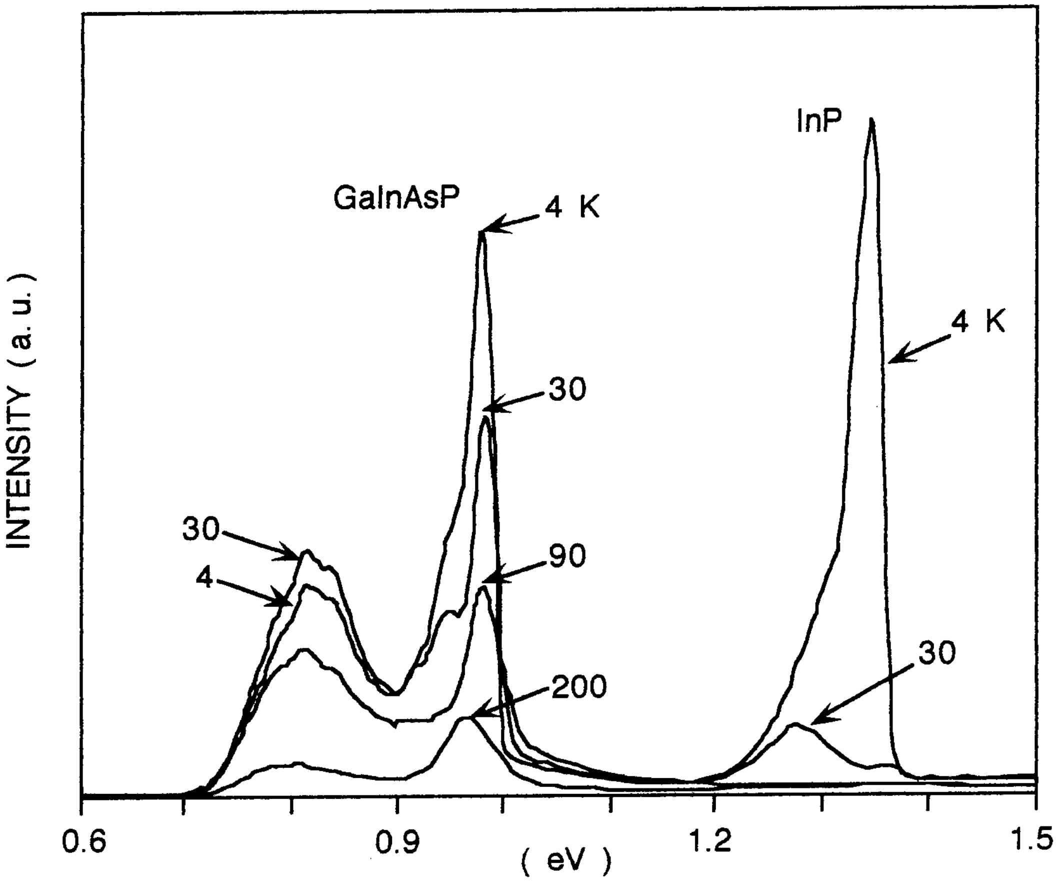

Figure 2.7 Photoluminescence spectra at four different temperatures ranging from 4 to 200 K.

For samples that are good, that is are grown on InP substrate and have higher crystalline quality than those grown on Si nonradiative centers are very few and as a result the integral intensity (area under the PL curve) of the PL peak of the active layer should show a weaker dependence on temperature. In samples with higher defect density (large number of non-radiative centers) in the active layer, the integral intensity at low temperatures is higher than at high temperatures. This is because radiative lifetime is shorter at low temperatures and as a result carriers recombine mostly radiatively rather than non-radiatively. This is why the InGaAsP PL intensity peak increases with decreasing temperatures.

The change in the PL intensity peaks of the upper InP layer is for one part the same as explained above in the case of the InGaAsP active layer. An additional reason could be that for InP layer at low temperatures the diffusion length for excess carriers is smaller than at high temperatures. As a result most of the excess carriers recombine in the InP layer. The small diffusion length prevents them from reaching the surrounding smaller bandgap material; InGaAsP. This effect is schematically shown in figure 2.8. At high temperatures, however, because of this larger diffusion length in InP layer the active layer adjacent to the InP layer receives the considerable portion of the excess carriers generated in

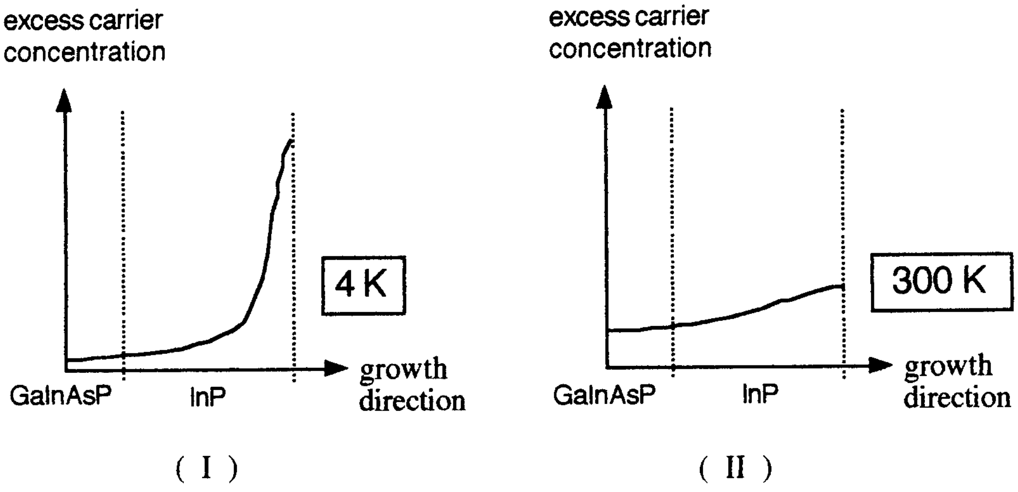

Figure 2.8 Schematic diagram showing excess carrier concentration in the InP layer and diffusion into the neighboring InGaAsP layer at temperatures of (I) 4 K and (II) 300 K.

its neighboring InP layer. This means that at high temperatures compared to helium temperatures the " effective " level of excitation of the active layer could be much higher than expected in case of photon excitation alone. So if this diffusion length change was not an issue, the growth of the active layer PL peak with decreasing temperature could be much higher than observed experimentally. Comparing the PL spectra at low and high temperatures we see that the active layer PL peak at 200 K is about 15 % of its value at 4 K. If only change of radiative lifetime with temperature was the cause and the diffusion length in InP remained constant with changing temperatures then the PL peak of the GaInAsP layer at 200 K would be for example only a small fraction of its value at 4 K.

CHAPTER 3

Laser Diode Processing and Fabrication Technology

3.1 Introduction

The first step in the processing of laser diodes is the preparation of the epilayer side, sometimes referred to as the p-side, of the sample. It is through this process that the contact stripes are patterned onto to the sample surface using a variety of photolithography techniques. The procedures used throughout these series of experiments essentially fall into three categories. These are the procedures used to fabricate broad area lasers with metal stripes by direct patterning, broad area lasers prepared using the liftoff process, and finally double channel lateral confinement lasers. These methods, each suitable for a different purpose are described in detail below.

3.2 Preparation of broad area lasers by direct patterning

The contact layer of the lasers used here are made of highly p-type doped InGaAs. In order to make a good ohmic contact to this layer it is necessary to deposit a layer of AuZn on the surface through thermal evaporation of the metal alloy. Typically the thickness of AuZn deposited is in the order of 500 Å. The AuZn used contains 16 % Zn and 84 % Au by weight. However, it was found that such material deposited directly on the surface of the wafer results in excessive diffusion of Zn deep into the crystal during the annealing cycle. In order to avoid excessive Zn diffusion a very thin layer of pure gold has to be deposited prior to the deposition of AuZn in order to create a buffer layer preventing excessive Zn diffusion. The thickness of this thin Au layer is critical since too thick a layer will result in drastic increase of the device series resistance due to the Schottky barrier effect. After experimenting with layers of various thickness the optimum Au layer thickness was determined to be around 140 Å. Such layer both helps stop excessive Zn diffusion into the epilayer contact layer and yet keeps the resistance of the device reasonably low. The 500 Å thick AuZn layer makes a good ohmic contact but due to its very small thickness is not possible to attach wire or probe connection to it. In order to be able to inject current into the device it is necessary to bring a probe in contact with the metallic layer or make wire bonds to it. The minimum thickness that allows this without piercing of the layer is about 2000 Å. As a result an additional 2000 Å pure gold is deposited on top of the relatively thin Au and AuZn layer. It is even better to have a contact that has a total thickness of 5000 Å but then this more than doubles the amount of Au that needs to be evaporated and thus makes the whole process more costly. The final contact consists typically of Au(140 Å)-AuZn(500 Å)- Au(2000 Å).

A very crucial issue in deposition of these metallic layers is the preparation of the semiconductor surface prior to evaporation. Without appropriate preparation the contacts will suffer both high resistance and poor morphology and in addition will easily peel off the semiconductor. Proper preparation of the surface involves two important processes of degreasing and deoxidation. Decreasing is done by submerging the sample in three baths of Trichloroethane (TCA), acetone, and methanol, in the order mentioned, for 5 minutes each. After degreasing in the manner described above the sample must be deoxidized for a few seconds in 1 % HF acid-water solution, rinsed with DI water and then blow dried with nitrogen and immediately loaded in the evaporator's vacuum chamber. Failure to deoxidize properly results in high device resistance. The sample is now ready for the evaporation of the Au/AuZn/Au layers.

Through evaporation process a uniform layer of metal is deposited on the surface of the semiconductor. It is now possible to pattern the stripe onto this layer by etching away specific areas of the Au layer. An alternative method is the use of a stainless steel mask to cover the sample during the evaporation. This will cause the metal to deposit only on areas not shadowed by the mask and has the advantage of doing away with the photolithography steps and thus reduces the processing time. But it has the disadvantage of creating stripes that do not have very sharp edges. It was observed that the use of an in situ evaporation mask results in irregularities at the edge of the stripes.

Once the sample is removed from the evaporation chamber it is recommended that it undergoes a pre annealing process. In this step the sample is heated for about 5 seconds on a hot plate placed in Forming gas environment at the temperature of 320 ^{o}C. Forming gas consists of 10 % hydrogen and 90 % nitrogen and helps in the formation of the contact. The duration and the temperature of this pre annealing process is very important. If the sample is allowed to fully anneal either through application of high temperatures or long annealing time the AuZn will form a eutectic bond with the semiconductor and it is then impossible to remove it completely from the areas that have to be bare of metal. On the other hand without this short and low temperature pre annealing step the contact is very likely to peel off during either the photolithography or the polishing cycles. More will be said about annealing later on. Pre annealing increases the adhesiveness of the metallic layer to the semiconductor without actually forming a eutectic bond.

The sample then has to undergo a simple photolithography process. This involves the deposition of a Shipley brand positive type photoresist followed by a 30 minute soft baking process in an oven set at 90 ^{o}C. The photoresist is deposited on the static sample and then spinned using a spinner running at 5000 rpm for 25 seconds. This results in a photoresist layer approximately 1 μm thick which is ready for exposure.

A photolithography mask with 100 μm wide opaque regions positioned periodically every 300 μm is used to selectively expose the sample to ultra violet radiation for 6 seconds. The exposure is done using a Karl Suss mask aligner. After the exposure the sample is immersed in a developer bath and developed until the pattern appears clearly. Using a 5 to 1 water and developer solution usually requires a developing time of about 1 minute. The sample is then hardbaked in an oven set at 120 ^{o}C for 30 minutes. Once the integrity of the photoresist layer is fully established through hard baking it is possible to remove the gold layers through a simple etching process which removes the gold layer where they are not covered with photoresist and leaves them intact where they are protected with photoresist layer. The etchant used to remove the Au layer consists of KI/I/H2O = 40 grams/3 grams/100ml.

Dipping the sample in this solution for about 7 seconds is sufficient to remove about 2500 Å of Au based metalization. Once the proper gold pattern is formed on the surface the sample can be fully annealed if desired. However, since it would be necessary to anneal the contact that will later be deposited on the substrate side of the sample too, it is better to anneal both side contacts at the same time in order to save the sample from undergoing an extra heating cycle which increases the amount of damage caused by thermal induced stresses.

The current injected into the laser diode through the gold stripes will tend to spread in the InGaAs layer before reaching the quaternary active layer. This results in an increase of the threshold current density of the device and is a very undesirable effect. The remedy is to etch away the InGaAs in the regions between the gold stripes. As mentioned in an earlier chapter the etching can be done using a 1:1:8 solution of $H_3PO_4 : H_2O_2 : H_2O$. By now the sample looks as shown in the schematic diagram of figure 3.1.

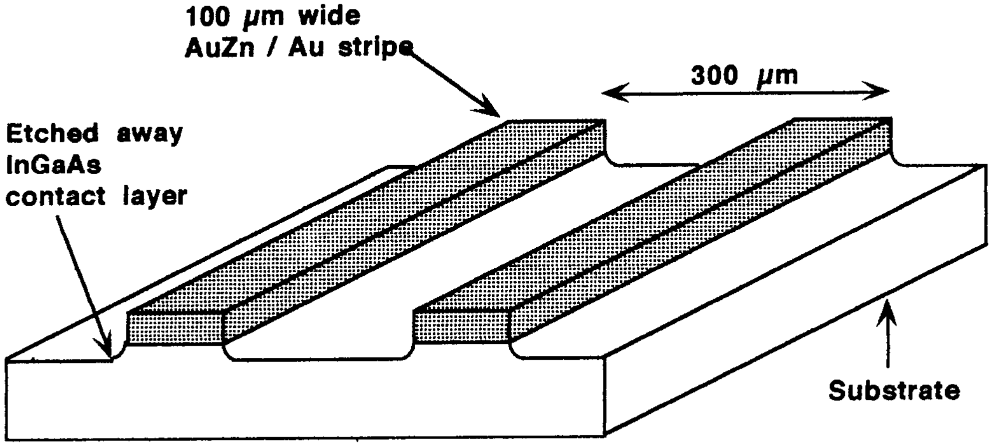

Figure 3.1 The laser after the AuZn/Au metalization contact has been deposited and patterned on the epilayer side of the sample.

A 100 μm wide Au contact is a rather wide stripe in the sense that it is possible to easily bring a micro probe in contact with it for the purpose of current injection or make a wire bond. However, sometimes it is necessary to place the laser on a heat sink with its p-side facing down in order to more effectively remove the excess heat from the active region which is closer to the p-side of the sample than to the substrate side of the sample. In this case it is important to electrically passivate the regions between the stripes so that current is injected only through the 100 μm stripes. One simple and effective method of doing this is through deposition of a blanket layer of Au over the whole surface. Au when brought in direct contact with the semiconductor surface forms a Schottky contact which prevents the flow of current from the metal into the semiconductor. In contrast AuZn/Au layer, through diffusion of Zn into the crystal, forms an ohmic contact which is very suitable for the purpose of injecting of current into the device. This Schottky barrier metalization is shown schematically in figure 3.2.

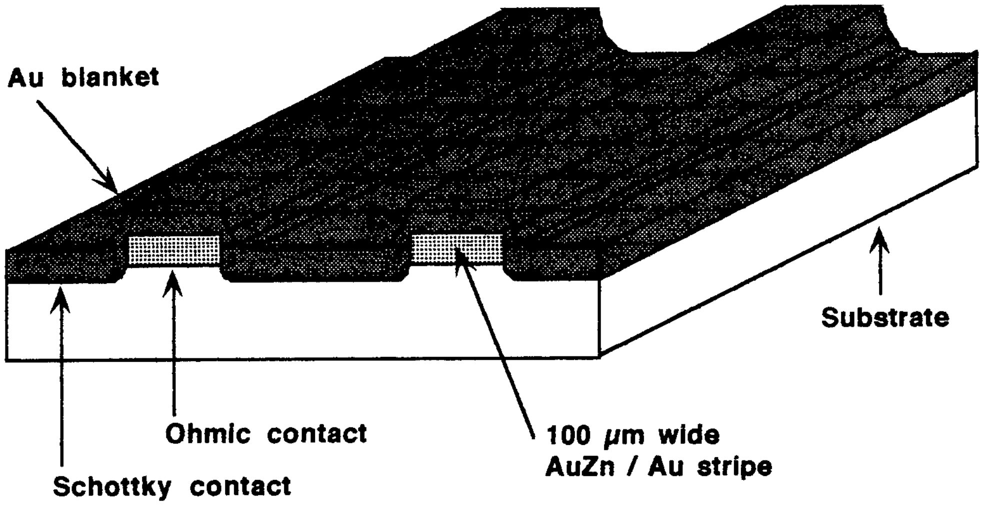

Figure 3.2 Sample after deposition of Au layer used as passivation through formation of a Schottky barrier.

3.3 Processing of broad area lasers using the liftoff process

An alternative to the AuZn/Au ohmic contact for the p side of the sample is Ti/Pt/Au. One advantage of Ti/Pt/Au is the fact that it is not necessary to go through an annealing process in order to form an ohmic contact. In the case of AuZn/Au contact through annealing process the AuZn layer forms an alloy with the semiconductor in order to create ohmic contact. In contrast Pt forms a non-alloy ohmic contact with the semiconductor. In order to promote the adhesion of the Pt to the semiconductor a very thin layer Ti ($\approx$100 Å) is usually deposited on the semiconductor surface prior to Pt deposition. The elimination of one annealing process is very important in the case of laser structures grown on Si which are highly prone to thermal induced stresses resulting from the difference of thermal expansion coefficient between Si, GaAs, and InP layers. In addition when using Ti/Pt/Au there is no problem with excess diffusion of Zn into the top semiconductor layer which is a concern in the case of AuZn/Au contacts.

Due to the high evaporation temperature of Ti and Pt it is not practical to deposit these metals through thermal evaporation methods and it is necessary to use an electron beam evaporator. In the case of AuZn/Au layers a chemical etching process was used to remove the metal and create stripe patterns on the surface of the semiconductor sample. However, a chemical etching process is not very suitable when dealing with Ti and Pt because Pt is very resistant to various etchants. As a result in these series of experiments, 20 μm wide stripes of Ti(100Å)/Pt(300Å)/Au(5000Å) were deposited on the epilayer side of the sample through a photolithography liftoff process. The liftoff process is schematically shown in figure 3.3. In this process two different types of photoresist are deposited one over the other to create a stripe pattern of desired width over the semiconductor surface. Notice that after development of the photoresists undercut is created. This effect is deliberate and in fact the reason for using two different layers of photoresist is to achieve this effect. This undercut greatly helps in the lifting off process when the sample is chemically treated after the deposition of the Ti/Pt/Au layers resulting in stripes with sharp straight edges.

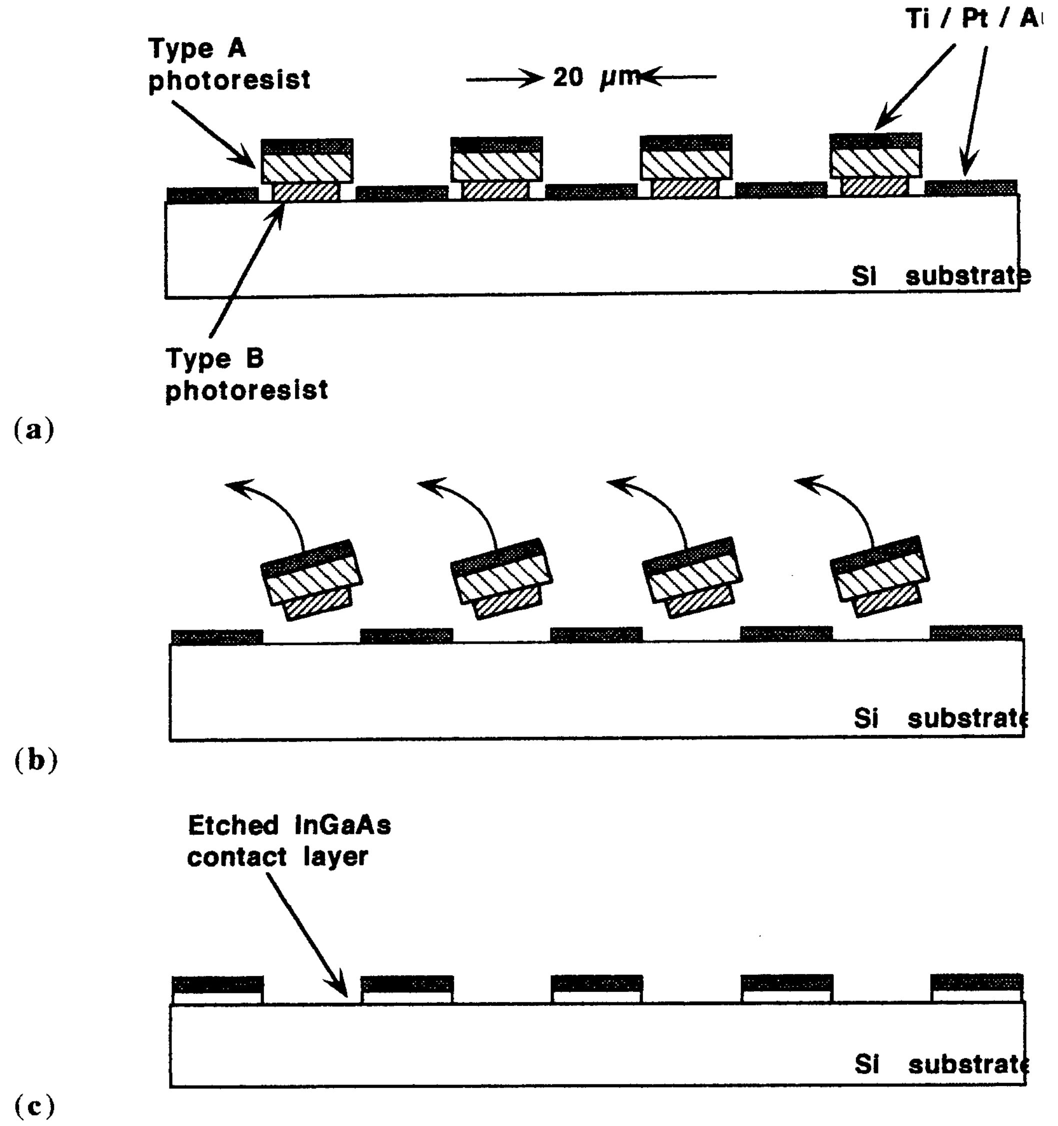
Ti / Pt / A
Type A
photoresist
20 μm
Si substrat
Type B
photoresist
(a)
Si substrat
(b)
Etched InGaAs
contact layer
Si substrat
(c)

Figure 3.3 a) deposition of Ti/Pt/Au layers over patterned photoresist layers, b) lift-off of preselected regions of metalization through chemical treatment of the sample, c) etching of the InGaAs contact layer.

In order to decrease the current spreading the InGaAs contact layer between the 20 μm stripes is usually etched away using the chemical process explained earlier. No significant under-cut could be observed using a scanning electron microscope Figure 3.4 shows the surface of the sample after the metallic stripes have been created through the liftoff process.

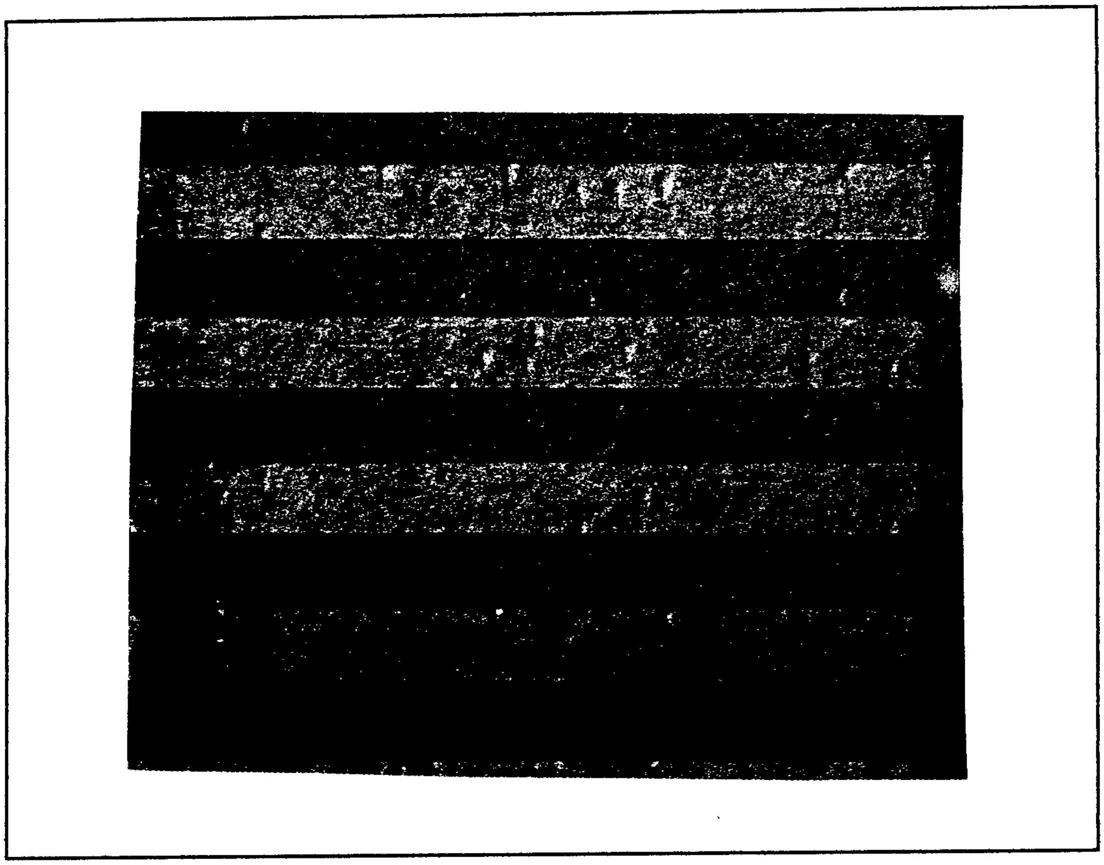

Figure 3.4 Top view photograph showing the 20 μm wide Ti/Pt/Au stripes deposited on the p-side surface of the sample and patterned using a liftoff process.

3.4 Fabrication of double channel ridge lasers

The eventual goal of the ongoing project is to grow and process a laser on Si substrate which would operate, under continuous wave (cw) condition, at room temperature reliably. In order to achieve cw operation it is necessary to fabricate narrow ridge structure devices and to properly bond these devices onto reliable heat sinks. This section briefly outlines the highlights of the effort put into development and processing of ridge lasers such as those fabricated using the double channel technique.

The double channel process has been chosen as the most suitable method in the fabrication of ridge lasers. An alternative would be the application of proton implantation technology, but only the details of double channel process will be discussed.

3.4.1 Chemical etching of the channels

The first step is to etch the channels. Two 10 μm wide channels, which are separated from each other by a 10 μm ridge, were etched into the semiconductor. Once the pattern has been developed the InGaAs cap layer is etched away with the use of 1:1:8 phosphoric acid, hydrogen peroxide and water solution. The InP cladding layer is etched away using Hydrochloric acid solutions. The general photolithography steps are shown below in figure 3.5.

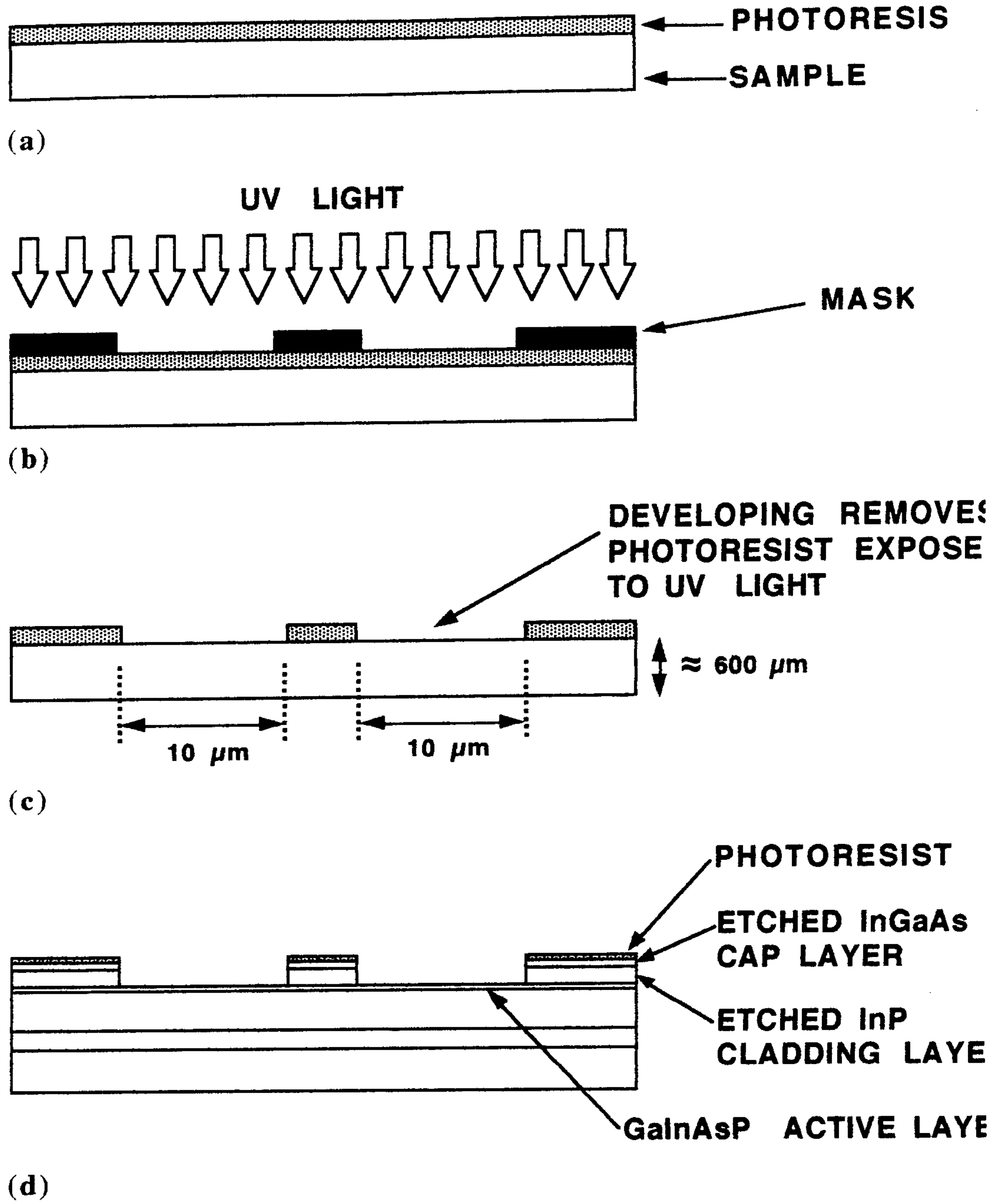
PHOTORESIS
SAMPLE
(a)
UV LIGHT
MASK
(b)
DEVELOPING REMOVE
PHOTORESIST EXPOSE
TO UV LIGHT
≈ 600 μm
10 μm
10 μm
(c)
PHOTORESIST
ETCHED InGaAs
CAP LAYER
ETCHED InP
CLADDING LAYE
GaInAsP ACTIVE LAYE
(d)

Figure 3.5 The different steps involved in etching of the double channels a) deposition of a 1 μm thick positive photoresist layer, b) exposure with UV light, c) development of double channels in the photoresist, d) chemical etching of the cap and cladding layers.

3.4.2 Dielectric passivation using SiO_2

After the channels have been etched and the photoresist is removed it is necessary to passivate the surface using a suitable dielectric layer. Previously an attempt was made to use Spin-On-Glass (SOG) for this purpose. SOG is a type of SiO_2 that is dispensed in the same way as photoresist and then baked. This was done due to the fact that at that time the facility to deposit the more suitable vapor deposited silicon dioxide was not operational. However eventually it was possible to deposit silicon dioxide (SiO_2) using the Plasma Enhanced Chemical Vapor Deposition (PECVD) technique. In this operation silane and NO_2 are used to form the SiO_2 layer. However in order to form a dielectric layer which is both uniform and free of pin holes it is essential to optimize the conditions at which the PECVD machine operates. These parameters include the pressure inside the chamber and the flow of each individual gas, in addition to the substrate temperature and the RF generator power. These parameters were varied during several runs until the surface of the sample looked satisfactory. Figure 3.6 shows channels etched and the wafer then coated with SiO_2.

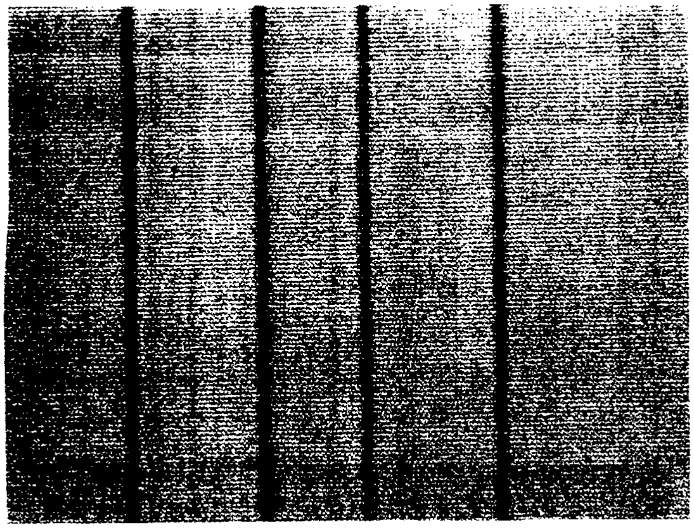

Figure 3.6 The top view of the double channels etched in the sample and the wafer then coated with about 6000 Å SiO_2 using PECVD method. The width of the channels shown in this photo is 10 μm.

3.4.3 Opening of windows in the SiO_2 layer using reactive ion etching

The next step in the processing of a lateral confinement laser is the opening of a window in the SiO_2 layer exactly over the ridge. This window has a width of 5 μm and requires a precise photolithography process. The width of the ridge is 10 μm.

Once the window has been opened in the photoresist, through developing, it is necessary to etch the SiO_2 layer in the area defined by this window. Attempts to do this through chemical etching failed due to the uncontrollably fast and non uniform etch rates when dealing with patterns in the order of few microns. As a result the window was opened using Reacting Ion Etching (RIE) technique. During this process sometimes it is necessary to unload the sample in the middle of the run for observation under the microscope. After several runs and the use of some experimental samples (pieces of Si and GaAs substrates coated with SiO_2) the proper combination and flow of the gases were established and a window was etched through the SiO_2 layer. The etching gas used was CF_4. Figure 3.7 shows the schematic of the photolithography process. Figure 3.8 shows the top and cross section views of the sample after etching of a 5 μm window in the SiO_2 layer over a 10 μm wide ridge.

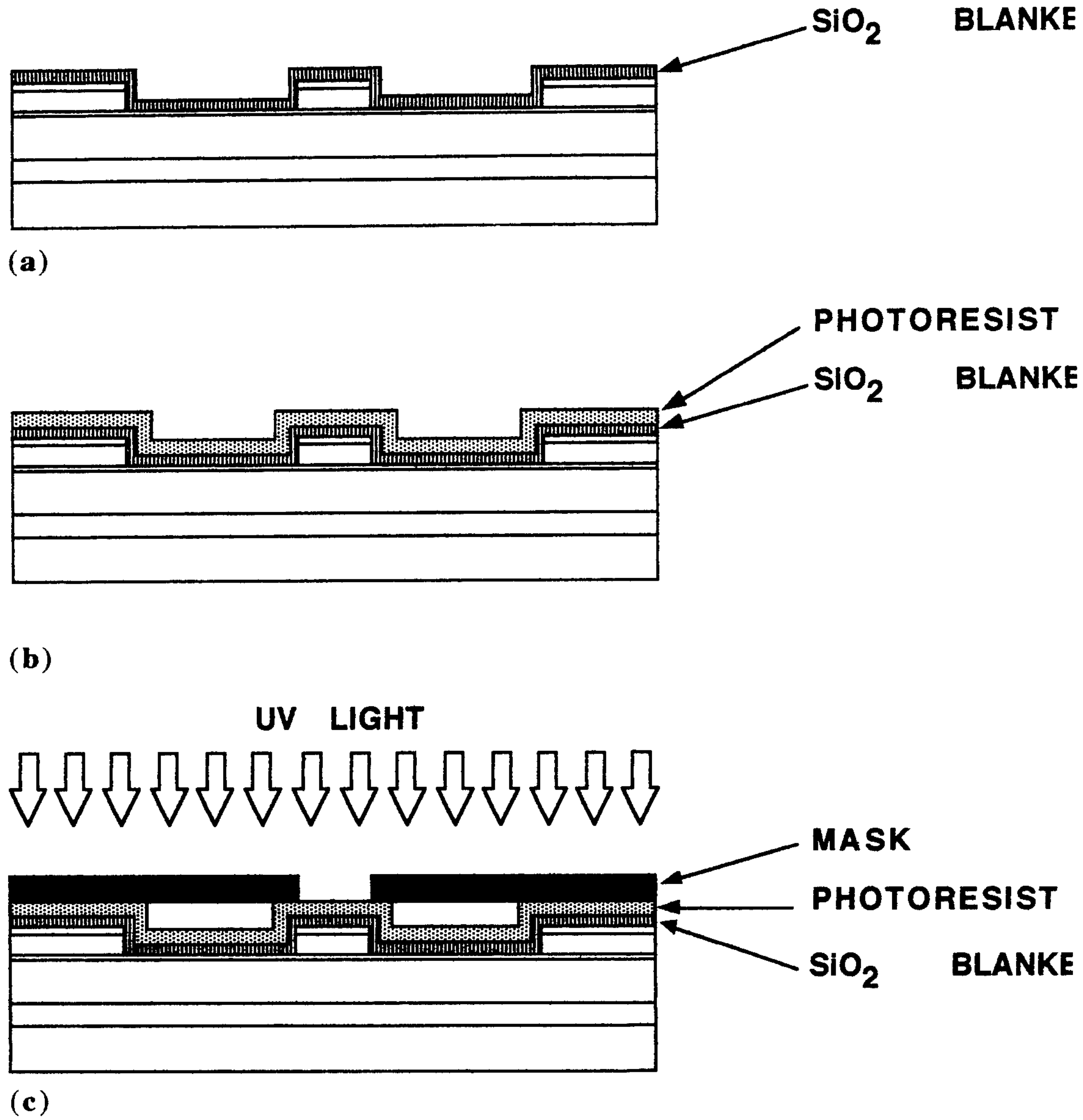
SiO_2 BLANKE
(a)
PHOTORESIST
SiO_2 BLANKE
(b)
UV LIGHT
MASK
PHOTORESIST
SiO_2 BLANKE
(c)

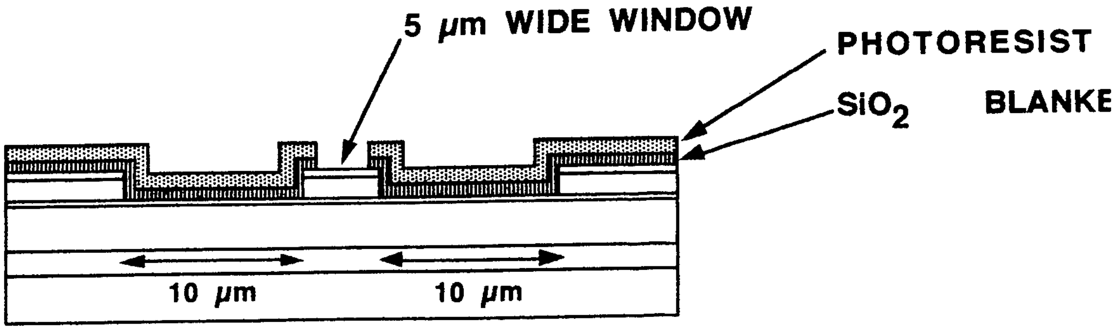
5 μm WIDE WINDOW
PHOTORESIST
SiO_2
BLANKE
10 μm
10 μm

(**d**)

Figure 3.7 The steps involved in opening of a window over the SiO_2 coated ridge. a) deposition of about 6000 Å of SiO_2 using the PECVD method, b) deposition of 1 μm thick positive photoresist layer, c) exposure with UV light, d) development of the photoresist and finally the etching of the SiO_2 layer using RIE technique.

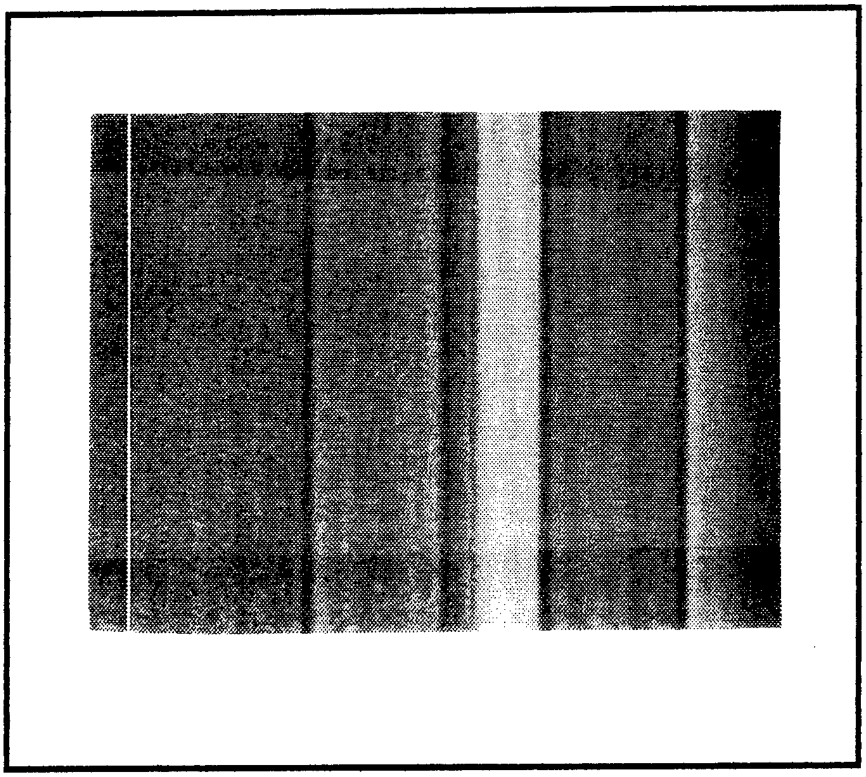

(**a**)

Figure 3.8.a Top view of the sample showing a window etched through the SiO_2 covered ridge using RIE method. The width of the channels is 10 μm.

The photos in figures 3.8.a and 3.8.b show the sample right after the window has been etched in the SiO_2 layer. Through a series of tests done with samples etched for a short time and studied under a microscope equipped with a Nomarski filter and then etched again it was observed that complete removal of SiO_2 and the exposure of the bare cap layer is indicated with a drastic change in contrast in the ridge area. This is shown in figure 3.8 top view photo. Even though the picture covers only a small area of the sample it is a typical representation of the whole surface.

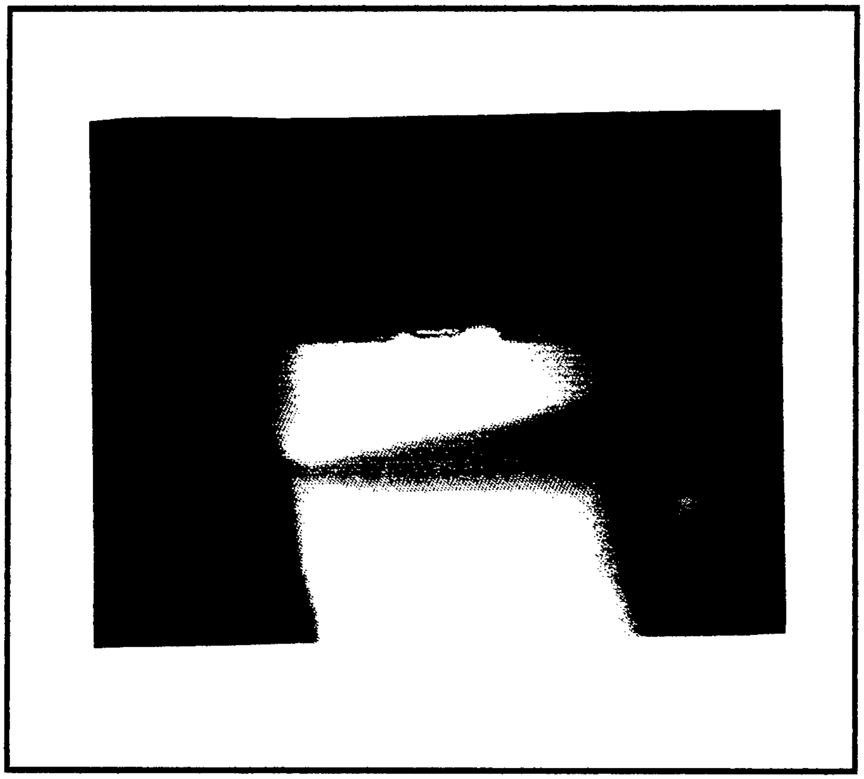
(b)

Figure 3.8.b Cross section view of the double channels showing the etched window in the SiO_2 layer. The cross section photo is taken under the same magnification as the top view photo.

Everywhere on the whole wafer, which was about 1 cm^2, the window is perfectly aligned to the ridge and the SiO_2 was removed uniformly without any indications of an undercut which was a major problem with chemical etching. The steps following the opening of the window in the SiO_2 using RIE are simply the coating of the p-side of the wafer with Ti/Pt/Au or

AuZn/Au, the thinning down of the sample to about 50 μm, the coating of the n-side with AuGe/Au, annealing, scribing and cleaving into individual diodes, and finally mounting of the devices on indium coated heat sinks. These procedures are essentially the same as those of processing of a broad area laser. Figure 3.9. shows the schematic of the laser after contacts have been deposited on both sides.

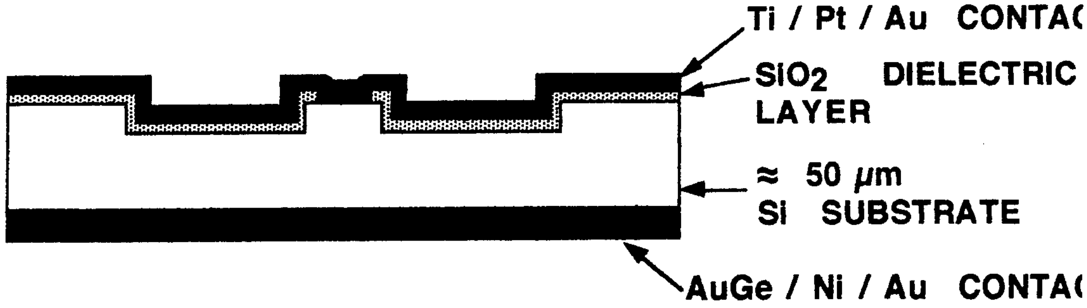

Figure 3.9 Deposition of metal contacts on the two sides of the sample in addition to lapping and polishing down to a thickness of about 50 μm results in a final product schematically shown here.

In summary in order to achieve cw operation of a laser grown on Si substrate it is necessary to firstly fabricate lateral confinement devices and secondly develop the capability of mounting these devices on heat sinks.

This section has briefly described the problems involved in fabricating a double channel laser. The first problem has been the etching of the channels. This problem has been solved using chemical etching approach. It is also possible to do this using dry etching which would be a more reproducible process. The second problem is the deposition of a suitable dielectric layer for passivation purposes. This problem has also been solved using plasma enhanced chemical vapor deposition of SiO_2. Using the same technique it is possible to deposit Si_3N_4 (silicon nitride) which may demonstrate advantages over SiO_2. Once the window has been opened the problem of etching the SiO_2 was solved using RIE method.

3.5 Lapping and polishing of the Si substrate

In order to facilitate the cleaving action it is necessary to thin down the sample to as small a thickness as possible. A thinner substrate also has the advantage of placing the active region of the laser closer to the heat sink surface in cases of n-side down bonded lasers. In case of the lasers grown on GaAs the samples are typically lapped down to a thickness of about 100 μm. GaAs samples with a thickness of less than 100 μm are too fragile to handle and break easily. Fortunately in the case of lasers grown on Si it is possible to thin down the sample to thicknesses of 50 or even 40 μm. Due to the high mechanical strength of Si a 50 μm thick Si sample can still be handled without too much difficulty.

To begin the lapping and polishing process the sample has to be bonded on a circular piece of glass with approximately 7 cm diameter and 1 cm thickness as shown in figure 3.10. A small piece of wax is put at the center of the glass puck and the puck is placed on a hotplate heated to about 6 0 ^{o}C. After the wax has melted the sample is placed on the puck, substrate side facing up, and scrap pieces of Si are arranged around the sample without overlapping it. Without taking the precaution of placing these scrap pieces around the sample the edges of the sample will get rounded during the lapping and polishing. Also the scrap pieces have the additional effect of reducing the chance of the sample coming off the glass puck during the process. The glass puck is placed in a vacuum chamber and the sample will get bonded to the glass under pressure from a rubber diaphragm while the wax is solidifying again.

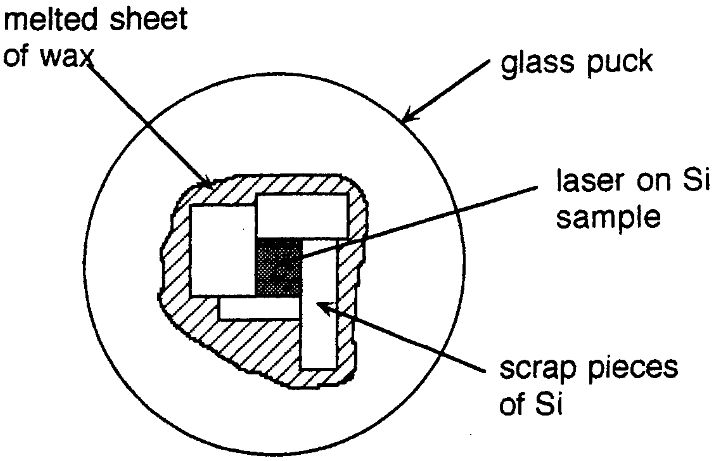

Figure 3.10 The laser sample wax bonded onto a glass puck as a preparation to lapping and polishing.

After the sample is properly bonded, the glass puck is attached to a polishing jig using vacuum. The polishing jig is put over the rotating disk of a Logitech polishing machine as shown in figure 3.11. This rotating disk is covered with a special black pad which is kept well lubricated with deionized water through out the whole process. The lapping is done using 3 μm size aluminum oxide powder which basically acts as the abrasive agent. The procedure is to lap the sample for several minutes with the lapping disk rotating at about 45 rpm, remove the jig, rinse the jig in deionized water, remove the glass puck rinse it and dry it with nitrogen, and measure the thickness of the sample. If the sample is still too thick go back and lap for a little while longer and then repeat the above steps until the thickness is approximately 10 μm thicker than the final desired thickness. To achieve an even better result one should begin the lapping with size 3 μm aluminum oxide powder and as the sample gets thinner reduce the size of the powder used to for example 1 μm size. Figure 3.11 schematically shows the lapping and polishing machine.

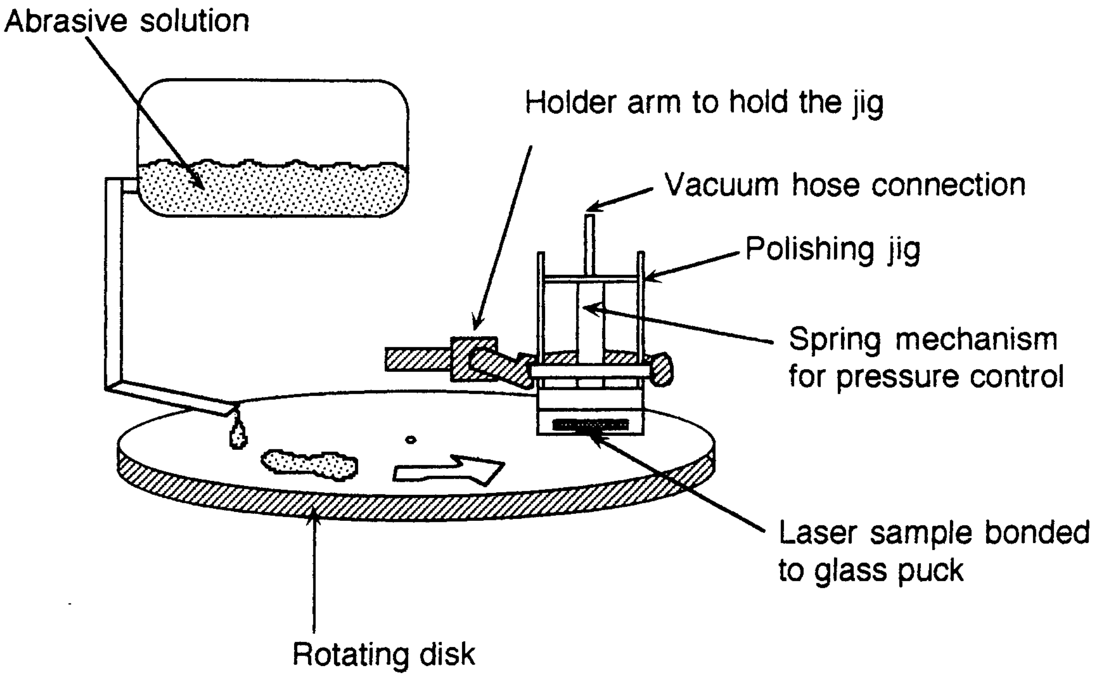
Abrasive solution
Holder arm to hold the jig
Vacuum hose connection
Polishing jig
Spring mechanism for pressure control
Laser sample bonded to glass puck
Rotating disk

Figure 3.11 Schematic diagram showing the polishing jig positioned over the rotating disk during the lapping procedure. The container at the top contains the abrasive solution. Aluminum oxide powder mixed with water is used for lapping and sodium hydrochloride solution is used for polishing.

At this point the surface of the substrate is smooth but not mirror like. The last 10 μm is removed through polishing with an abrasive chemical such as sodium hydrochloride. After polishing is concluded the surface of the sample should be very smooth and look mirror like.

It is very important not to apply too much pressure to the sample during the lapping and polishing procedure. Any stress applied to the sample could result in generation of micro-cracks at the interface between the III-V material and the Si substrate and result in further propagation of dislocations upward into the active region of the laser. In fact the polishing jig is equipped with a spring loaded mechanism used to adjust the pressure applied to the sample during the lapping and polishing. In processing of the lasers in these series of experiments the spring mechanism was adjusted such that almost zero pressure was put on the sample.

This results in a very slow lapping rate of only a few microns per minute but nevertheless is important in order to avoid damaging the sample.

3.6 Annealing

After the Si substrate has been lapped and polished down to the desired thickness of approximately 50 μm the sample is again degreased and deoxidized in the manner described before and set inside the vacuum chamber of the evaporator in order to deposit the n-side contact. The n-side contact in this case is consisted of 1000 Å AuGe, 200 Å Ni, and 5000 Å Au. The diffusion of Ge into the substrate during the annealing actually creates an eutectic alloy which serves well as an ohmic contact. The purpose of the thin layer of Ni is to prevent the AuGe from forming an uneven surface during the annealing process. AuGe generally has a tendency to ballup when heated to its eutectic temperature. The thick layer of Au serves as a firm foundation for any contacts such as wire bonds that have to be made to the sample.

The annealing process was done in a very simple manner by putting the sample on top of a hot plate which is placed inside a chamber filled with Forming gas. The temperature of the hot plate is controlled with an electronic temperature controller equipped with a temperature ramp adjustment control. The sample was annealed at 385 °C for 30 seconds.

3.7 Scribing and cleaving

The mirrors in a semiconductor laser consist of the two cleaved facets of the sample. These smooth facets are formed by first creating scribe lines at the edge of the sample and then applying pressure causes the semiconductor crystal to cleave along its cleavage plane. This process is shown in figure 3.12.

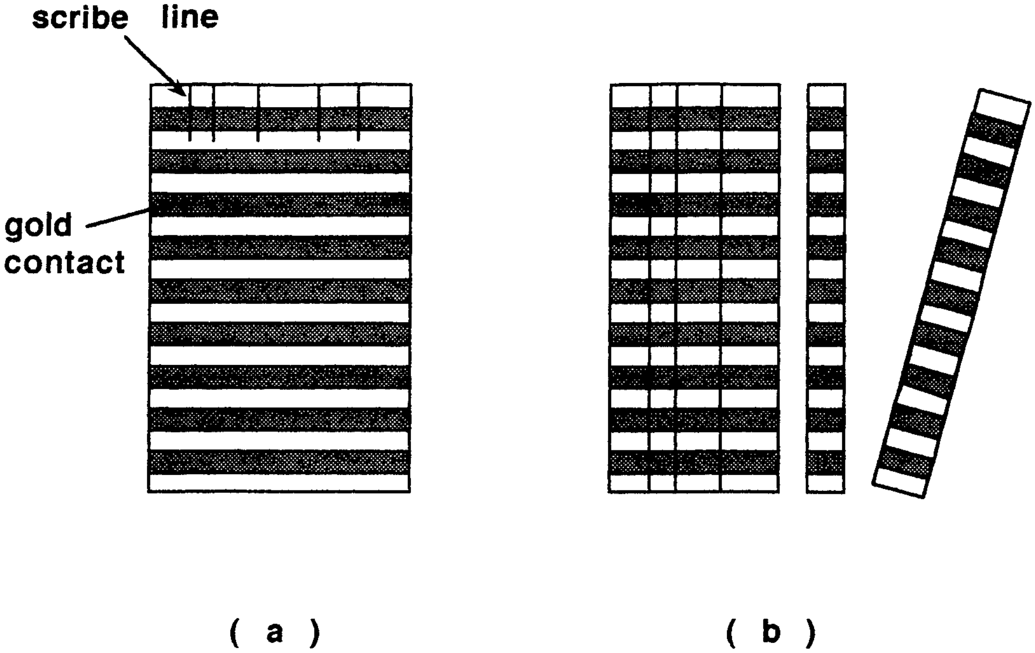

Figure 3.12 a) Approximately 50 μm long scribe lines are scratched at the edge of the sample, b) Application of pressure cleaves the sample along the scribe lines.

The problem associated with laser structures grown on Si is the fact that Si crystal does not have a cleavage plane and as a result it is not possible to easily create smooth mirror facets. One solution to this problem is to scribe the sample along the cleavage plane of the InP crystal and thus cause the sample to break parallel to this plane. In order for this approach to result in smooth mirror facets the thickness of the Si substrate has to be kept at a minimum. Fortunately due to the high mechanical strength of Si crystal it is possible to thin down the substrate to a thickness of approximately 50 μm and still be able to handle the sample without breaking it. Figure 3.13 shows the schematic diagram of a scriber machine designed and fabricated for proper scribing of the laser structure on Si substrate.

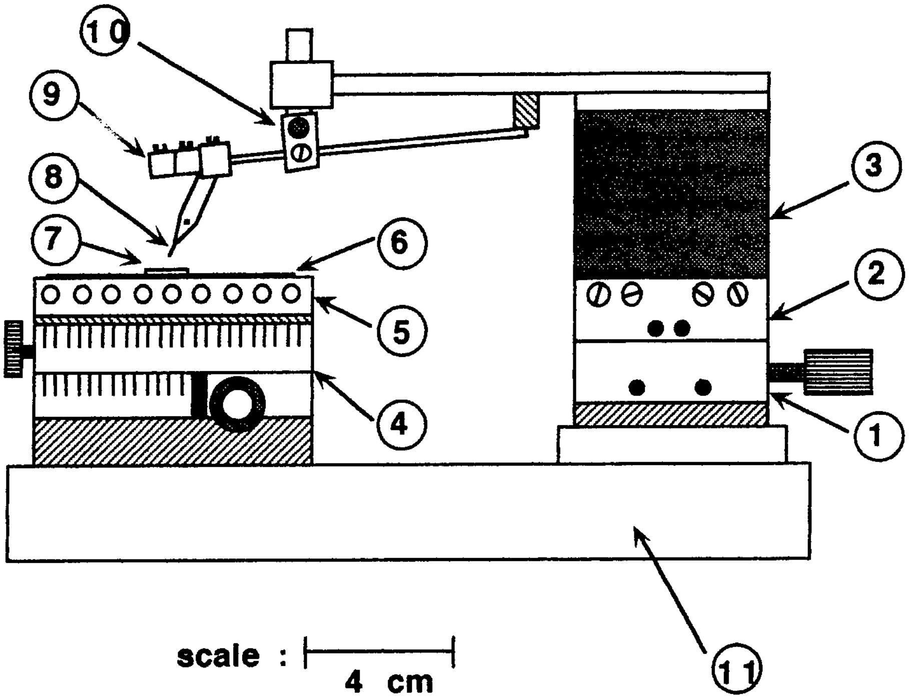
10
9
8
7
6
5
4
3
2
1
11
scale :
4 cm

Figure 3.13 Schematic diagram of the scribing machine followed by the list of different parts.

Figure 3.13 continued

1. X translation stage with micrometer
2. Y translation stage with micrometer
3. Z translation stage with micrometer
4. Rotation stage
5. Vacuum chuck
6. Low tack blue plastic tape
7. Semiconductor sample
8. Diamond scribing needle
9. Weights for adjusting needle pressure
10. Pivot pin
11. Heavy metallic base

Since the eventual goal is to grow laser structures monolithically on integrated circuits on Si substrates it will not be possible to achieve smooth mirror facets through cleaving anyway. Research has been done regarding the possibility of fabricating mirror facets through application of a dry etching technique using reactive ion beam etching methods [39-42]. In this manner it is possible to make mirror facets with 45 degree inclinations so that the light can be emitted from the laser in a direction perpendicular to the epilayers. Figure 3.14 shows a schematic representation of such horizontal cavity surface emitting laser.

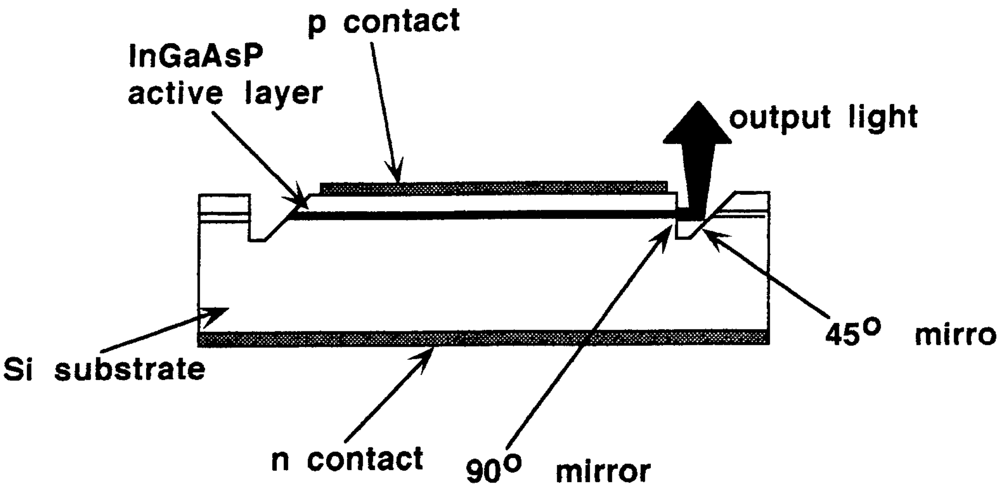

Figure 3.14 Schematic structure of InGaAsP/InP surface emitting laser with vertical and 45° mirrors created by reactive ion beam etching.

3.8 Development of heat sink and packaging technology:

It is well known that the removal of excess heat from a laser diode is highly critical in the performance of the device and its reliability. This is done through mounting of the devices on heat sinks, application of thermoelectric coolers, and essentially proper packaging. Considerable effort was put into developing the technical capability to package laser diodes. This included the development and fabrication of a versatile die bonding machine and establishment of a reliable procedure to fabricate low cost copper heat sinks coated with evaporated indium.

The heat sinks used in these series of experiments are basically a piece of copper coated with indium. The copper pieces are produced in large quantities at the local machine shop. They are then wax bonded on a piece of stainless still disk in a manner similar to bonding of the lasers on the glass puck prior to substrate lapping. The heat sinks, mounted on the stainless steel disk, are then brought in contact with the rotating disk of a polishing machine covered with a pad with approximately the same roughness as a very smooth sandpaper. The pad is continuously being lubricated with water through out the process. After polishing for a few minutes the heat sinks are taken to a different polishing machine with a pad of finer grain and the polishing process is repeated again. The heat sinks are processed through a total of five different rotating disks each covered with pads of progressively finer grain. The last two steps of polishing is done using diamond paste with grain size 3 μm and 0.5 μm . In this manner the heat sinks are polished very carefully until their surface is perfectly mirror like.

The surface smoothness of the heatsinks is very important in achieving satisfactory results with indium deposition. However, it is also very important that the heatsinks have very sharp 90 degree edges so that the laser dies can be placed perfectly at the edge without any problem. As a result after the surfaces of the heatsinks are polished it is necessary to stack them together with a clamp and polish their edges also. Only the edge at which the laser die is going to be mounted needs to be polished and sharpened.

Once the two surfaces of the heatsinks are prepared the heatsinks are chemically treated to remove any trace of grease and copper oxide. This is done immediately prior to placing them in a thermal evaporator vacuum chamber for the purpose of indium deposition. It was found that indium does not deposit favorably on bare copper surface. The result is usually a rough indium coating of poor morphology that melts very unevenly. To solve this problem first a 2000 Å layer of nickel is deposited on the very smooth and clean copper surface. Over this layer of nickel a 500 Å layer of gold is deposited followed by a comparatively thick 2 μm layer of 99.99 % pure indium. All the metals are deposited using thermal evaporation. The nickel basically serves as a hard and solid foundation setting the ground for the deposition of the layer of indium. The thin layer of gold isolates the indium from the nickel and prevents any possible undesirable chemical reaction between the two metals. In addition if the depositions of nickel and indium are done in separate evaporators the gold prevents the oxidization of the nickel surface during the transfer of the heatsinks from one machine to the other. The thicknesses of the three deposited metals are the optimum thicknesses necessary to achieve a smooth indium surface that melts very uniformly and then solidifies without any ballup effect. The heat sinks prepared in the manner described here should be used as soon as possible since indium is very prone to rapid oxidization. However they can typically be stored in a nitrogen box for up to one week without too much degradation in the quality of their indium coatings.

The process of mounting the laser dies on the heatsinks consists of accurately positioning them at the sharp edge of the indium coated surface of the heatsinks and holding them in place while the indium melts and then solidifies. A special die bonding machine had to be designed, developed, and fabricated for this purpose. The schematic diagrams of this machine are shown in figures 3.15 and 3.16. A ceramic capillary is used to pick up the dies using vacuum suction. The tip of the ceramic capillary has inner and outer diameters of approximately 50 μm and 80 μm respectively and is suitable for handling dies as small as 100 μm at each edge without any damage to either the mirror facets or the contacts. Using a xyz translation stage equipped with micrometers the ceramic capillary, with the laser die holding to its tip, is positioned at the exact desired location on the surface of the heatsink. Once the die is properly positioned at the right spot, the heatsink which is sitting over a hot plate in nitrogen or Forming gas atmosphere, is heated to just over 160 ^{o}C which is the melting point of indium. The whole operation is monitored using a microscope and the onset of the indium melting is marked by a slight change of the indium surface appearance. Once the indium is melted the hotplate temperature is lowered and the heatsink is cooled down with nitrogen blow. Through out this process a crucial parameter is the force applied to the laser die. If the laser die is not gently pressed down during the indium melting it will not be bonded strongly enough to the heatsink and will most likely come off during the wire bonding steps. On the other hand too much pressure could either break the tiny fragile chip or push it too deep in the pool of molten indium. The latter effect is catastrophic in the case of samples bonded with their epilayer surface facing down on the heatsink and will definitely result in molten indium soaking the edges of the die and thus shorting out of the pn junction. In order to be able to accurately exert the right amount of pressure on the laser the die bonding machine is equipped with a spring mechanism designed for adjusting the applied force.

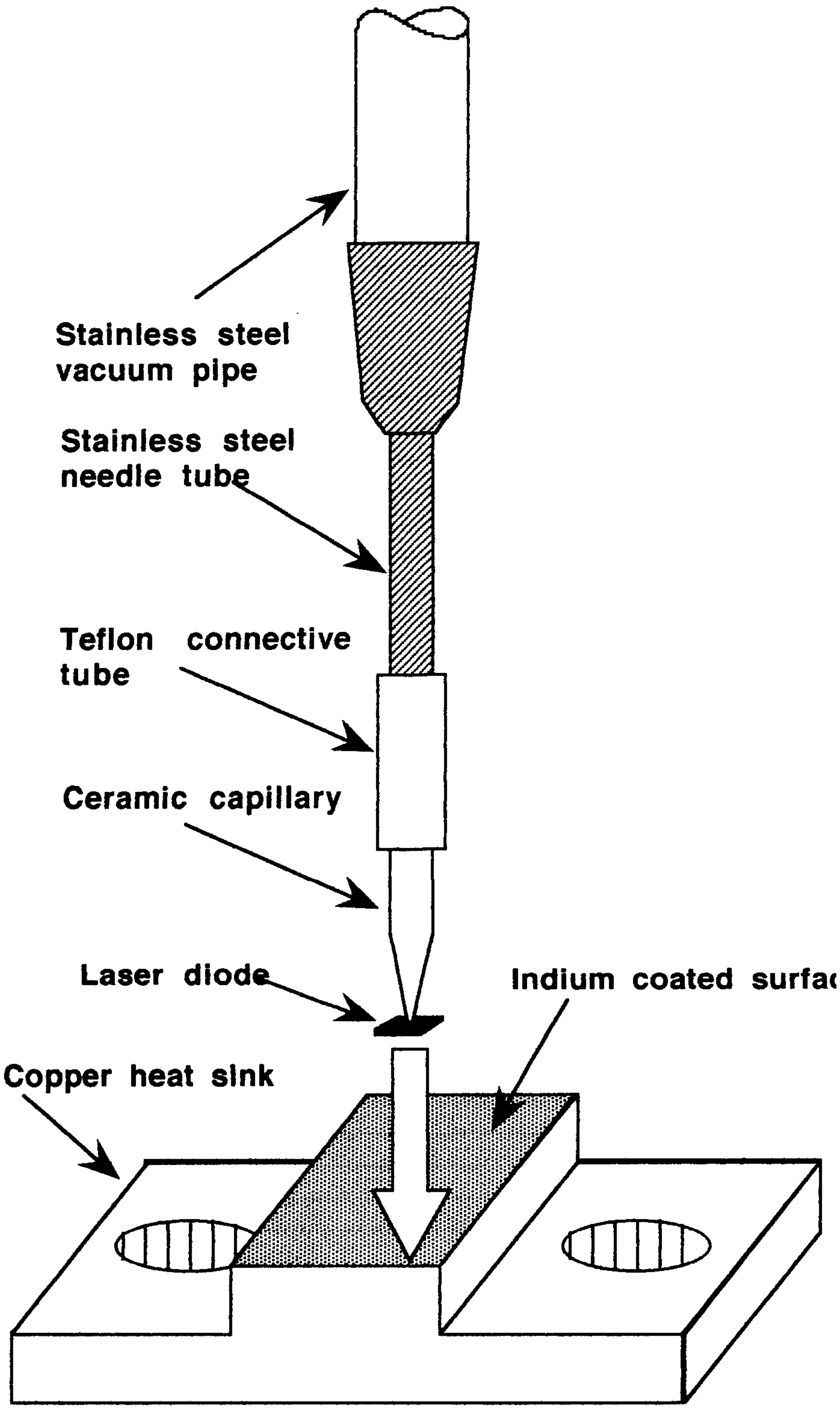
Stainless steel vacuum pipe
Stainless steel needle tube
Teflon connective tube
Ceramic capillary
Laser diode
Indium coated surfa
Copper heat sink

Figure 3.15 Schematic diagram showing the details of the system used to bond a laser diode onto the surface of an indium coated heatsink.

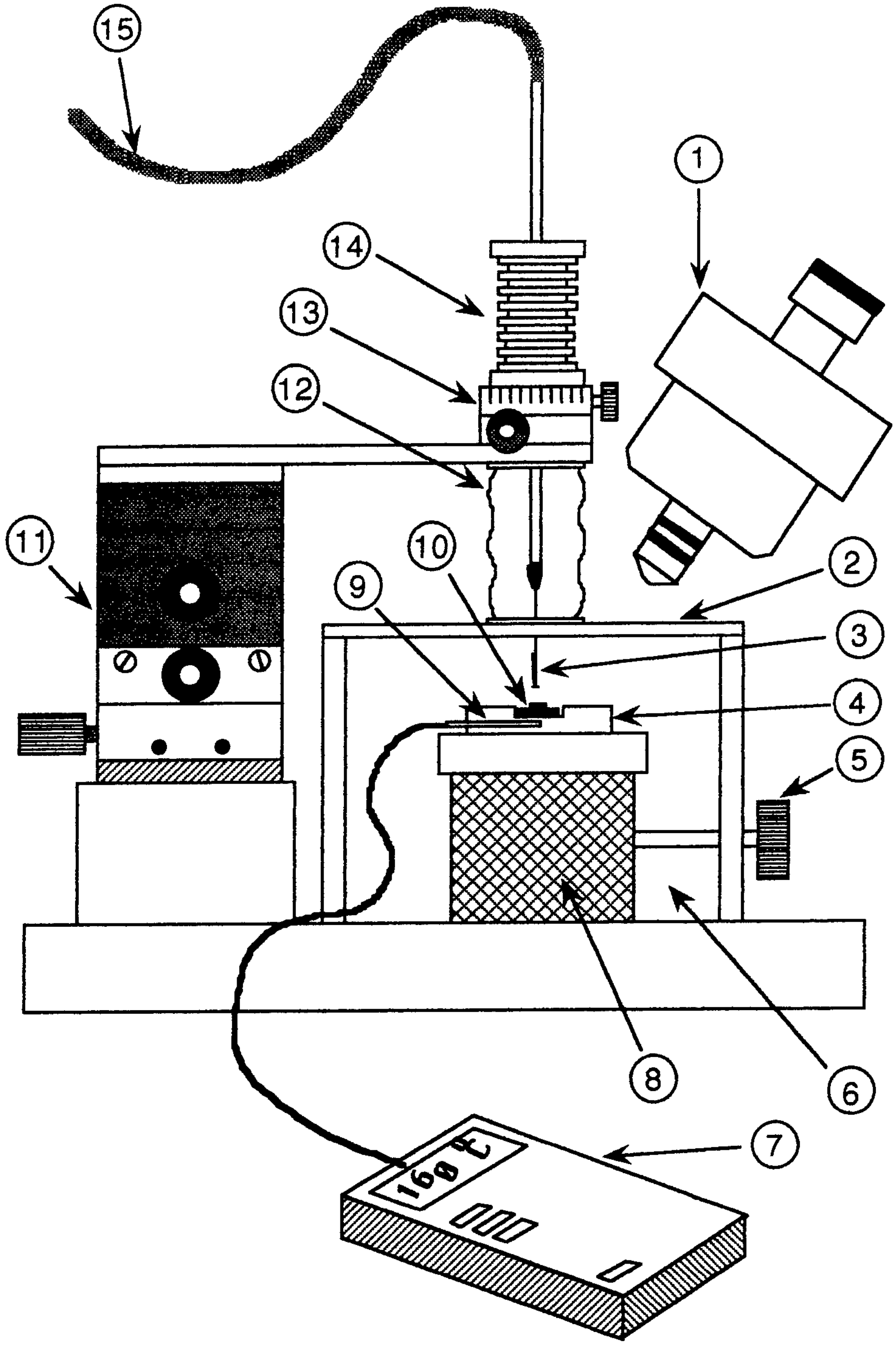
15
1
14
13
12
11
10
9
2
3
4
5
8
6
7
160 ℃

Figure 3.16 The schematic representation of the die bonding machine followed by the list and description of various parts. The details of the ceramic capillary system used to pick up the die are shown in the previous figure.

1. microscope
2. transparent Plexiglas cover
3. ceramic capillary suction tip
4. heat sink positioner
5. temperature adjustment knob
6. nitrogen or Forming gas atmosphere
7. thermocouple temperature monitor unit
8. hotplate
9. thermocouple
10. indium coated heat sink
11. xyz translation stage with micrometers
12. flexible sleeve
13. rotation stage
14. spring mechanism for pressure adjustment
15. vacuum hose

The heat sinks prepared using the technology described here have been used in the packaging of high power 808 nm lasers which have demonstrated excellent performance under long term continuous wave operation. The excess heat removal requirements of the lasers grown on silicon are generally less strict than the high power 808 nm lasers and thus as far as the 1.3 μm laser on silicon project is concerned the significant problems of excess heat removal, heat sinks, and packaging have been solved. Figure 3.17 shows schematic representation of the final product after wire bonding.

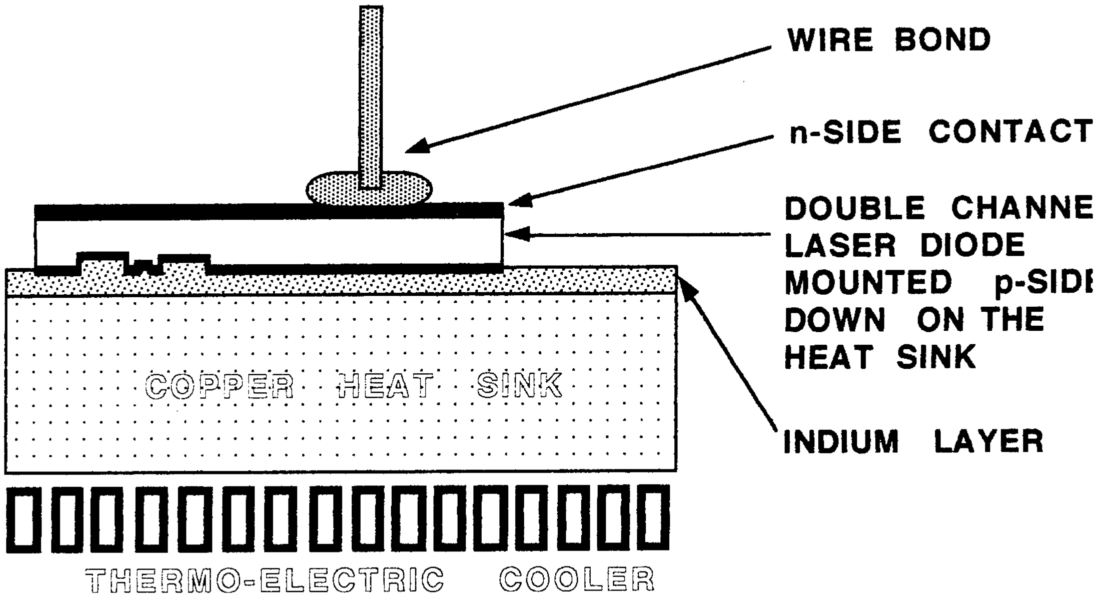
WIRE BOND
n-SIDE CONTACT
DOUBLE CHANNE
LASER DIODE
MOUNTED p-SIDI
DOWN ON THE
HEAT SINK
INDIUM LAYER
COPPER HEAT SINK
THERMO-ELECTRIC COOLER

Figure 3.17 Scribing and cleaving into individual diodes and mounting them on indium coated heat sinks results in a package suitable for efficient removal of excess heat.

CHAPTER 4

Characterization of Broad Area Lasers and Analysis of the Results

4.1 Preview

The characterization results of a series of laser diodes are presented in this section and analyzed. The details of the processing steps specific to the fabrication of these diodes were presented in the previous chapter and are briefly outlined below.

Through a photolithography liftoff process 20 μm wide stripes of Ti(100Å)/Pt(300Å)/Au(5000Å) were deposited on the epilayer side of the sample. The silicon substrate was then lapped down to about 50 μm thickness and the n-side contact which consists of AuGe(1000Å)/Au(1000Å) was evaporated and annealed at 385 °C for 30 seconds.. In order to decrease the current spreading the InGaAs contact layer between the 20 μm stripes was etched away without any significant under-cut. The wafer was then cleaved in bars with lengths ranging between 100 μm and 600 μm and the quality of the mirror facets were checked with an optical microscope. No anti-reflection or high-reflectivity coatings were applied on the mirror facets.

4.2 Analysis of Light versus Current Curve

4.2.1 Experimental setup and procedure

An Avtech pulse generator capable of delivering currents in excess of 5 Amperes was used to drive the laser diodes in the pulse mode. All the lasers were tested using pulses with 100 nsec width and a repetition rate of 5 KHz. These values correspond to a duty cycle of $5x10^{-4}$. In order to monitor the current and determine exactly how much current is being applied to the laser diode a current probe was used. This current probe, which is simply a coil in parallel with a capacitor, samples the current passing through the laser without disturbing the current and then feeds a voltage signal into the Boxcar Integrator. This voltage signal is proportional to the magnitude of the current pulse signal being applied to the laser diode. The Boxcar then creates a 50 nsec gate and gives the average of the probe signal during the gate. The Boxcar is triggered by the pulse generator and also sends an averaged D.C. signal to the x-y recorder for plotting the light power versus current curve. In addition the Boxcar transforms the current signal into a voltage signal that is viewed on the oscilloscope screen along with the gate signal. In this manner the current passing through the laser diode is monitored without influencing its shape or magnitude.

An integrating sphere equipped with a germanium photodetector was used to measure the output power of the laser. The sphere was used in order to ensure that all the light emitted from the front facet of the laser diode is collected properly and detector positioning with respect to the laser diode has no effect on the power values measured. The signal generated by the germanium detector was then processed through a radiometer which was accurately calibrated by the manufacturer to give precise readings depending on the specific wavelength of the output light. The radiometer then fed an average D.C. signal with amplitude proportional to the intensity of the collected output light into a x-y recorder.

The laser probe station was equipped with a thermoelectric cooler-heater for adjustment of the operating temperature of the laser. The temperature was monitored using a thermocouple embedded in the copper heat sink on which the laser diode was placed. In these series of experiments the laser diode was not indium bonded on the heat sink. It was simply placed at the edge of the heat sink and held firmly in place with a probe needle which also served to inject the current into the device. To avoid disturbance by room lights the entire laser probe station and the integrating sphere were covered by a thick black cloth. Figure 4.1 shows a schematic diagram of the experimental setup.

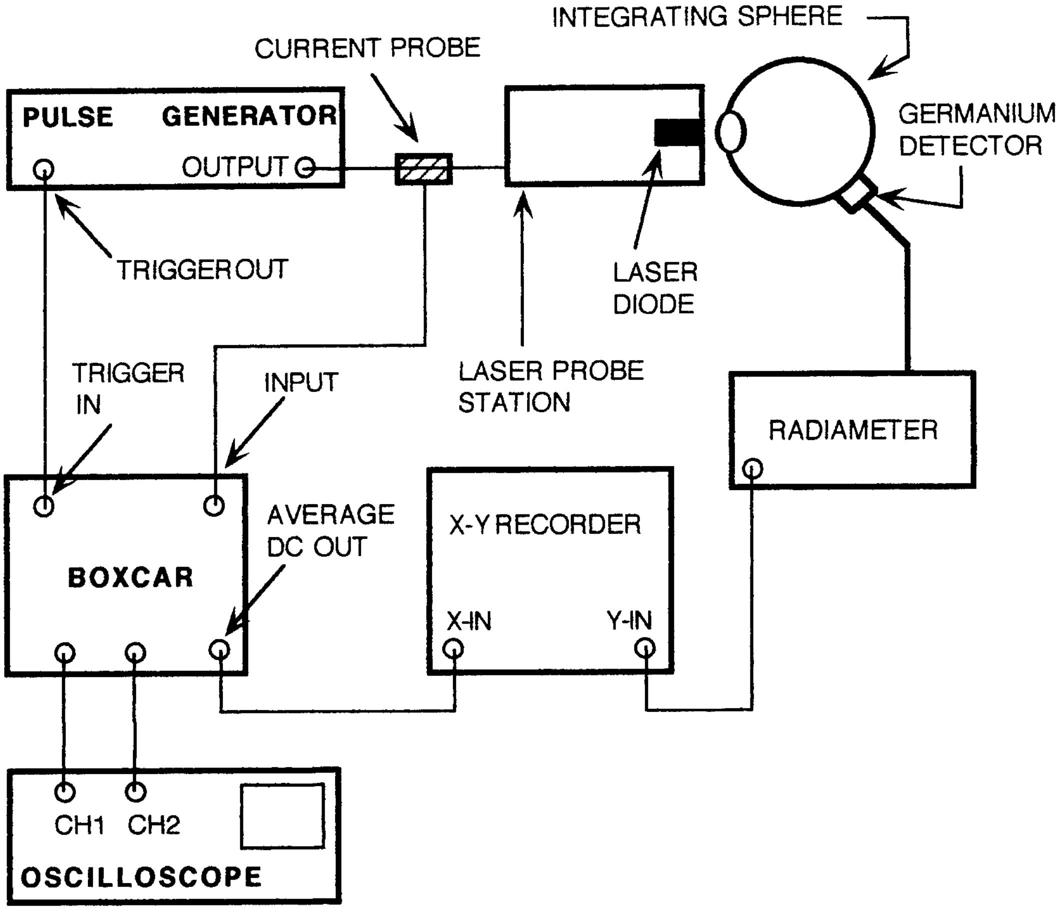
INTEGRATING SPHERE
CURRENT PROBE
PULSE GENERATOR
OUTPUT
GERMANIUM DETECTOR
TRIGGER OUT
LASER DIODE
TRIGGER IN
INPUT
LASER PROBE STATION
RADIAMETER
AVERAGE DC OUT
X-Y RECORDER
BOXCAR
X-IN
Y-IN
CH1
CH2
OSCILLOSCOPE

Figure 4.1 Experimental setup for measurement of the output light power of laser diodes emitting at 1.3 μm wavelength. An integrating sphere equipped with a germanium detector is used to collect the light. The laser probe station is equipped with a thermoelectric cooler-heater for temperature adjustment.

4.2.2 Threshold current density

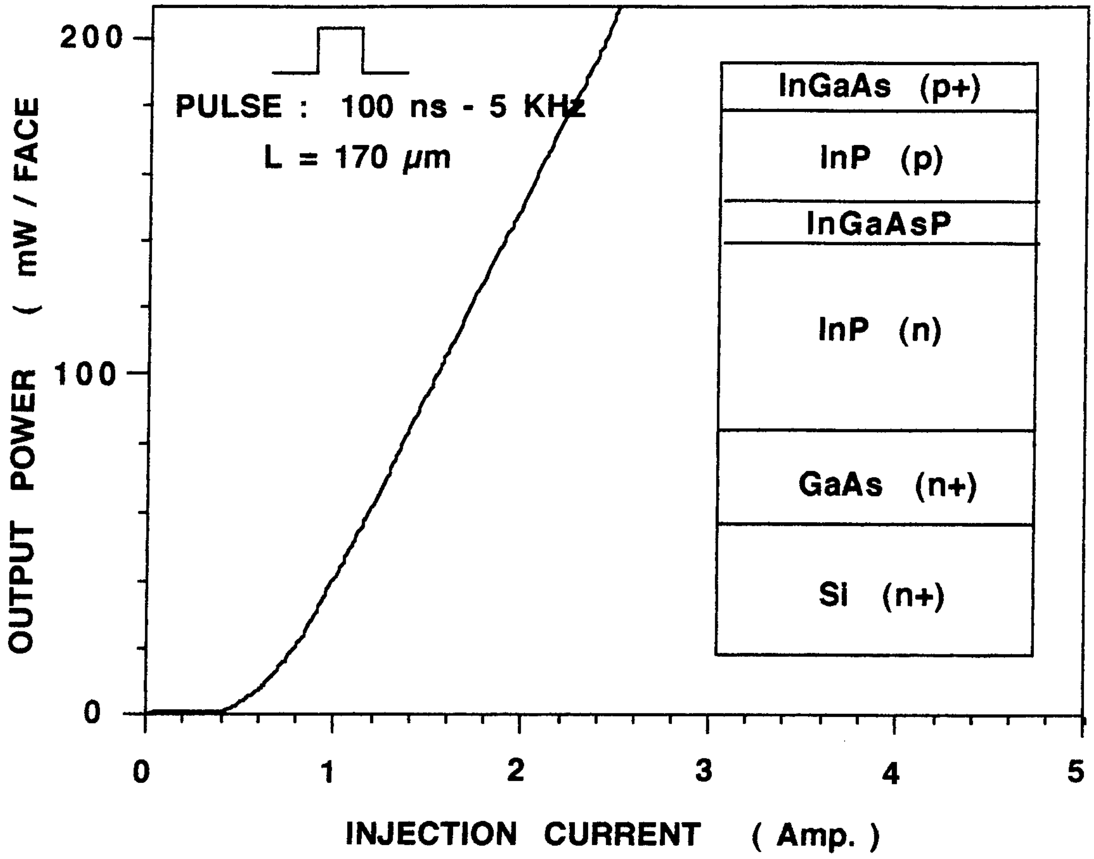

Figure 4.2 Pulsed (100ns-5kHz) light-current characteristic for a 170 μm long (20 μm side stripe) laser with both facets as cleaved. Output power exceeds 200 mW per facet. The inset shows the laser structure.

Figure 4.2 shows the light versus current (L-I) characteristic of one laser diode. In order to understand the behavior of the L-I curve shown in figure 4.2 it is necessary to introduce a simple model describing the variations of the output power with increasing injection current. The rate equations governing the behavior of the laser are introduced in the section regarding the spectrum analysis of the devices. Based on these equations the solution to the carrier density rate equation at steady state is given by

$$J = qd\,R(n) \qquad (4.1)$$

where J is the current density, q is the electron charge, d is the thickness of the active region, and R(n) is the recombination rate which is a function of the carrier density n and takes into account the carrier loss owing to various recombination processes both radiative and nonradiative. The general expression for R(n) is

$$R(n) = A_{nr}n + Bn^2 + Cn^3 + R_{st}N_{ph} \tag{4.2}$$

where A_{nr} is the nonradiative recombination coefficient due to such mechanisms as trap or surface recombination, B is the spontaneous radiative recombination coefficient, C is the nonradiative Auger recombination coefficient. The last term; $R_{st}N_{ph}$ is due to stimulated recombination that leads to coherent emission of light. with R_{st} and N_{ph} being the net rate of stimulated emission and the photon density inside of the cavity respectively. The net rate of stimulated emission is determined by the optical gain parameter g(n) through: $R_{st} = [c/n_g][g(n)]$ where c is the speed of light, and n_g is the group index of refraction. Since below threshold there is no stimulated emission this last term in equation 4.2 (i.e. $R_{st}N_{ph}$) can be neglected in the analytical process leading to an expression for the threshold current density; J_{th}.

The total recombination rate R(n) is a function of the carrier density n. Threshold is reached when n achieves n_{th} value. At this point the gain equals loss. This is shown as

$$\begin{aligned} \Gamma g &= \alpha_{loss} \\ &= \alpha_{int} + \alpha_m \\ &= \Gamma\alpha_{ac} + (1-\Gamma)\alpha_{ex} + \frac{1}{L}\ln\left(\frac{1}{R}\right) \end{aligned} \tag{4.3}$$

where G is the confinement factor, g is the gain, L is the cavity length, R is the mirror reflectivity, a_m is the loss due to the mirrors and a_{int} is the internal loss parameter. a_{int} consists of two parts; Ga_{ac} and $(1-G)\alpha_{ex}$. These correspond to the loss from the portion of the optical wave propagating inside and outside the active region of the material respectively. The gain parameter can be shown to be a function of the carrier density n as follows

$$\begin{aligned} g &= A(n - n_o) \\ &= An - An_o \\ &= An - \alpha_{in} \end{aligned} \tag{4.4}$$

where A is the gain coefficient indicating the rate at which the peak gain value g increases with increasing carrier density n and n_o is the injected carrier density at which gain takes a non zero value and is basically the onset of population inversion. The term An_o is defined as a_{in} the absorption of the unpumped material. Solving equation 4.4 for n at threshold gives

$$\begin{aligned} n_{th} &= \frac{g_{th}}{A} + \frac{\alpha_{in}}{A} \\ &= \frac{\alpha_{loss}}{A\Gamma} + \frac{\alpha_{in}}{A} \\ &= \frac{1}{A}\left[\alpha_{in} + \alpha_{ac} + \left(\frac{1-\Gamma}{\Gamma}\right)\alpha_{ex} + \frac{1}{\Gamma L}\ln\left(\frac{1}{R}\right)\right] \end{aligned} \tag{4.5}$$

Substituting the value of n_{th} from equation 4.5 in place of n in equation 4.2 (and neglecting the stimulated emission term in equation 4.2) gives an expression for the recombination rate at threshold. Using this term in equation 4.1 results in an expression for J_{th} as given below

$$J_{th} = qd\, n_{th}\left[A_{nr} + Bn_{th} + Cn_{th}^2\right] \tag{4.6}$$

where n_{th} is defined by equation 4.5 and the term in the brackets of the above expression is defined as the inverse of carrier lifetime at threshold; t_e. Using this definition equation 4.6 can be written in the more concise form shown below

$$J_{th} = \frac{qd\, n_{th}}{\tau_e} \tag{4.7}$$

The simple expression obtained for the threshold current density in equation 4.7 along with the definitions for the carrier density and carrier lifetime at threshold shown in equations 4.5 and 4.6 are important relationships. These will be used to determine the key parameters affecting the threshold current density of a semiconductor laser. Of particular interest are the variations of J_{th} with increasing temperature and the physical phenomena responsible for this.

From equations 4.5 and 4.7 it is also observed that the threshold current density increases linearly as the inverse cavity length 1/L increases. This is experimentally verified and shown in figure 4.3.

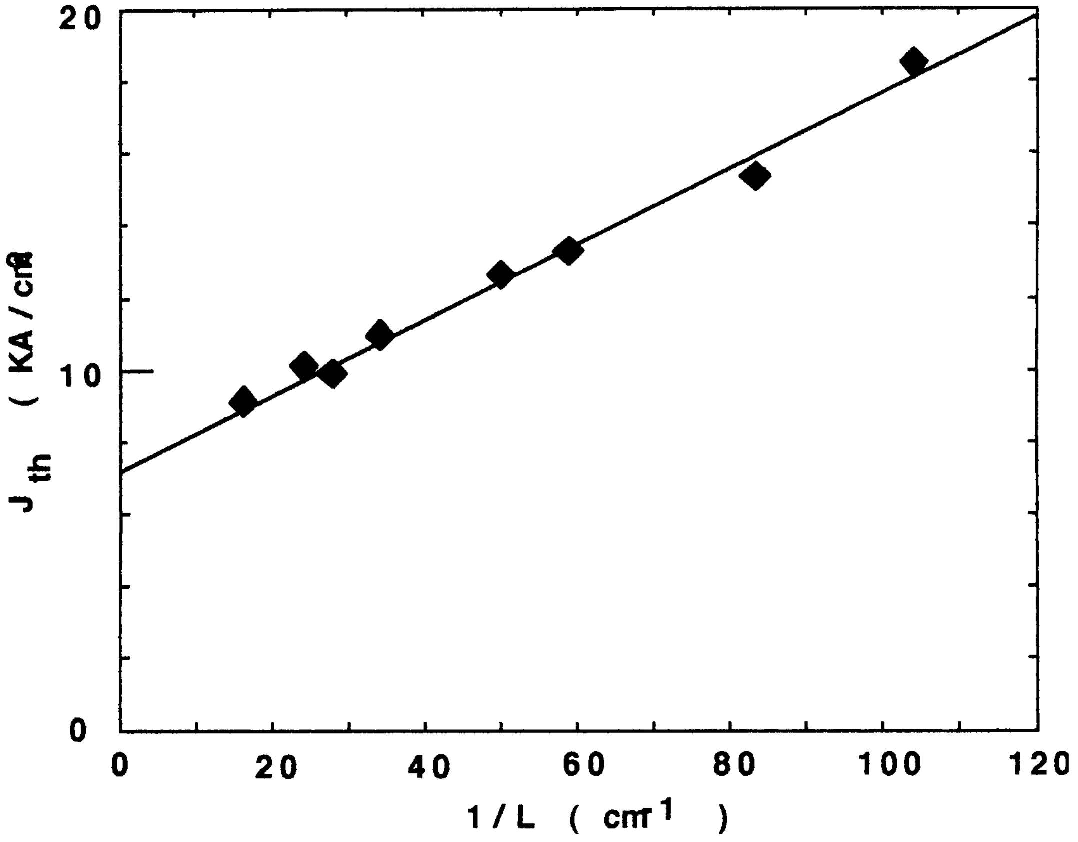

Figure 4.3 The threshold current density J_{th} versus the inverse cavity length 1/L for lasers with cavity lengths between 95 μm and 590 μm.

4.2.3 Output light versus injection current curve

Figure 4.2 shows that once the threshold is reached further increase in current results in a linear increase in the coherent output light power of the laser. Using equations 4.1 and 4.2 it can be shown that the photon density; N_{ph} inside the laser cavity is given by

$$N_{ph} = \eta_i \left(\frac{\tau_p}{qd} \right) (J - J_{th}) \tag{4.8}$$

where t_p is the photon lifetime (the inverse of the stimulated emission rate) and is defined as t_p = (n_g/c)(a_m+a_{int})$^{-1}$. h_i is the internal quantum efficiency and it takes into account the fact that not all carriers injected into the device recombine radiatively. In other words the internal quantum efficiency is defined as the fraction of injected carriers converted into photons inside the laser cavity . Equation 4.8 shows that once the threshold is reached the photon density inside the cavity increases linearly with further increase in pump current. The photon density inside the cavity is related to the more readily measurable parameter; the output power of the laser P_{out} through the following relationship

$$P_{out} = \frac{1}{2} h\upsilon v_g \alpha_m V N_{ph} \tag{4.9}$$

where the 1/2 factor indicates that P_{out} is the power per one of the two facets of the laser, hu is energy of one photon with the specific frequency u and h is the Planck's constant, v_g is the group velocity of the optical wave defined as v_g=c/n_g. The term $v_g a_m$ is the rate at which photons escape out of the laser cavity and V is the total volume of the active region of the laser which is the product of the width w, the thickness d, and the cavity length L.

Equations 4.8 and 4.9 can be used to write an expression relating the measured parameter the injected current (I) to the output light power (P_{out}) of the laser. Threshold current I is related to the threshold current density J through I=wLJ. Thus the following can be obtained

$$P_{out} = \frac{h\upsilon}{2q}\,\frac{\eta_i \alpha_m}{\alpha_m + \alpha_{int}}\,(I - I_{th}) \qquad (4.10)$$

where I_{th} is related to J_{th} which in turn is defined by in equations 4.6 or 4.7.

$$I_{th} = \frac{qVn_{th}}{\tau_e} + I_L \qquad (4.11)$$

Also the term I_L is introduced to account for the current lost due to leakage caused by surface recombinations. I_L does not include the contribution of heterobarrier leakage which will be discussed later on.

The experimentally obtained graph of figure 4.2 agrees well with the analytical model described above. However the linear increase in the output power with increasing pump current finally saturates and further increase in injection current simply results in a decrease of the output power and the top of the curve shown in figure 4.2 begins to bow down. This effect is not shown in the case of the 170 μm long laser of figure 4.2 because the current could not be increased any more due to limitations of the pulse generator that was used. But for shorter cavity lasers having a smaller threshold current this was clearly observed. This behavior could be due to several reasons.

Firstly the temperature of the laser junction increases with increasing current. This higher operating temperature results in an increase in the nonradiative Auger recombination rate which is highly temperature sensitive. This in turn leads to a decrease of the carrier lifetime t_e which according to equations 4.10 and 4.11 lowers the output power of the device.

Secondly an increase in current leads to an increase in percentage leakage current. This means that less current is used to inject carriers into the active region of the laser.

Thirdly an increase in the internal loss parameter a_{int} is caused by increasing the threshold current. This means that a smaller fraction of the generated photons find their way into the output power value and a higher number of them get absorbed before leaving the laser cavity.

So far the linear behavior of the experimentally obtained L-I curve has been analytically discussed and an expression relating J_{th} to fundamental material parameters has been given. Another important parameter to consider is the slope of the L-I curve which is a measure of the laser efficiency in converting injected electric power into output optical power. This efficiency factor is referred to as the differential quantum efficiency and is discussed below.

4.2.4 External differential quantum efficiency

It has already been mentioned that not all carriers injected into the laser diode convert into photons. The fraction of carriers converted into photons is referred to as the internal quantum efficiency. Once the photons are generated inside the laser cavity not all of them find their way outside to contribute to the output power. A number of them get absorbed by various absorption mechanisms which are also highly temperature dependent. This will be elaborated later on. The product of the internal quantum efficiency with the ratio of the photons that do escape from the cavity over the rate of total photons generated is referred to as the external differential quantum efficiency; h_d. This is summarized in the following relationship.

$$\eta_d = \left[\frac{\text{radiative recombination rate}}{\text{total recombination rate}}\right] \text{x} \left(\frac{\text{photon escape rate}}{\text{photon generation rate}}\right) \qquad (4.12)$$

where the fraction in the brackets is the internal quantum efficiency h_i and its complete form is

$$\eta_i = \frac{\text{radiative recombination rate}}{\text{total recombination rate}} = \frac{Bn^2 + R_{st}N_{ph}}{A_{nr}n + Bn^2 + Cn^3 + R_{st}N_{ph}}$$

$$= \frac{\frac{1}{\tau_r}}{\frac{1}{\tau_{nr}} + \frac{1}{\tau_r}} \tag{4.13}$$

where B is the spontaneous recombination coefficient and t_r and t_{nr} are the radiative and nonradiative recombination lifetimes respectively.

As mentioned earlier at steady state photons are generated at a rate of $1/t_p$ and escape out of the laser cavity at a rate of $u_g a_m$. Remember that $t_p = (n_g/c)(1/a_m+a_{int}) = [v_g(a_m+a_{int})]^{-1}$. Thus equation 4.12 can be written as

$$\eta_d = \eta_i \frac{\upsilon_g \alpha_m}{1/\tau_p} = \eta_i \frac{\alpha_m}{\alpha_m + \alpha_{int}} \tag{4.14}$$

Notice that the expression obtained for h_d in equation 4.14 is the derivative of output power with respect to input current from equation 4.10 where h_d is directly related to the slope of the L-I curve as shown below

$$\eta_d = \frac{2q}{h\upsilon} \frac{\partial P_{out}}{\partial I} \tag{4.15}$$

The term $\partial P_{out} / \partial I$ in equation 15 is the slope of the L-I curve such as shown in figure 4.2. Its unit is W/A and it basically conveys the information that for every 1 Ampere increase of current how many Watts the power goes up. By multiplying this term by the 2q/hu factor the external differential quantum efficiency is obtained which is a dimensionless quantity, as obvious from expression given in equation 4.12, and is usually given in percentage form. The relationship shown in equation 4.15 could be understood intuitively in a simple manner described below.

In an ideal case every injected carrier (with an electric charge of 1 q) recombines radiatively to result in a photon outside the cavity (with an energy of hu Joules). In this situation the efficiency is 100 % and all the generated photons inside the cavity escape to contribute to the output power. 100 % efficiency is the case of a laser diode that perfectly converts all the electric power it receives into coherent output power. Now the point of interest is that how does the laser whose L-I curve is shown in figure 4.2 compare with a 100 % efficient device ? In other words what is the external differential quantum efficiency of the device ? The differential quantum efficiency is given as the ratio of the slope of the laser tested to the slope of a 100 % efficient laser

$$\eta_d = \frac{\partial P_{out} / \partial I}{h\upsilon / q} \tag{4.16}$$

The above expression is essentially the same as the one given in equation 4.15 except that in equation 4.15 there is an extra factor of 2 corresponding to the fact that the output power measured is only from one facet and amounts to only half the total output power of the laser. In these series of experiments both facets of the laser were as cleaved with no anti reflection or high reflectivity coatings applied to them. The external differential quantum efficiency of the 170 μm long cavity laser of figure 4.2 was determined to be about 23 % for 2 mirrors and as observed there is no sign of any non linearity or kinks.

Through slight rearrangements of the terms of equation 4.14 a useful relationship can be obtained for the external differential quantum efficiency such as shown below

$$\frac{1}{\eta_d} = \frac{1}{\eta_i}\left[1 + \frac{\alpha_{int}}{\ln(1/R)} L\right] \tag{4.17}$$

Equation 4.17 is an important relationship. By measuring the external quantum efficiency of a number of lasers with different cavity lengths and plotting the cavity length dependence of the inverse external quantum efficiency it is possible to directly determine the value of both the internal quantum efficiency h_i and the total internal loss a_{int} . The former obtained from the vertical axis intercept and the latter related to the slope of the linear fit.

Figure 4.3 shows the measured threshold current densities of laser diodes with cavity lengths ranging from about 100 μm up to 600 μm . More than 20 lasers of each cavity length were tested. The external differential efficiencies of these lasers were also measured and the results are plotted in figure 4.4. From this data, using the discussion and equations presented above, the internal quantum efficiency was calculated to be h_i=33% with a corresponding internal loss of a_{int}=39 cm^{-1}.

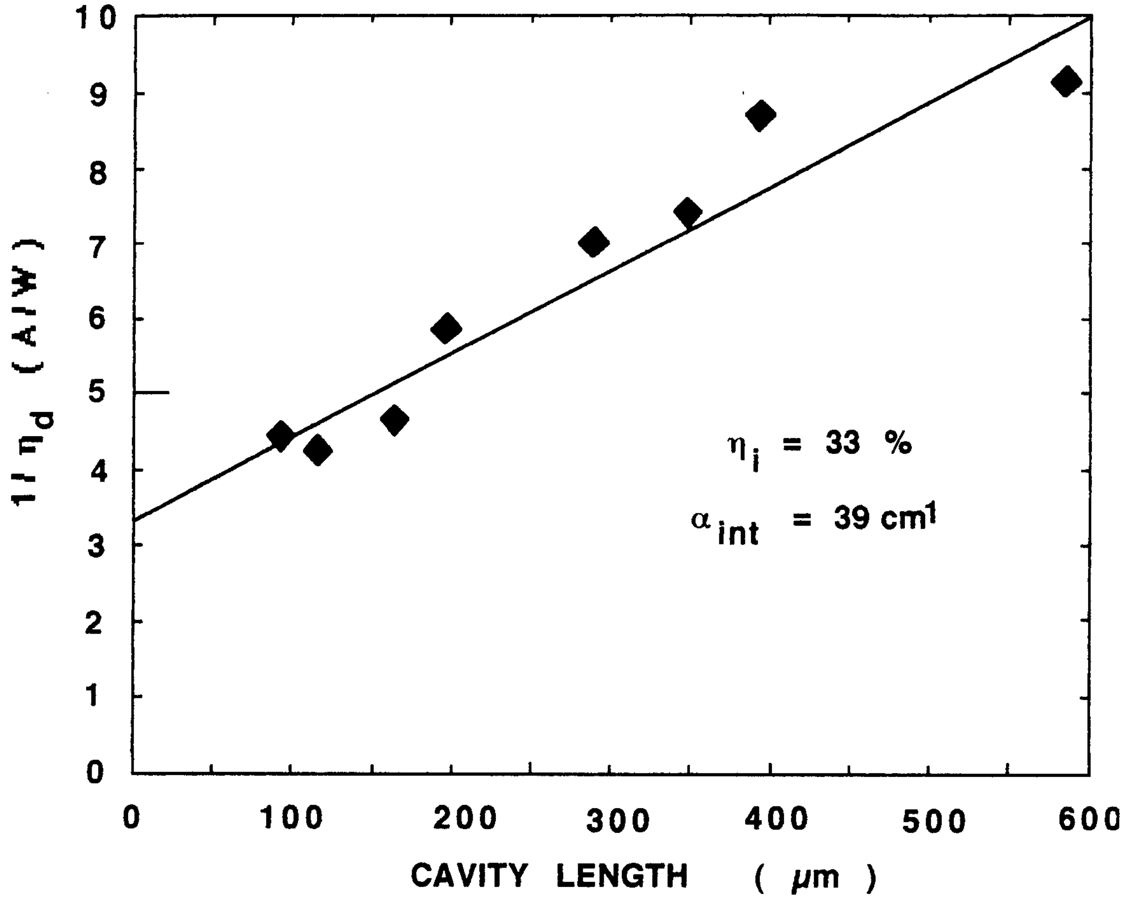

Figure 4.4 The cavity length dependence of the inverse external differential quantum efficiency. The extrapolated internal quantum efficiency is 33 % and the internal loss is 39 cm^{-1} .

4.3 Temperature Sensitivity of the Threshold Current and External Differential Quantum Efficiency

4.3.1 Calculation of the characteristic temperature T_O of a laser operating under pulse condition

The threshold current density of the semiconductor lasers varies with temperature according to the following relationship

$$J_{th} = J_o \exp[T/T_o] \tag{4.18}$$

where J_O is a constant and T_O is the characteristic temperature. T_O is a measure of the temperature sensitivity of the device. A higher T_O value implies that the threshold current density increases less rapidly with increasing temperature and thus the laser is more stable. Generally InGaAsP lasers have a lower T_O value (typically 40 K to 70 K under continuous wave CW, operation) compared to the conventional AlGaAs lasers which usually have T_O values of above 120 K. The high temperature sensitivity of these lasers can be understood by considering three effects; the intervalence band absorption, heterobarrier leakage, and nonradiative Auger recombination. Later on in this section it will be explained how each of these phenomena affect the threshold current density and the external differential efficiency of the laser. However for the moment the point of interest is to determine the T_O value of the lasers tested here. Improvement of the T_O parameter is an important concern because the high temperature sensitivity of the InGaAsP lasers highly limits their performance particularly under CW conditions. As more and more current is pumped into the device to offset the loss of power due to increasing temperature the actual temperature of the device increases further and in this manner a thermal runaway process is created that limits the maximum power emitted by the laser diode.

Figure 4.5 shows the L-I curves of a 95 μm long laser at different temperatures. The laser tested here is a broad area laser and was not bonded on heat sinks. For this reason the T_O

measurement was performed under pulse condition (100nsec / 5kHz) with a duty cycle of 0.05 %. The characteristic temperature obtained in this way is of course higher than one that would have been measured under CW condition but nevertheless it provided a quick feedback regarding the temperature sensitivity of the laser.

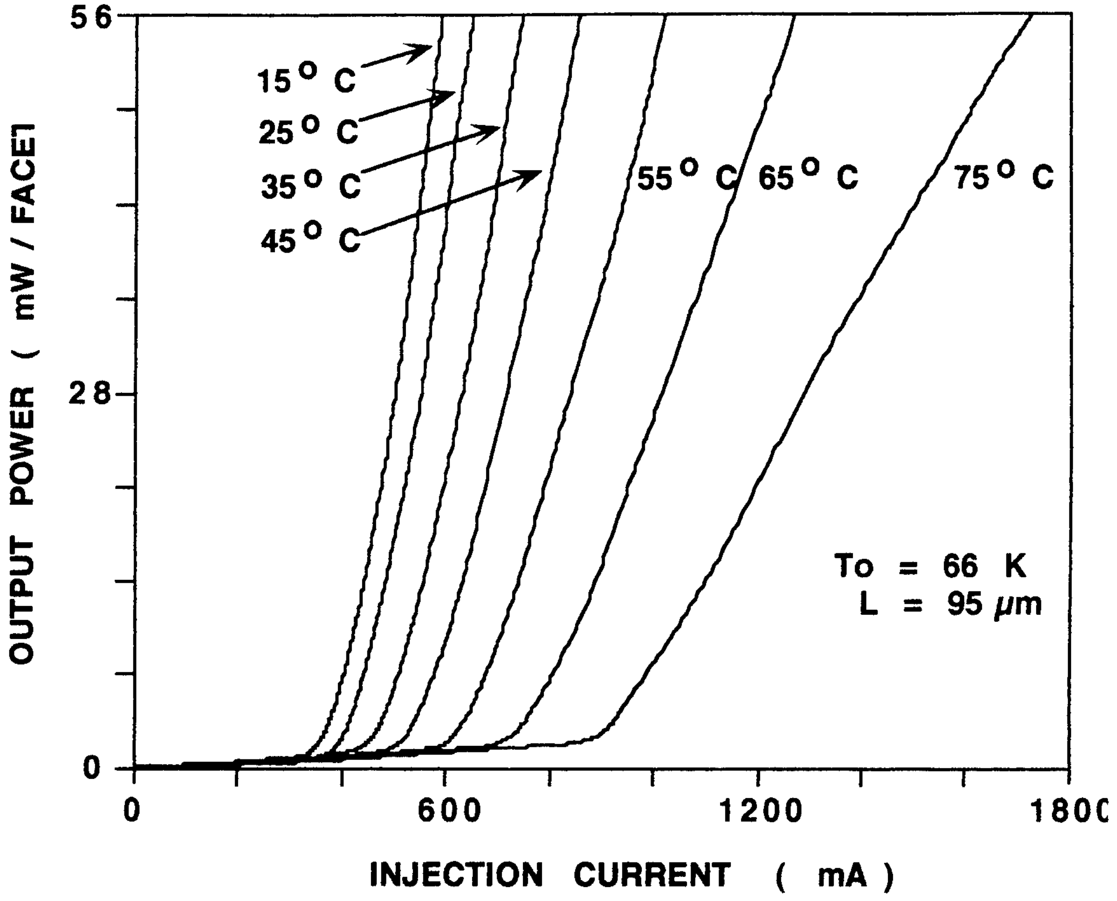

Figure 4.5 Light-current characteristic for a 95 μm long (20 μm wide stripe) broad area laser at various temperatures ranging from 15 ^{o}C up to 75 ^{o}C.

Starting with equation 4.18 the process of finding the characteristic temperature is outlined below

$$J_{th} = J_o \exp[T/T_o] \tag{4.19-a}$$

$$\ln\left[\frac{J_{th}}{J_o}\right] = \frac{T}{T_o} \tag{4.19-b}$$

$$\ln(J_{th}) - \ln(J_o) = \frac{T}{T_o} \qquad (4.19\text{-c})$$

$$\partial \ln(J_{th}) = \frac{1}{T_o}\,\partial T \qquad (4.19\text{-d})$$

$$T_o = \frac{\Delta T}{\Delta \ln(J_{th})} \qquad (4.19\text{-e})$$

where in equation 4.19-e the symbol D reflects a change in the related parameter.

From figure 4.5 the following data has been extracted carefully. These data along with equation 4.19-e will lead to determination of T_o.

T (**°C**)	**Ith** (**mA**)	**Jth** (**A/cm^2**)
15	340	17895
25	375	19737
35	435	22895
45	485	25526
55	600	31579
65	705	37105
75	870	45789

Using the data tabulated above the T_o of the laser operating under pulse conditions for temperature range of 1 5 °C to 7 5 °C is determined to be 66 K. This is done by plotting J_{th} points from the above table versus T on a logarithmic scale and measuring the slope of the linear fit line as shown in figure 4.6.

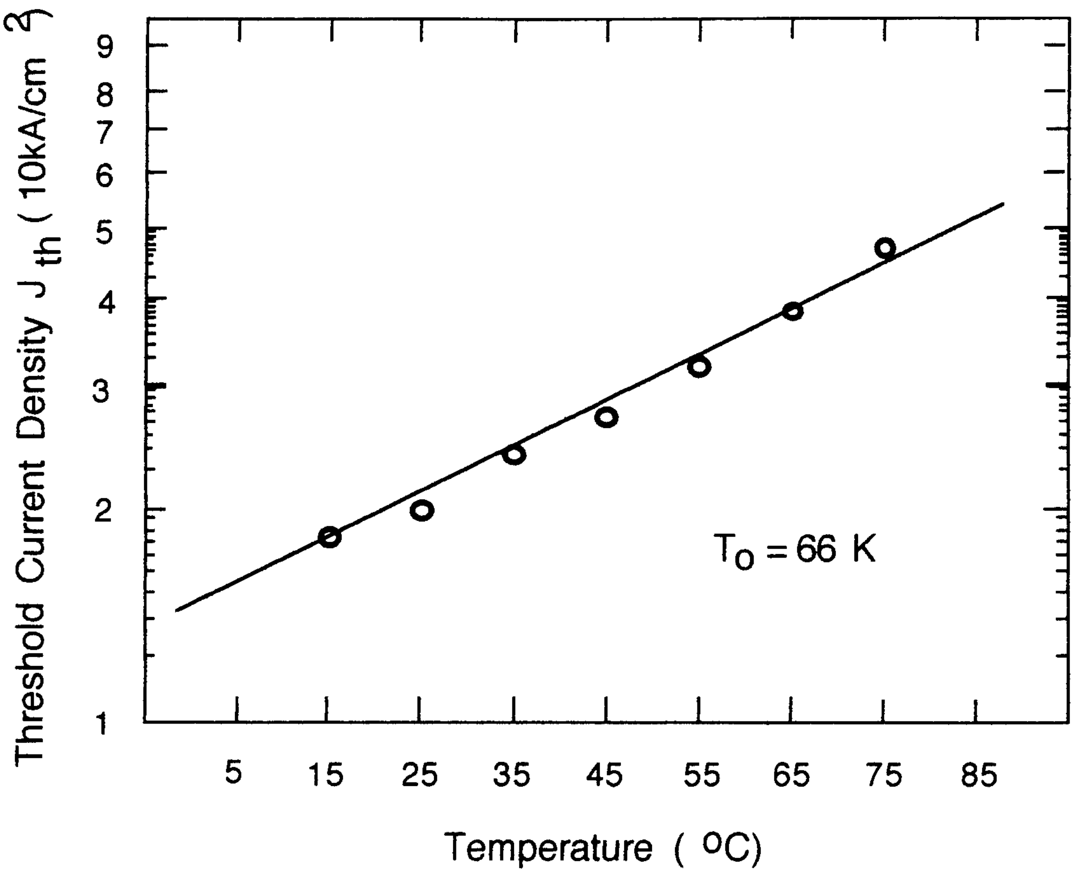

Figure 4.6 Variations of J_{th} with rising temperature for a 95 μm long laser operating under pulse condition. The solid line is a linear fit and from its slope T_o is deduced.

4.3.2 Temperature dependency of J_{th} and h_d

In order to determine how J_{th} and h_d are affected by variations in temperature it should be made clear which parameters govern the behavior of J_{th} and h_d. Using equation 4.1 and remembering that the recombination rate R(n) is the same as the inverse of the total carrier lifetime the full blown expression for the threshold current density can be written, using also the definition for the threshold carrier density n_{th} from equation 4.5, as

$$J_{th} = \frac{qd}{A}\left[\alpha_{in} + \alpha_{ac} + \left(\frac{1-\Gamma}{\Gamma}\right)\alpha_{ex} + \frac{1}{\Gamma L}\ln\left(\frac{1}{R}\right)\right]\left[\frac{1}{\tau_{nr}} + \frac{1}{\tau_r}\right] \quad (4.20)$$

where

$$\frac{1}{\tau_r} + \frac{1}{\tau_{nr}} = \left[Bn^2 + R_{st}N_{ph}\right] + \left[A_{nr}n + Cn^3\right] \quad (4.21)$$

and the stimulated emission term $R_{st}N_{ph}$ can be neglected at or below threshold.

Similarly the full blown expression for the external differential quantum efficiency can be obtained from equations 4.13 and 4.14 and is given as

$$\eta_d = \eta_i \frac{\frac{1}{L}\ln\left(\frac{1}{R}\right)}{\Gamma\alpha_{ac} + (1-\Gamma)\alpha_{ex} + \frac{1}{L}\ln\left(\frac{1}{R}\right)} \quad (4.22)$$

where the internal quantum efficiency h_i is defined in equation 4.13 as the ratio of the nonradiative carrier lifetime over the total carrier lifetime.

Basically three important physical effects govern the temperature sensitivity of J_{th} and h_d. These are intervalence band absorption, heterobarrier leakage, and nonradiative Auger recombination and each will be elaborated on in the following sections. Intervalence band absorption manifests itself through the active layer loss coefficient a_{ac}, while heterobarrier leakage and Auger recombination mechanisms exert their influence through the nonradiative recombination coefficient A_{nr}, and Auger coefficient C, respectively. In other words the nonradiative recombination and carrier leakage influence the carrier lifetime while the intervalence band absorption affects the loss. Each one of these mechanisms is highly temperature sensitive and in the following section it will be explained how their behavior determines the overall temperature sensitivity of J_{th} and h_d.

4.3.3 Effect of intervalence band absorption

From figure 4.5 a sharp decrease in the differential quantum efficiency h_d is observed at temperatures above room temperature. This is believed to be due to the absorptions caused by the transition of electrons from the split-off valence band into the acceptor level and into the holes within the heavy hole valence band. These holes are either from thermally excited acceptors or are injected electrically by forward biasing of the laser diode. These transitions are schematically shown in figure 4.7.

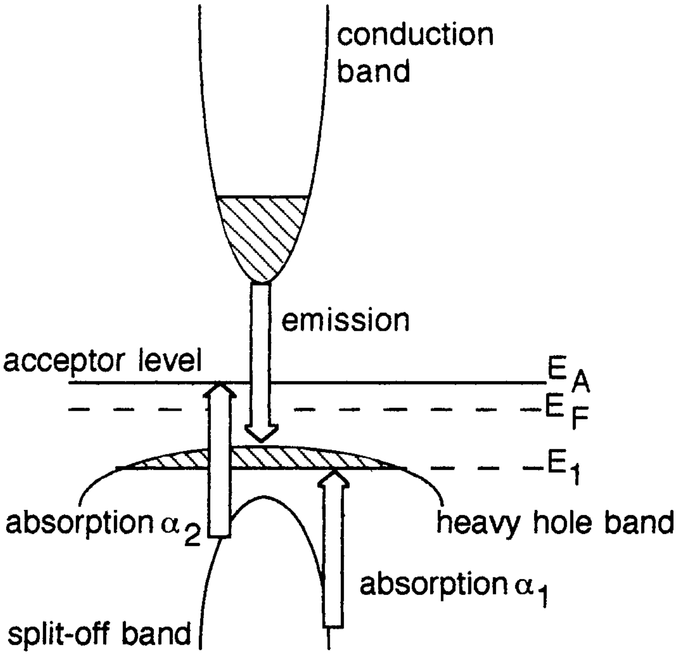

Figure 4.7 Absorption of emitted photons by transitions from the split-off band into the heavy hole band at energy E_1. This absorption is referred to a_1. The transition into the acceptor level at energy E_A is referred to as a_2 [43].

The absorption loss coefficient in the active layer a_{ac} is due to the sum of these two main effects. The absorption a_2 due to transitions from the valence band into impurity levels is not strongly temperature dependent since it is related primarily to the energy difference between acceptor energy level E_A and Fermi level energy E_F. However a_1 which is due to absorption from lower lying bands into the holes positioned at the maximum point of the valence band is strongly temperature dependent for temperatures at or above room temperature. This is because it is mainly proportional to the difference between the Fermi level energy and the lowest energy hole and this difference is always increasing with temperature. The overall effect is that the absorption loss coefficient in the active layer a_{ac} rises slowly with temperature up to about room value and then increases rapidly [44].

Based on the above arguments as temperature rises J_{th} will also increase slowly until about room temperature and after that they increase rather rapidly. This explains the temperature variation of J_{th}, but it is important to keep in mind that the absolute value of J_{th} is determined by nonradiative recombination mechanisms. In summary the fact that the threshold current of the laser increases so rapidly near the room temperature is partially due to the increase in the intervalence band absorption [45-46] in addition to heating effects caused by thermal runaway process due to injection of high current levels.

4.3.4 Auger recombination process

Auger mechanism is a nonradiative recombination process in which the recombination of an electron with a hole releases energy which is used to excite another electron from its bound state instead of resulting in the emission of a photon. This is shown schematically in figure 4.8.

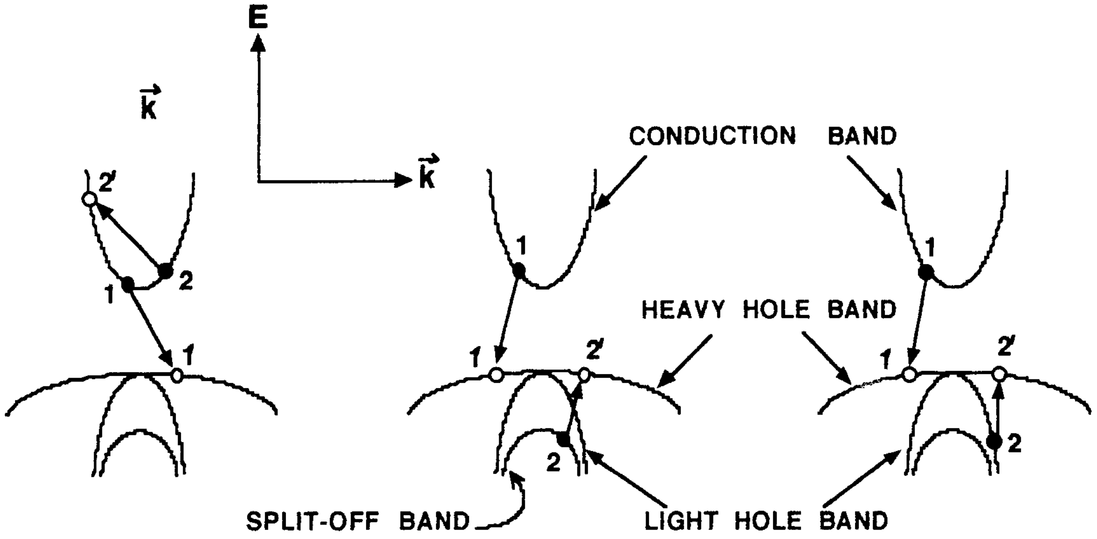

Figure 4.8 Three different band to band processes shown schematically. Electrons are represented by closed circles and holes by open circles [47].

For example in the first diagram the Coulomb interaction between the two electrons in the conduction band results in recombination of one of them with the hole in the valence band. The energy released from this process is used to excite the other electron to a higher state in the conduction band.

Another variation of the Auger process described above is one in which the participation of a phonon is included too. This is referred to as the phonon assisted Auger process in which the Coulomb interaction causes a heavy hole to interact with a phonon before reaching its final state.

Auger processes are strongly temperature dependent and affect the threshold current density and the external differential quantum efficiency through the Auger coefficient C. They are also much dependent on the bandgap of the material. In the case of relatively large bandgap material systems such as GaAs/AlGaAs their effect is almost negligible but for InGaAsP/InP Auger processes result in high temperature sensitivity . This is due to momentum conservation and energy laws governing the behavior of the four particles (i.e. electrons and holes as shown in figure 4.8) involved in the interaction and was first derived and explained in 1959 by Beattie and Landsberg [48] and since then have been studied and elaborated else where in the literature [49-56].

Essentially through the Auger process an electron is brought from the conduction band down to the valence band. This electron will be eventually excited back to the conduction band through the absorption of photon and thus contributes to total photon losses. This new source of photon loss has to be counteracted by an increase in the threshold current density.

From empirical approximations for the Fermi energy in a semiconductor with parabolic bands it is understood [57] that the threshold carrier density in an ideal case $n_{th(ideal)}$; where there are no losses, is proportional to $[T]^{3/2}$, where T is the temperature. However the total loss of photons in a real laser results in a value of threshold carrier density n_{th}, that is larger than the ideal case. This increase in n_{th} is related to the ratio of the total photon losses $A+Cn^2$ and the radiative transitions Bn in the form shown below

$$n_{th} = n_{th\,(ideal)} \left[1 + \frac{A + Cn^2_{th\,(ideal)}}{Bn_{th\,(ideal)}} \right] \tag{4.23}$$

where the ideal threshold carrier density is dependent on temperature according to

$$n_{th\,(ideal)} \;\alpha\; \left[\frac{T}{300} \right]^{3/2} \tag{4.24}$$

Consequently, in addition to directly influencing the threshold current density through the nonradiative lifetime term, Auger process affects it through the threshold carrier density parameter too.

It was mentioned earlier that band to band and phonon assisted mechanisms both contribute to the overall Auger effect, however, because of the energy and momentum kinematics involved the phonon assisted mechanism is generally weakly temperature dependent and dominates for temperature range below about 200 K where radiative recombination dominates [47, 51]. The band to band mechanisms are much more temperature dependent and exert a more important effect at higher temperatures (i.e. room temperature and above). This is a direct cause of the break point of the threshold current density versus temperature curve in which passed a certain breakpoint temperature the variations of J_{th} with T become much more rapid. The Auger process is a much stronger effect in influencing the threshold current density of the laser than the intervalence band absorption mechanism described in the previous section.

The presence of the Auger recombination can be seen in the form of strong sublinearities of the spontaneous emission versus injection current curve of the laser. These sublinearities are typical of InGaAsP lasers operating below their threshold current; in the light emitting diode mode, and are generally not observed in GaAs/AlGaAs lasers where Auger mechanisms are negligible. This is primary due to the larger bandgap of GaAs compared to InGaAsP.

Auger process is an intrinsic material property and not much can be done to overcome it and shows a strong presence in all material that could possibly be used for coherent emission at 1.3 μm wavelength [47].

4.3.5 Heterojunction leakage mechanism

Electrons and holes can leak from the active layer of the laser into the adjacent cladding layers due to two forces; diffusion and drift. This leakage mechanism leads to an increase of threshold current of the laser. The effect is due to both electrons and holes. However, since electrons have a larger diffusion length, a higher mobility, and a lower effective mass compared to holes, the hole leakage is negligible compared to electron leakage which is the dominant process.

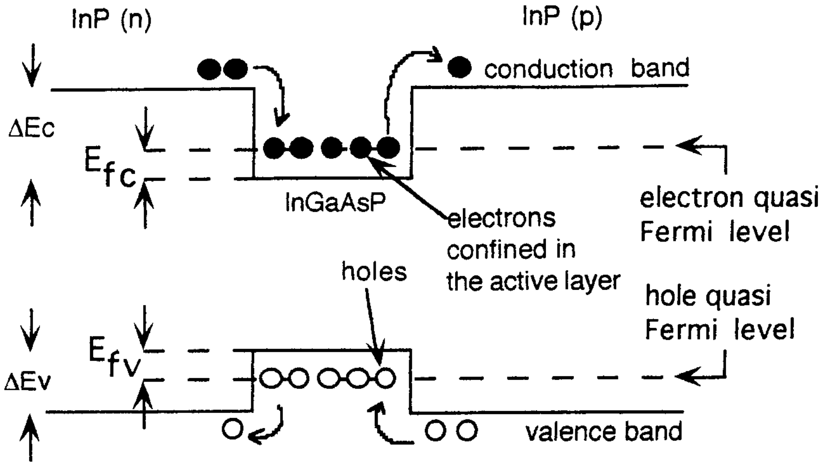
InP (n)
InP (p)
conduction band
ΔEc
Efc
InGaAsP
electrons confined in the active layer
electron quasi Fermi level
holes
hole quasi Fermi level
ΔEv
Efv
valence band

Figure 4.9 Schematic bandgap diagram showing the electron and hole leakage currents over the heterobarrier.

From figure 4.9 it is intuitively obvious that both a smaller heterobarrier energy DE and higher temperature facilitate the escape of the carriers from the confinement of the active region. The effect of temperature and barrier height is apparent from the expression for the electron density at the boundary of the active and cladding layers at steady state thermal equilibrium. The number of these " escapee " electrons which have an energy greater than the conduction band barrier height DE_C is related to T and DE_C according to [62]

$$n = 2\left(\frac{2\pi m_c k_B T}{h^2}\right)^{3/2} \exp\left[-\frac{\Delta E_c - E_{fc}}{k_B T}\right] \tag{4.25}$$

where E_{fc} is the electron quasi Fermi level measured from the conduction band edge of the active layer material.

Based on the assumption that the main contribution to the heterobarrier leakage current is due to electron leakage, the current associated with this is given by [62]

$$J_L = -qD_n\frac{dn}{dx} + qn\mu_n E \tag{4.26}$$

The first term represents the diffusion component and includes D_n, the electron diffusivity which is a material parameter, and the derivative of n(x) the electron concentration at a distance x inside the p cladding layer from the interface. The second term is due to drift resulting from applied electric field and is based on both carrier concentration n and the carrier mobility m_n. This equation can be solved [62] to give an expression for the leakage current density J_L with the help of the boundary condition that states the ratio at which the carriers are removed from the boundary due to current must be equal to the rate at which their concentration n is replenished. This continuity equation is

$$\frac{1}{q}\frac{dJ}{dx} = \frac{n}{\tau_e} \tag{4.27}$$

where t_e is the electron carrier lifetime in the p-cladding layer. Even though heterobarrier leakage mechanism is partially responsible for increasing the threshold current density of the laser, its effect at 1.3 μm wavelength near room temperature is not as significant as Auger process or intervalence band absorption effect [59-61].

4.4 Longitudinal Spectrum Analysis

4.4.1 Experimental measurement setup

To measure the spectrum of the laser radiation an Advantest model Q8344A optical spectrum analyzer was used. The light from the laser diode was coupled into a fiber optics line through a collimator lens system placed approximately 1 mm away from the front facet of the device. The other end of the fiber optic line was attached to the optical input of the spectrum analyzer. Using a light power meter and a system of three axes translation stages the coupling of the radiation into the fiber optics collimator was optimized. Figure 4.10 shows the schematic of the experimental setup. Since the main objective was to determine the emission wavelength no attempts were made to minimize external feed backs into the laser diode which could result in an unusual reduction of the linewidth and an increase of its sensitivity due to mechanical vibrations. This point will be elaborated later.

The light from the laser diode, after passing through the two arms of a Michelson interferometer setup, creates an interferogram. This is obtained by the motion of a movable mirror which continuously adjusts the optical path difference. The interferogram, carries information about the phase, intensity, and frequency of the input light, is read by a photo detector. The spectrum analyzer is equipped with an InGaAs photo detector with measurement range between 1 to 1.75 μm. From this interferogram, using an analog to digital converter and execution of fast Fourier transform algorithms by the analyzer computer, the spectrum of the radiation is obtained and displayed.

Due to the limitations imposed by the movable mirror in the Michelson interferometer arm of the analyzer a problem arises when attempting to measure the spectrum of lasers operating in the pulse regime. Most lasers used in these series of experiments belong to this category. To overcome this problem the lasers had to be operated at a frequency rate of 300 kHz. At such high frequencies the movable mirror essentially perceives the laser radiation as a continuous source of light. The minimum frequency to ensure accurate spectral measurements is around 250 kHz. A Hewlett Packard pulse generator was used to drive the lasers at such high frequencies while supplying currents of up to 1 amp peak value. Other than using a different generator the current injecting mechanism used to pump the laser diode here is almost exactly the same as the system used in the light power versus injection current experiment described in detail previously. An example of the spectrum obtained in the manner described here is shown in figure 4.11.

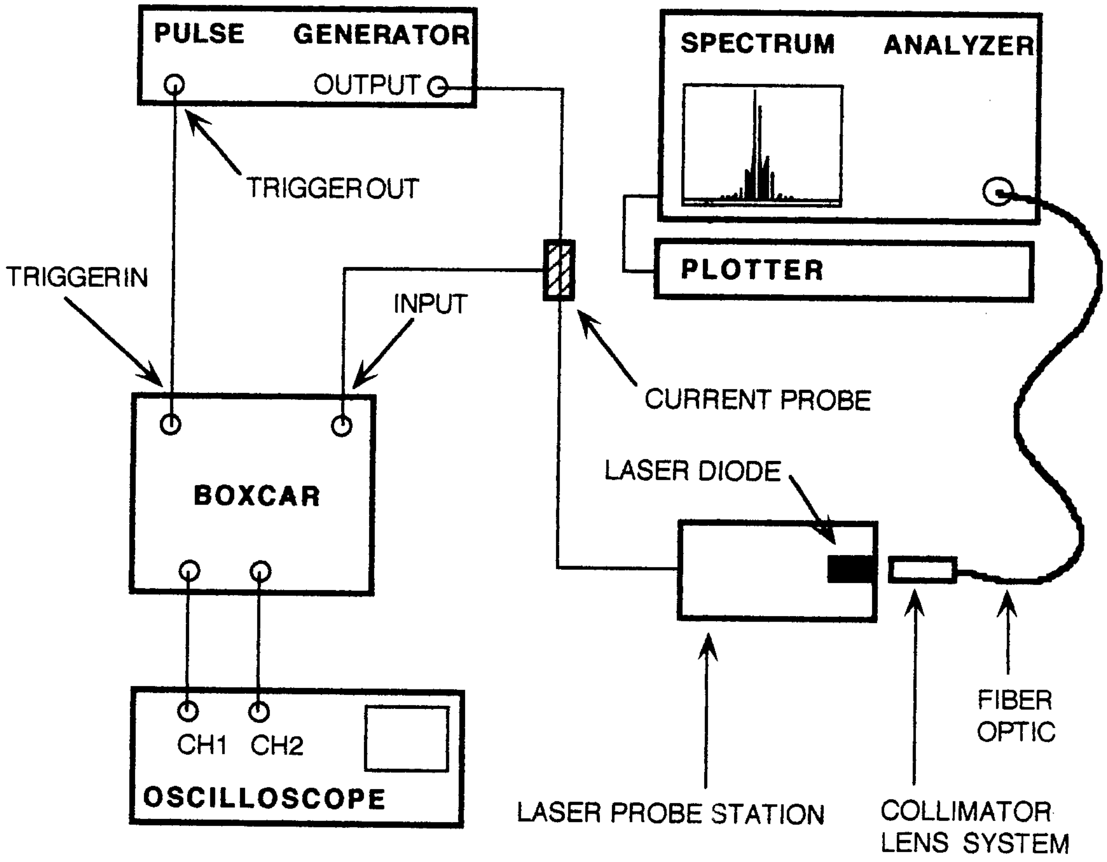
PULSE GENERATOR
OUTPUT
TRIGGER OUT
SPECTRUM ANALYZER
PLOTTER
TRIGGER IN
INPUT
CURRENT PROBE
BOXCAR
LASER DIODE
CH1 CH2
OSCILLOSCOPE
LASER PROBE STATION
COLLIMATOR LENS SYSTEM
FIBER OPTIC

Figure 4.10 The experimental setup used in driving the laser diode and measuring its output light spectrum.

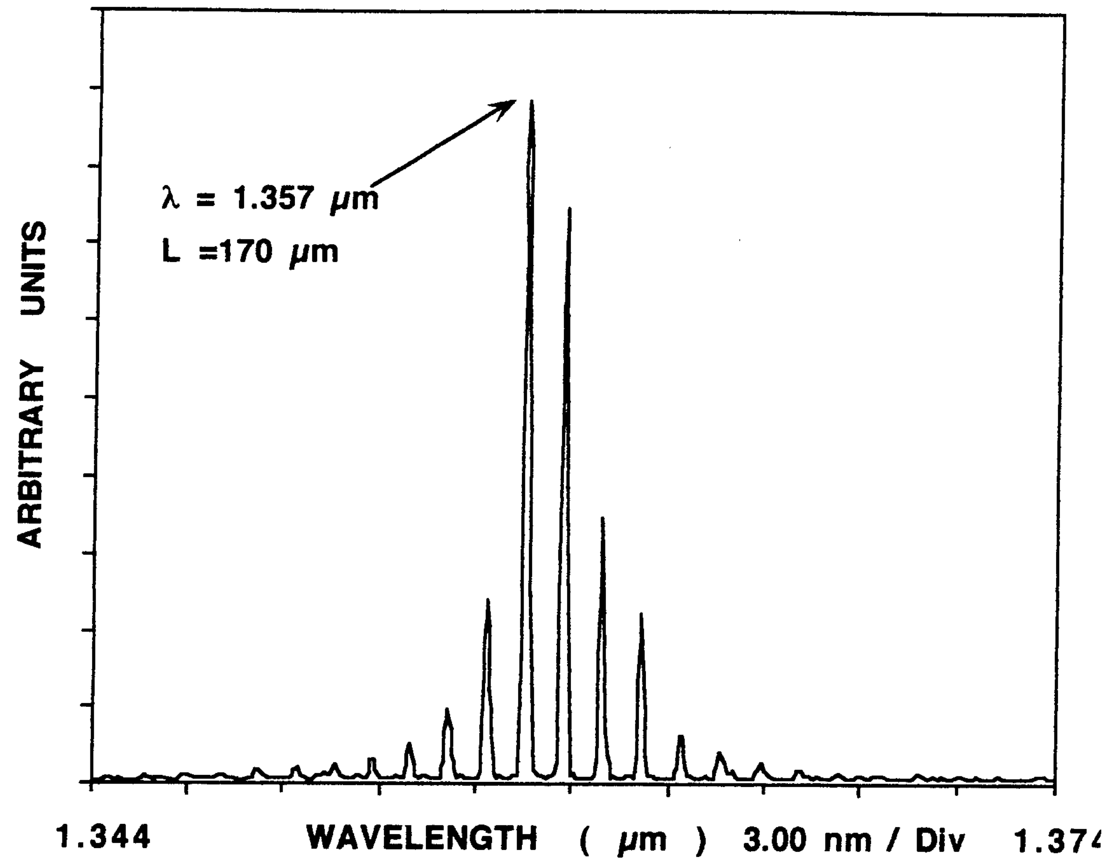

Figure 4.11 Lasing spectrum of a 170 μm cavity length laser operating at slightly above threshold. The peak wavelength is at 1.357 μm.

4.4.2 Mode spacing

The cavity of the semiconductor laser is essentially a Fabry-Perot etalon within which the optical wave propagates in the form of a standing wave. This wave is supported at its two ends by the cleaved facets of the device which act as mirrors. The cavity can resonate only if the separation between the two mirrors (L) is exactly equal to an integer multiple (m) of one half wavelength. In this manner the position of each mirror coincides with one node of the standing wave. This resonance condition can be written as

$$m = \frac{L}{\lambda/2} = \frac{n_p L}{\lambda o/2} \tag{4.28}$$

where the integer m is the mode number. L is the cavity length, l_o is the free space wavelength, and n_p is the phase index of refraction. The wavelength of the mth mode is

$$\lambda_m = \frac{2n_p L}{m} \tag{4.29}$$

and the spacing between the adjacent modes is

$$\Delta\lambda = \lambda_{m+1} - \lambda_m \approx \frac{\lambda_m \lambda_{m+1}}{2n_g L} \approx \frac{\lambda_m^2}{2n_g L} \tag{4.30}$$

where n_g is the group index of refraction of the laser medium. The group index of refraction is related to the phase index of refraction through $n_g = pn+ u(\partial p/\partial u)$. It is important to use the group index of refraction in equation 4.30 because in a semiconductor laser the index of refraction varies with frequency. Both the mode frequencies and the separation between the modes change due to variations of the refractive index caused by charge carriers pumped into the laser. Figure 4.11 shows the lasing spectrum of a 170 μm cavity length laser emitting at a peak wavelength of 1.357 μm. In order to apply the above relationship we need to have knowledge of the refractive index. The active layer of this laser is $In_{1-x}Ga_xAs_yP_{1-y}$ lattice matched to InP with fraction y being equal to 0.6. Through direct measurements [63] involving the observation of changes in the reflection caused by interference of light between the two surfaces of the epitaxial layer the refractive index of this compound emitting at approximately 1.3 μm wavelength (since $x = 0.2$) has been reported to be about 3.5 with a corresponding group index of refraction being roughly 4. Using this value the wavelength mode separation is calculated to be about 1.3 nm which is consistent with the observed value from spectrum of figure 4.11.

4.4.3 Multimode rate equations

From figure 4.11 it is obvious that the semiconductor laser is operating in a multi longitudinal mode. The intensity of each mode is built up through amplification of spontaneous emission. The amplitude of each mode is different from the adjacent modes and grows with increasing current according to the rate equations. The rate equations, essentially, relate the photon number associated with each mode and the total carrier density to the external pump parameter J; the current density of the device. The rate equations, shown below, incorporate the mechanisms by which photons and carriers are generated or lost.

$$\frac{dN_{ph(m)}}{dt} = \frac{c}{n_g}(g_m - \alpha_m - \alpha_{int})\, N_{ph(m)} + R_{sp}(\omega_m) \qquad (4.31)$$

$$\frac{dn}{dt} = \frac{J}{qd} - \left[A_{nr} + Bn + Cn^2\right] n - \frac{c}{n_g}\sum_m g_m N_{ph(m)} \qquad (4.32)$$

$N_{ph(m)}$ is the photon density of the m_{th} mode, c is the speed of light, n_g is the group index of refraction, g_m is the gain of the mth cavity mode, a_m is the mirror loss, a_{int} is the internal loss, n is the electron carrier density, J is the current density flowing through the active region of the layer with thickness d, q is the electron charge, and R_{sp} is the spontaneous emission rate and is defined as the rate at which spontaneously emitted photons are added to the intracavity photon density.

The first rate equation, basically indicates that the rate of change of the photon density in the m_{th} cavity mode equals to contributions to photon density from stimulated emission (1st. term) plus the contribution to photon density from spontaneous emission (2nd. term). The second rate equation equates the rate of change of the carrier density to the supply of carriers due to external pumping (1st. term) plus the depletion of carriers due to spontaneous recombination (2nd. term) plus the depletion due to stimulated recombination in sum of all modes (3rd. term). Before attempting to solve the rate equations in order to obtain an expression for the steady state photon flux density of each mode, it is necessary to know the form of the gain spectrum.

4.4.4 Gain spectrum

The form of the gain spectrum is not readily available and has to be either calculated numerically or measured experimentally. However a useful and simple approximation is that gain decreases quadratically from its peak value [62]. Assuming that the central mode is located at gain peak frequency w_o, with a maximum gain value of g_p, and all modes have the same loss value the mode gain is given by

$$g(\omega) = g_p \left[1 - \left(\frac{\omega - \omega_o}{\Delta\omega_g} \right)^2 \right] \tag{4.33}$$

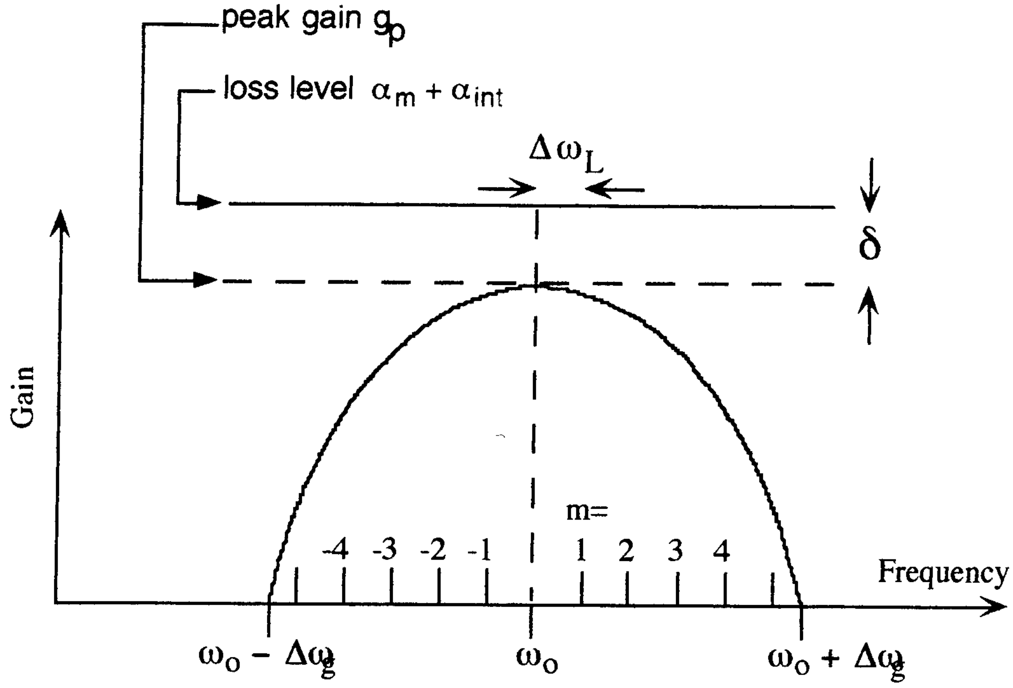
peak gain g_p
loss level $\alpha_m + \alpha_{int}$
$\Delta\omega_L$
δ
Gain
m=
-4 -3 -2 -1
1 2 3 4
Frequency
$\omega_o - \Delta\omega_g$
ω_o
$\omega_o + \Delta\omega_g$

Figure 4.12 The illustration of gain spectrum indicating the gain peak and the cavity loss level [62].

From figure 4.12 the frequency of each longitudinal mode is

$$\omega_m = \omega_o + m\Delta\omega_L \tag{4.34}$$

where

$$\Delta\omega_L = \frac{c}{2n_gL} \tag{4.35}$$

and m is the integer mode number. The largest integer M in the ratio of the frequency spread (Dw_g) on either side of the gain peak for which gain is positive over the longitudinal mode spacing and is given by

$$M \approx \frac{\Delta\omega_g}{\Delta\omega_L} \tag{4.36}$$

The mode gain approximation can thus be written as

$$g_m = g_p \left[1 - \left(\frac{m}{M} \right)^2 \right] \tag{4.37}$$

Equation 4.37 essentially gives the gain value associated with each mode.

4.4.5 Shape of the spectral envelope

Now that an expression for gain has been obtained, with the use of the rate equation , it is possible to find the photon density value corresponding to each mode. This will provide the power distribution among various side modes. At steady state, the photon density will remain constant with time, and the rate equation 4.31 will reduce to

$$N_{ph(m)} = \frac{R_{sp}(\omega_m)}{\frac{c}{n_g} \left[\alpha_m + \alpha_{int} - g_m \right]} \tag{4.38}$$

The peak gain (g_p) asymptotically approaches the loss level $(a_m + a_{int})$ and $(a_m + a_{int})$-(g_p) is inversely proportional to the main mode power so that

$$g_p = (\alpha_m + \alpha_{int})\,(1 - \delta) \tag{4.39}$$

Based on equation 4.37 and substituting 0 for m in equation 4.38 the parameter d can be defined as

$$\delta = \frac{R_{sp}(\omega_o)}{(\alpha_m + \alpha_{int})\, N_{ph(0)}} \tag{4.40}$$

where $N_{ph(0)}$ here is the photon density of the main mode. The numerical value of d depends on the spontaneous emission rate; R_{sp}, and is sensitive to fraction of spontaneously emitted photons that find their way into a lasing mode. Using the expression for g_m (equation 4.37) in equation 4.38 and using the equation 4.39 will result in

$$\begin{aligned} N_{ph(m)} &= \frac{R_{sp}(\omega_m)}{\frac{c}{n_g}\left[\alpha_m + \alpha_{int} - g_m\right]} \\ &= \frac{\frac{n_g}{c} R_{sp}(\omega_m)}{\alpha_m + \alpha_{int} - g_p\left[1 - \left(\frac{m}{M}\right)^2\right]} \\ &\approx \frac{R_{sp}(\omega_m)}{\frac{c}{n_g}(\alpha_m + \alpha_{int})} \left[\frac{1}{\delta + (m/M)^2}\right] \end{aligned} \tag{4.41}$$

From equation 4.41 it is clear that the power distribution among various side modes is approximately Lorentzian. $N_{ph(m)}$ is the photon density inside the laser cavity. It can be expressed in terms of the output power P_{out}. Assuming that both facets of the laser have the same reflectivity the power emitted from each facet is related to $N_{ph(m)}$ using equation 4.9 repeated below

$$P_{out} = \frac{1}{2} h\upsilon v_g \alpha_m V N_{ph(m)} \tag{4.42}$$

where h is the Planck's constant, u is the frequency of operation, V is the volume of the active region, and $u_g a_m$ is the rate at which the photons escape out of the laser cavity. v_g is the group velocity defined as the ratio of the speed of light in free space c, over the group index of refraction of the medium n_g. a_m is the loss due to the mirrors and is equal to (1/L)ln(1/R) where R is the mirror reflectivity.

Based on equation 4.41 the photon density of the main mode is

$$N_{ph} \approx \frac{R_{sp}(\omega_m)}{\frac{c}{n_g}(\alpha_m + \alpha_{int})\,\delta} \tag{4.43}$$

To find the full width at half maximum (FWHM) of the spectral envelope it is necessary to determine at which frequency the photon density is reduced to half the value of the main mode. This happens when $d=(m/M)^2$ which corresponds to $m=Md^{1/2}$. Remembering that $M=Dw_g/Dw_L$ the expression for the FWHM can be written as

$$\begin{aligned} \Delta\omega_s &= 2m(\Delta\omega_L) \\ &= 2\delta^{1/2}M(\Delta\omega_L) \\ &= 2\,\delta^{1/2}\,\Delta\omega_g \end{aligned} \tag{4.44}$$

Equation 4.44 shows that Dw_S; the FWHM of the spectral envelope decreases as the photon density of the main mode increases. This is because an increase in photon density results in a decrease in d which is simply a measure of how closely the peak gain approaches the total loss level . The gain peak approaches the loss level less rapidly with increasing power because of its asymptotic approach nature.

4.4.6 Spectral linewidth

In 1958 Schawlow and Townes [64] proposed the laser, predicted that its spectral linewidth would be Lorentzian, derived a formula for the linewidth, and showed that the linewidth would narrow as the laser power increases. The linewidth of the laser can be caused by external noise sources such as mechanical vibrations of the cavity. Also current fluctuations due to Johnson noise in the series resistors and shot noise in the diodes themselves may also contribute to the observed laser linewidths in addition to effects due to optical feedback to the laser from reflecting surfaces in the beam path [65]. However, in absence of any external noise, the fundamental linewidth of a laser is determined by quantum fluctuations. This is caused by the spontaneous emission of photons which give rise to time fluctuations in the complex amplitude of the optical field. These discontinuous altering of the phase and the intensity of the field translate into broadening of the frequency spectrum of the field. The detailed description of these concepts is discussed in a number of interesting papers by Charles Henry and others [66-69].

The formula derived by Schawlow and Townes is only valid below threshold. Later on Melvin Lax [70] pointed out that above threshold the linewidth is in fact twice as narrow as what is predicted by the Schawlow-Townes formula. The new formula is referred to as the modified Schawlow-Townes relation and is given as

$$\Delta f = \frac{R_{sp}}{4\pi N_{ph}} \tag{4.45}$$

where N_{ph} is the photon density inside the cavity and is related to the photon density outside the cavity by equation 4.42. The subscript m is dropped from N_{ph} because equation 4.45 applies to any of the lasing modes. The spontaneous emission rate; R_{sp}, can be obtained by the following expression which relates the gain spectrum to the spontaneous emission spectrum [71]

$$R_{sp}(\omega) = n_{sp}(\omega)\ g(\omega)\frac{c}{n_g} \tag{4.46}$$

where $n_{sp}(w)$ is the spontaneous photon emission factor which is defined [65] as the ratio of the spontaneous emission rate to the stimulated emission rate.

$$n_{sp}(\omega) = \left[1 - \exp\left(\frac{h\omega - E_{fc} + E_{fv}}{kT}\right)\right]^{-1} \tag{4.47}$$

where E_{fc} and E_{fv} are the conduction band and valence band quasi Fermi levels. From equation 4.47 it can be seen that the spontaneous emission factor expression predicts that the linewidth narrows with decreasing temperature. Equation 4.45 gives a formula for the laser linewidth, however for practical purposes, it is necessary to write this expression in terms of measurable quantities. Beginning with equation 4.45 it can be proceeded by replacing the intra cavity photon density with P_{out}; the output power from a single facet. This will result in

$$\Delta f = \frac{h\upsilon(c/n_g)\ \alpha_m}{8\pi P_{out}} R_{sp} \tag{4.48}$$

Using equation 4.46 the spontaneous emission rate; R_{sp}, can be related to the gain g, using the spontaneous emission factor n_{sp}, defined in 4.47. This gives the following expresion

$$\Delta f = \frac{h\upsilon}{8\pi P_{out}} \left(\frac{c}{n_g}\right)^2 \alpha_m \, n_{sp} \, g \qquad (4.49)$$

At or above threshold the value of gain is the same as the loss level and this results in

$$\Delta f = \frac{h\upsilon}{8\pi P_{out}} \left(\frac{c}{n_g}\right)^2 \alpha_m \left(\alpha_m + \alpha_{int}\right) n_{sp} \qquad (4.50)$$

where as mentioned before a_m is the loss due to mirror facets and is related to the mirror reflectivity R, and the cavity length L, as $a_m=(1/L)\ln(1/R)$. Substituting the value for a_m in equation 4.50 gives

$$\Delta f = \frac{h\upsilon}{8\pi P_{out}} \left(\frac{c}{n_g}\right)^2 \frac{1}{L^2} \left[\ln\left(\frac{1}{R}\right) + L\alpha_{int}\right] \left(\ln\frac{1}{R}\right) n_{sp} \qquad (4.51)$$

Rearranging and simplifying equation 4.51 results in the final expression for the laser linewidth. The predicted linewidth due to quantum phase fluctuations is given by the modified Schawlow-Townes relation [72] as

$$\Delta f = \frac{h\upsilon}{8\pi P_{out}} \left(\frac{c}{n_g L}\right)^2 (\ln R) \left[\ln R - L\alpha_{int}\right] n_{sp} \qquad (4.52)$$

This equation shows that the spectral width of the diode laser increases linearly with the reciprocal output power so that the linewidth-power product (Df)(P_{out}) is constant.

It was mentioned earlier that external optical feedbacks caused by reflections of light back into the laser diode can result in a reduction of the linewidth at the cost of increased sensitivity to mechanical vibrations. This effect has been taken advantage of in order to fabricate the so called external-cavity laser diodes [69] in which through the application of an external cavity light is deliberately reflected back into the laser . From equation 4.45 it is clear that the linewidth is dependent on the spontaneous emission rate R and the intra cavity photon density N_{ph}. In external cavity laser diodes the cavity length is essentially increased without an increase in the length of the active region. This means that the intra cavity photon density N_{ph} into a mode is increased while the spontaneous emission rate R remains unchanged. As a result the fundamental linewidth will be reduced.

4.4.7 Linewidth enhancement factor

The first careful measurement of the linewidth of an injection laser versus the output power was performed in 1981 by M. Fleming and A. Mooradian at the M.I.T. Lincoln Laboratory [65]. Their measurements showed that the line broadening mechanisms for diode lasers are more complex than predicted by the modified Schawlow-Townes relation; given by equation 4.45 or 4.52. The experimentally obtained value for the linewidth was larger than predicted by the Schawlow-Townes relation. At the time Fleming and Mooradian could not explain this unexpected behavior, however later on this discrepancy was explained by C. Henry [66] to be due to the variation of the real part of the refractive index with increasing carrier density. Henry said that fluctuations in the phase of the optical field result in linewidth broadening. These fluctuations are induced by random spontaneous emission events. As a result, in order to get a correct match between the experimental results and the theoretical prediction the modified Schawlow-Townes relation has to be multiplied by the correction factor $(1+b_c^2)$ where b_c is referred to as the enhancement factor and is much smaller than 1 for laser other than the semiconductor lasers. It is basically defined as the ratio of change of the real part of the refractive index to the change in the imaginary part of the refractive index. For InGaAsP lasers emitting at 1.3 μm wavelength bc is typically about 5 [62]. Incorporating this enhancement factor in equations 4.45 and 4.52 will result in expressions that correctly predict the outcome of the experimental results. These are given as

$$\Delta f = \frac{R_{sp}}{4\pi P_{out}}\left(1 + \beta_c^{\,2}\right) \tag{4.53}$$

$$\Delta f = \frac{h\upsilon}{8\pi P_{out}}\left(\frac{c}{n_g L}\right)^2 (\ln R)\left[\,\ln R - L\alpha_{int}\right](n_{sp})\left(1 + \beta_c^{\,2}\right) \tag{4.54}$$

Equation 4.54 shows the dependence of the laser linewidth on various parameters. However due to the limited wavelength resolution of the spectrum analyzer used in these series of experiments it was not possible to obtain a precise experimental value for the linewidth.

4.4.8 Effects of temperature on the longitudinal spectrum

As the temperature increases the peak of the gain curve shifts to longer wavelengths resulting in a shift in the laser output spectrum. The position of the longitudinal modes will also change due to changes in the optical path length caused by variations in the index of refraction and the actual temperature induced changes in the cavity length L. The situation is very complex because the peak of the gain curve shifts towards shorter wavelengths with increasing external pump current which gives rise to an increase in carrier density. But an increase in the pump current is usually accompanied with an increase in the temperature of the device which, as mentioned, has an opposite effect on the wavelength. Consequently the group of modes will seem to be moving within their spectral envelope. Depending on the exact numerical value of the temperature the position of the main mode may or may not coincide with the gain peak. The wavelength shift of InGaAsP lasers emitting around 1.3 μm has been shown experimentally [73] to be in the order of 0.2 nm per degree Celsius. If the spectrum looks quite symmetrical it implies that the primary cavity mode is aligned with the gain peak. This is obviously not the case of the spectrum shown in figure 4.11, but it can be the case through careful tailoring of the spectrum with temperature modifications.

Another important effect of the temperature is the influence it has on the spectral linewidth of the laser. From equation 4.45 and 4.47 it can be seen that the linewidth of the laser increases with increasing temperatures in addition to its increase with increasing reciprocal power such as predicted by the modified Schawlow-Townes relation and shown experimentally [74].

4.5 Observation of the near field emission pattern

The near field emission pattern of the laser was observed qualitatively in order to determine the precise light emitting area of the front mirror facet. In order to make this observation a microscope objective was used to focus the infrared radiation onto the optical element of a Hamamutsu lead sulfite camera. The camera was connected to a black and white monitor for observation purposes and to a Sony thermal imaging printer for recording. In addition the signal generated by the camera is processed through a video analyzer prior to being pictured on the monitor. Through the video analyzer it is possible to measure the relative intensity of the light along a prescribed line and thus accurately measure the relative light intensity profile along the front mirror facet of the laser. In this manner any sign of inhomogeneity such as filamentation effects is easily detected and recorded. Since the infrared camera can easily be saturated at high light intensity inputs a filter holder has been installed between the microscope objective and the camera. If necessary neutral density filters can be placed there to attenuate the input light. Figure 4.13 shows the experimental setup used to accomplish this task. Figure 4.14 shows an example of the near field emission pattern of a laser diode.

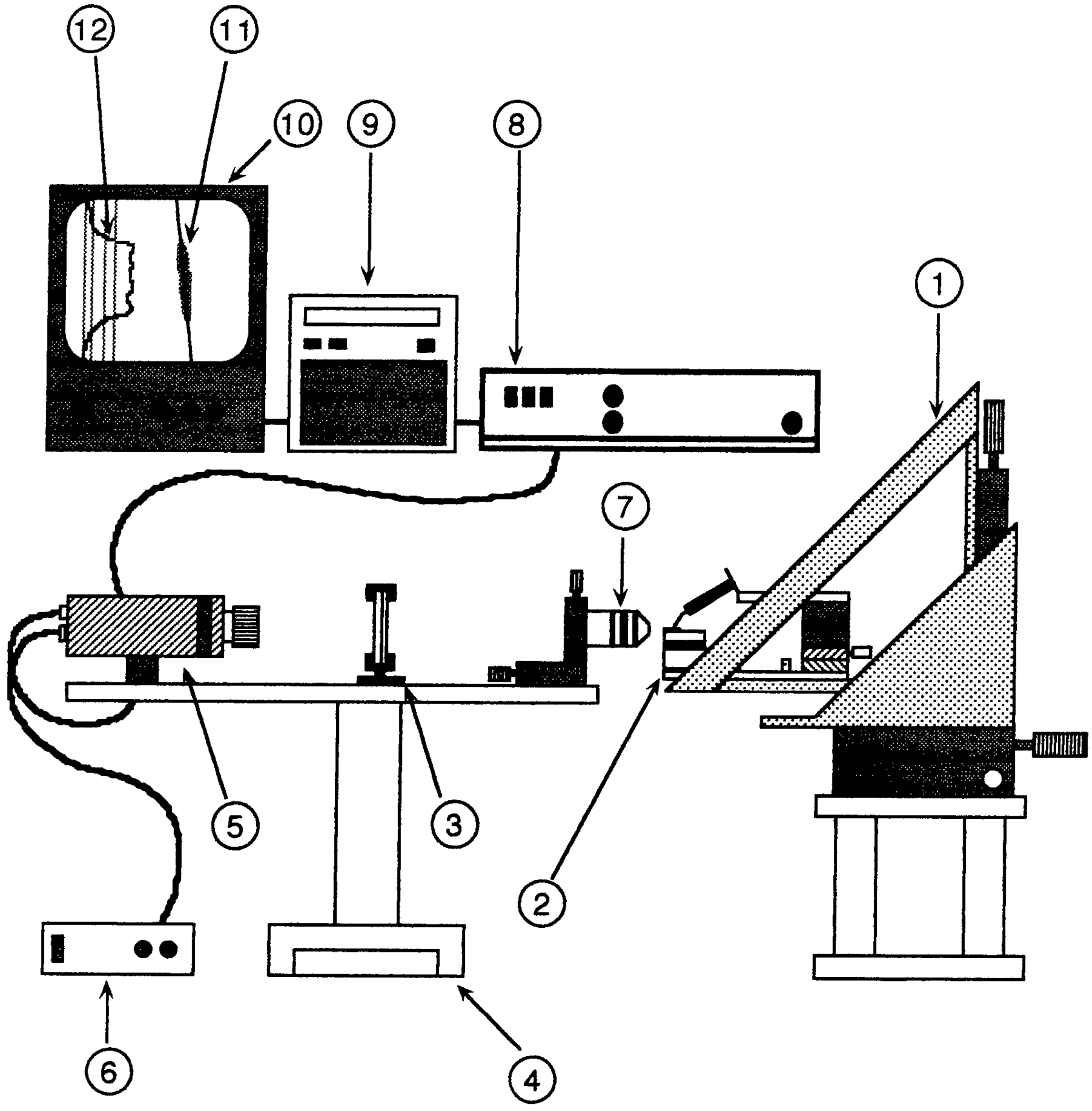
12
11
10
9
8
1
7
5
3
2
6
4

Figure 4.13 Experimental setup for observation of laser diode near field emission pattern and the list of components.

Figure 4.13 continued

1. Support brackets for holding the laser probe station and equipped with xyz translation stages
2. Laser probe station with the heatsink and thermoelectric cooler system
3. Neutral density filters and filter holder
4. Rail slide for removing the near field pattern measurement system out of the way when not in use
5. Infrared camera
6. Camera power supply and controller box
7. Lens objective with translation stages used for focusing
8. Video analyzer
9. Thermal printer
10. Black and white monitor
11. Picture of light emitting area of the front mirror facet of the laser diode
12. Near field intensity profile generated by the video analyzer

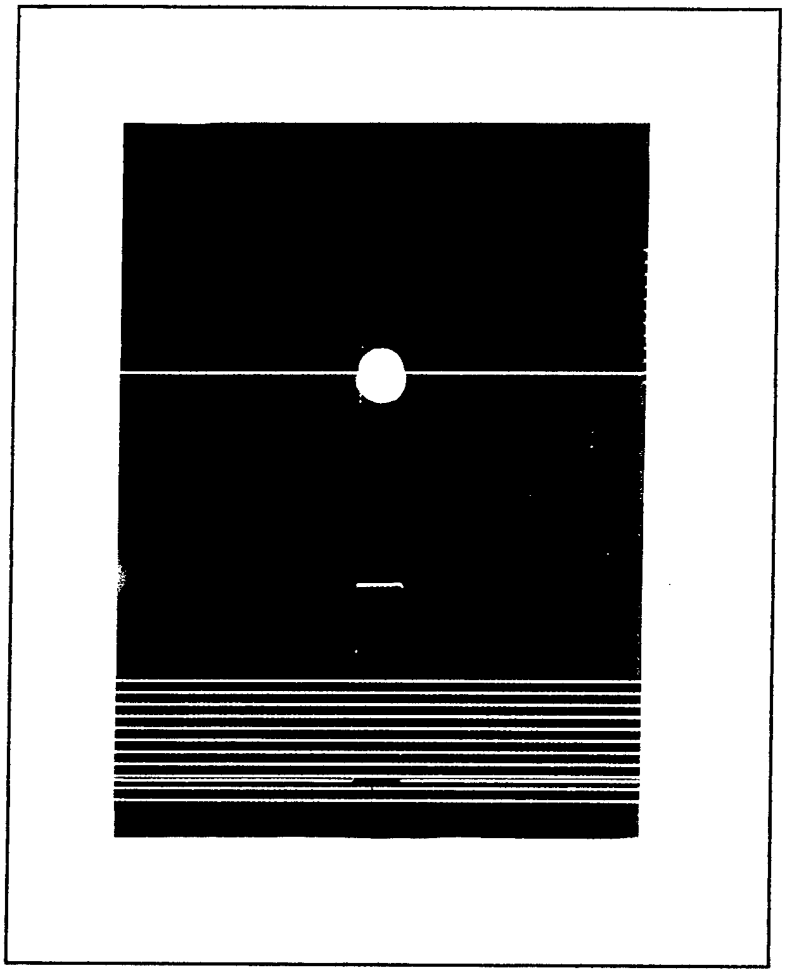

Figure 4.14 Stimulated emission near field pattern of a 1.3 μm laser. The intensity profile is measured along the line passing through the emission pattern. The position and the tilt of this line can be adjusted using the video analyzer.

Summary

The accomplishments of this contract can be classified in two major milestones as follows:

Material growth on Si substrates:

- Growth of high quality GaAs, GaInP, GaInAsP films for 1.3 μm emission wavelength
- Growth of double heterostructure GaInAsP/InP layers
- GaAs buffer layer FWHM decreased bellow 200 arcsec;
- InGaAsP/GaAs superlattices utilizing quaternary materials with different composition are realized;
- InGaAsP/InGaP superlattices utilizing quaternary materials with different composition are realized;
- development of chemical revelation method for studying the interface properties and defect density of buffer layers and superlattices implemented in them;
- photoluminescence and X-ray studies of the interface defect formation and defect propagation;
- optimized GaAs buffer thickness for minimal thermal stress and crack formation.

Processing and device fabrication on Si substrates:

- etching methods for dual channel and ridge-waveguide structure developed;
- photolithography methods for wet chemical etching processes for ridge-waveguide structure developed;
- SiO_2 pasivation by plasma-enhanced CVD developed;
- photolithography methods for window-openings in SiO_2 for RIE developed;
- improved contact system and thermal annealing procedure;
- high yield cleaving method developed;
- laser die bonding to heatsinks developed;
- wire bonding of laser diodes developed
- accomplish short-time CW laser operation at 1.3 μm

It was mentioned in the introduction that the ultimate goal is the realization of OptoElectronic Integrated Circuits on Si substrates. In this way it is possible to combine the III-V photonic semiconductor technology with the already well established and mature Si electronic integrated circuits. The first task towards the achievement of this final goal is the successful development of a laser device grown on a Si substrate in a simple and reproducible manner. However, the heteroepitaxy of III-V material on Si is not an easy task. The problems associated with the growth of photonic devices on Si were addressed in chapter 1.

As part of this work a low pressure metalorganic vapor phase epitaxy machine had to be setup and prepared for the growth of a variety of laser structures including the high power aluminum free systems used in the fabrication of lasers diodes emitting at the wavelengths of 0.98 μm and 0.808 μm.

Chapter 2 outlines the optimum growth parameters for the growth of a InGaAsP / InP double heterostructure on Si substrate without the use of a superlattice layer. The epitaxial layers were grown on (100) Si coated with GaAs. The growth process was carried out at 76 Torr in a horizontal MOCVD reactor with a substrate temperature of 550 ^{o}C. Trimethylindium and Triethylgallium were used as sources of In and Ga. Pure arsine (AsH_3) and phosphine (PH_3) were used as the sources of As an P. Silane (SiH_4) was used as the n-type dopant while diethylzinc (DEZn) was used as p-type dopant. Hydrogen (H_2) was used as the carrier gas.

The material characterization results are also presented and analyzed in chapter 2. The quality of the crystal structure and the lattice matching condition to InP of the InGaAs contact layer and InGaAsP active layer was inspected from the x-ray diffraction pattern of the sample. This spectrum indicated a FWHM for the (004) InGaAsP/InP/InGaAs epilayers of 441 arc seconds. Other material characterization methods included doping profile analysis and photoluminescence measurements done at temperatures ranging from 4 K up to 300 K. The room temperature photoluminescence showed signs of tight carrier confinement and it peaked at 1.35 μm with a FWHM of about 75 meV.

Once the quality of the material was assessed and it was determined that the material was of a device quality a laser diode had to be processed. The details of the laser diode processing and fabrication procedures are given in chapter 3. These include the procedures used to fabricate broad area lasers with and without Schottky contacts, the use of the liftoff process, and the details of the process followed in the fabrication of double channel ridge structures. Different steps of lapping, polishing, annealing, scribing, and cleaving of the laser diodes grown on Si substrate have been explained and the problems involved have been discussed. The fact that Si does not exhibit any clear cleavage plane makes the fabrication of laser diodes on Si particularly difficult. These problems have been overcome successfully. In addition the development of heat sink and laser diode bonding technology has been presented in detail. The procedures set during the development of this technology have even resulted in successful packaging of high power 808 nm lasers with continuous wave output power in excess of 1 Watt per facet.

Presented in chapter 4 are the laser characterization results and the experimental systems used to obtain the measurements. The results include output power measurement results of lasers operating under pulse condition, spectrum analysis measurements, determination of characteristic temperature of the laser diodes, and near field emission pattern. The lasers, which had 20 μm wide stripes, were emitting at a wavelength of 1.35 μm. Output power of over 200 mW per facet at room temperature was achieved for a 170 μm. cavity device with an external quantum efficiency of 23 %. The threshold current density of a 350 μm cavity length device was 9.8 kA/cm^2 and the characteristic temperature was 66 K. From data indicating the cavity length dependence of the inverse external differential quantum efficiency the extrapolated internal quantum efficiency of these lasers was 33 % and the internal loss was 39 cm^{-1}. Conventional theoretical models were then used in chapter 4 to study and explain the behavior of the lasers tested.

This work contributes a firm ground towards the realization of future OEIC's. The immediate step following this work is the achievement of continuous wave operation of this type of laser through improvement of both material quality and processing technology. Also in order to completely eliminate the problems associated with cleaving of a laser grown on Si it is necessary to process horizontal cavity surface emitting lasers with micro mirrors fabricated on them using the technique of reactive ion beam etching. Since the intention is to grow these lasers monolithically on integrated circuits it is necessary to design their structure in such manner as to be able to make both n type and p type contacts to the laser from the same direction. This will also eliminate the need to lap the substrate and thus the laser can be grown monolithically over integrated circuits.

Upon the accomplishment of this contract, several transition of personal have gone to industry:

- Emil Kolev - Spectra Diode Labs
- Xiaoguang He - Optopower
- Ivan Eliashevich - Emcore

References

[1] A. P. Bogatov, L. M. Dolginov, P. G. Eliseev, M. G. Mil'vidiskii, B. N. Sverdlov, and E. G. Shevchenko, " Radiative characteristics of InP-GaInPAs laser heterostructures, " Sov. Phys. Semicond. 9, 10, pp. 1282-1285 (1976).

[2] J. J. Hsieh, J. A. Rossi, and J. P. Donnelly, " Room-temperature cw operation of GaInAsP/InP double heterostructure diode lasers emitting at 1.1 μm, " Appl. Phys. Lett. 28, 12, pp. 709-710 (1976).

[3] K. Oe, S. Ando, and K. Sugiyama, " 1.3 μm cw operation of GaInAsP/InP DH diode lasers at room temperature, " Jpn. J. Appl. Phys. 16, 7, pp. 1273-1274 (1977).

[4] W. T. Tsang, F. S. Choa, R. A. Logan, T. Tanbun-Ek, M. C. Wu, Y. K. Chen, A. M. Sergent, and K. W. Wecht, " 1.3 μm InGaAsP/InP multiquantum well buried heterostructure grown by chemical-beam epitaxy, " Appl. Phys. Lett. 59, 24, pp. 3084 -3086 (1991).

[5] D. Z. Garbuzov, I. E. Berishev, Yu. V. Il'in, N. D. Il'inskaya, A. V. Ovchinnikov, N. A. Pikhtin, N. L. Rassudov, and I. S. Tarasov, " Improvement in the burial process and fabrication of single-mode buried InGaAsP/InP(l=1.3 μm) lasers with an output power of 160 mW, " Sov. Phys. Semicond, 25, 8, pp. 852-854 (1991).

[6] A. Kasukawa, I. J. Murgatroyd, Y. Imajo, N. Matsumoto, T. Fukushima, H. Okamoto, and S. Kashiwa, " High quantum efficiency, high output power 1.3 μm GaInAsP buried graded-index separate-confinement-heterostructure multiple quantum well (GRIN-SCH-MQW) laser diodes, " Jpn. J. Appl. Phys. 28, pp. L661-L663 (1989).

[7] H. Horikawa, H. Wada, T. Matsui, T. Yamada, Y. Ogawa, and Y. Kawai, " High-power and high-speed semi-insulating blocked V-grooved inner-stripe lasers of 1.3 μm wavelength fabricated on p-InP substrates, " Appl. Phys. Lett. 54, 12, pp. 1077-1079 (1989).

[8] D. Coblentz, T. Tanbun-Ek, R. A. Logan, A. M. Sergent, S. N. G. Chu, and P. S. Davisson, " Strained multiple quantum well lasers emitting at 1.3 μm grown by low-pressure metalorganic vapor phase epitaxy, " Appl. Phys. Lett. 59, 4, pp. 405-407 (1991).

[9] N. Bouadma, C. Kazmierski, and J. Semo, " Over 245 mW 1.3 μm buried ridge stripe laser diodes on n-substrate fabricated by the reactive ion beam etching technique, " Appl. Phys. Lett, 59, 1, pp. 22-24 (1991).

[10] M. Razeghi, R. Blondeau, K. Kazmierski, M. Krakowski, and J. P. Duchemin, " Very low threshold buried ridge structure lasers emitting at 1.3 μm grown by low pressure metalorganic chemical vapor deposition, " Appl. Phys. Lett. 46, 2, pp. 131-133 (1985).

[11] M. Razeghi, " Recent advanced in III-V compounds on silicon " Prog. Crystal Growth, and Charact. 19, pp. 21-37 (1989).

[12] M. Razeghi, F. Omnes, M. Defour, and Ph. Maurel, " High-quality GaInAsP/InP heterostructures grown by low-pressure metalorganic chemical vapor deposition on silicon substrates, " Appl. Phys. Lett. 52, 3, pp. 209-211 (1988).

[13] R. Houdre and H. Morkoc, " Properties of GaAs on Si grown by molecular beam epitaxy, " Critical Reviews in Solid State Materials Sciences, 16, 2, pp. 91-114 (1990).

[14] O. Aina, M. Mattingly, J. R. Bates A. Coggins, J. O'Connor, S. K. Shastry, J. P. Salerno, A. Davis, J. P. Lorenzo, and K. S. Jones, " High-purity InP grown on Si by organometallic vapor phase epitaxy " Appl. Phys. Lett. 58, 14, pp. 1554-1556 (1991).

[15] H. K. Choi, R. Hull, H. Ishiwara, and R. J. Nemanich, " Heteroepitaxy on Si: Fundamentals, Structures, and Devices, " Materials Research Society Symposium Proceedings, Volume 116, (1988).

[16] M. Razeghi, M. Defour, F. Omnes, Ph. Maurel, J. Chazelas, and F. Brillouet, " First GaInAsP-InP double-heterostructure laser emitting at 1.27 μm on a silicon substrate, " Appl. Phys. lett. 53, 9, pp. 725-727 (1988).

[17] M. Razeghi, M. Defour, R. Blondeau, F. Omnes, P. Maurel, O. Acher, F. Brillouet, J. C. C. Fan, and J. Salerno, " First cw operation of a $Ga_{0.25}In_{0.75}As_{0.5}P_{0.5}$-InP laser on a silicon substrate, " Appl. Phys. Lett. 53, 24, pp. 2389-2390 (1988).

[18] M. Sugo, H. Mori, M. Tachikawa, Y. Itoh, and M. Yamamoto, " Room-temperature operation of an InGaAsP double-heterostructure laser emitting at 1.55 μm on a Si substrate, " Appl. Phys. Lett. 57, 6, pp. 593-595 (1990).

[19] M. Sugo, H. Mori, Y. Itoh, Y. Sakai, and M. Tachikawa, " 1.5 μm-long-wavelength multiple quantum well laser on Si substrate, " J. Appl. Phys. 12B, pp. 3876 -3878 (1991).

[20] K. Mobarhan, C. Jelen, E. Kolev, and M. Razeghi, " Optical, electrical, and structural characterization of GaInAsP/InP layers grown on silicon substrate for 1.35 μm laser applications, " Materials Research Society Symposium Proceedings, Volume 281, pp. 369-374 (1993).

[21] K. Mobarhan, C. Jelen, E. Kolev, and M. Razeghi, " GaInAsP / InP 1.35 μm double heterostructure laser grown on silicon substrate by metalorganic chemical vapor deposition, " J. Appl. Phys. 74, 1, pp. 743-745 (1993).

[22] Y, Shinoda, T. Nishioka, and Y. Ohmachi, " GaAs light emitting diodes fabricated on SiO_2/Si wafers, " Jpn. J. Appl. Phys. 22, 7, pp. L450-L451 (1983).

[23] T. H. Windhorn, G. M. Metze, B-Y. Tsaur, and J. C. C. Fan. " AlGaAs double-heterostructure diode lasers fabricated on a monolithic GaAs/Si substrate, " Appl. Phys. Lett. 45, 4, pp. 309-311 (1984).

[24] H. K. Choi, C. A. Wang, and N. H. Karam, " GaAs-based diode lasers on Si with increased lifetime obtained by using strained InGaAs active layer, " Appl. Phys. Lett. 59, 21, pp. 2634-2635 (1991).

[25] J. Paslaski, H. Z. Chen, H. Morkoc, and A. Yariv, " High-speed GaAs p-i-n photodiodes grown on Si substrate by molecular beam epitaxy, " Appl. Phys. Lett. 52, 17, pp. 1410-1412 (1988).

[26] H. K. Choi, B-Y. Tsaur, G. M. Metze, G. W. Turner, and J. C. C. Fan, " GaAs MESFETs fabricated on monolithic GaAs/Si substrates, " IEEE Electron Device Lett. EDL-5, 6, pp. 207-208 (1984).

[27] R. Fischer, T. Henderson, J. Klem, W. T. Masselink, W. Kopp, H. Morkoc, and C. W. Litton, " Characteristics of GaAs/AlGaAs MODFETs grown directly on (100) silicon, " Electron Lett. 20, 22, pp. 945-947 (1984).

[28] R. Fischer, C. K. Peng, J. Klem, T. Henderson, and H. Morkoc, " III-V semiconductors on Si substrates: new directions for heterojunction electronics, " Solid State Electronics 29, 2, pp. 269-271 (1986).

[29] R. P. Gale, J. C. C. Fan, B-Y. Tsaur, G. W. Turner, and F. M. Davis, " GaAs shallow-homojunction solar cells on Ge-coated Si substrates, " IEEE Elect. Dev. Lett. EDL-2, 7, pp. 169-171 (1981).

[30] W. Dobbelaere, D. Huang, M. S. Unlu, and H. Morkoc, " AlGaAs/GaAs multiple quantum well reflection modulators grown on Si substrates, " Appl. Phys. Lett. 53, 2, pp. 94-96 (1988).

[31] Y. S. Kim, S. S. Lee, R. V. Ramaswamy, S. Sakai, Y. C. Kao, and H. Shichijo, " Low-pass GaAs/AlGaAs optical waveguides and phase modulator on silicon substrate grown by molecular beam epitaxy, " Appl. Phys. Lett. 56, 9, pp. 802-804 (1990).

[32] M. Razeghi, R. Blondeau, M. Defour, F. Omnes, P. Maurel, and F. Brillouet, " First room-temperature cw operation of a GaInAsP/InP light-emitting diode on a silicon substrate, " Appl.. Phys. Lett. 53, 10, pp. 854-855 (1988).

[33] M. Razeghi, F. Omnes, R. Blondeau, Ph. Maurel, M. Defour, O. Acher, E. Vassilakis, G. Mesquida, J. C. C. Fan, and J. P. Salerno, " A high quantum efficiency GaInAs-InP photodetector-on-silicon substrate, " J. Appl. Phys. 65, 10, pp. 4066-4068 (1989).

[34] Yamaguchi M., A. Yamamoto, Y. Itoh, and T. Nishioka. Proc. 19th. IEEE Photovoltaic Specialists Conf., 267 (1987).

[35] T. Makimoto, K. Kurishima, T. Kobayashi, and T. Ishibashi, " InP/InGaAs double heterojunction bipolar transistors grown on Si, " Jap. J. Appl. Phys. 30, 12B, pp. 3815-3817 (1991).

[36] O. Aina, M. Serio, M. Mattingly, J. O'Connor, S. K. Shastry, D. S. Hill, J. P. Salerno, and P. Ferm, " High-speed InP/GaInAs heterojunction phototransistor on InP-on-Si grown by metalorganic vapor phase epitaxy, " Appl. Phys. Lett. 59, 3, pp. 268-270 (1991).

[37] K. Adomi, J.-I. Chyi, S. F. Fang, T. C. Shen, S. Strite, and H. Morkoc, " Molecular beam epitaxial growth of GaAs and other compound semiconductors, " Thin Solid Films, 205, pp. 182-212 (1991).

[38] N. Chand, J. Allam, J. M. Gibson, F. Capasso, F. Beltram, A. T. Macrander, A. L. Hutchinson, L. C. Hopkins, C. G. Bethea, B. F. Levine, and A. Y. Cho, " GaAs avalanche photodiodes and the effect of rapid thermal annealing on crystalline quality of GaAs grown on Si by molecular-beam epitaxy, " J. Vac. Sci. Technol.. B5, 3, pp. 822-826 (1987).

[39] S. Wakabayashi, K. Mutoh, M. Nakajima, and Y. Toyoda, " InGaAsP/InP horizontal cavity surface-emitting lasers radiating in two opposite directions, " Appl. Phys. Lett. 61, 13, pp. 1499-1501 (1992).

[40] G. J. van Gurp, J. M. Jacobs, J. J. M. Binsma, and L. F. Tiemeijer, " InGaAsP/InP lasers with two reactive-ion-etched mirror facets, " Jpn. J. Appl. Phys. 28, 7, pp. L1236 - L11238 (1989).

[41] K. Mutoh, S. Wakabayashi, Y. Toyoda, and M. Nakajima, " Simultaneous fabrication of vertical and 45° mirrors of InP for surface-emitting lasers using inclined Cl ion beams, " Jpn. J. Appl. Phys. 30, pp. 67-71, (1991).

[42] H. Saito and Y. Noguchi, " A reflection-type surface-emitting 1.3 μm InGaAsP/InP laser array with microcoated reflector, " Jpn. J. Appl. Phys. 28, pp. L1239-1241 (1989).

[43] A. R. Adams, M. Asada, Y. Suematsu, and S. Arai, " The temperature depenedence of the efficiency and threshold current of $In_{1-x}Ga_xAs_yP_{1-y}$ lasers related to intervalence band absorption, " Jpn. J. Apll. Phys. 19, 10, pp. L621-624 (1980).

[44] M. Asada, and Y. Suematsu, " Measurement of spontaneous emission efficiency and nonradiative recombinations in 1.58 μm wavelength GaInAsP/InP crystals, " Appl. Phys. lett. 41, 4, pp. 353-355 (1982).

[45] M. Asada, A. R. Adams, K. E. Stubkjaer, Y. Suematsu, Y. Itaya, and S. Arai " The temperature dependence of the threshold current of GaInAsP/InP DH lasers, " IEEE J. of Quantum Electron. QE-17, 5, pp. 611-618 (1981).

[46] M. Asada and Y. Suematsu, " The effects of loss and nonradiative recombination on the temperature dependence of threshold current in 1.5-1.6 μm GaInAsP/InP lasers, " IEEE J. Quantum Electron. QE-19, 6, pp. 917-923 (1983).

[47] N. K. Dutta and R. J. Nelson, " The case for Auger recombination in $In_{1-x}Ga_xAs_yP_{1-y}$, " J. Appl. Phys. 53, 1, pp. 74-92 (1982).

[48] Beattie, A. R., and P. T. Landsberg. Proc. R. Soc. London Ser. A 249, 16 (1959).

[49] P. J. Anthony and N. E. Schumaker, " Ambipolar transport in double heterostructure injection lasers, " IEEE Electron Device Lett. EDL-1, 4, pp. 58-60 (1980)

[50] A. Sugimura, " Band-to-band Auger recombination effect on InGaAsP laser threshold, " IEEE J. Quantum Electron. QE-17, 5, pp. 627-634 (1981).

[51] A. Haug, " Theory of the temperature dependence of the threshold current of an InGaAsP laser, " IEEE J. Quantum Electron. QE-21, 6, pp. 716-718 (1985).

[52] Y. Horikoshi, and Y. Furukawa, " Temperature sensitive threshold current of InGaAsP-InP double heterostructure lasers, " Jpn. J. Appl. Phys. 18, 4, pp. 809-815 (1979).

[53] C. B. Su, J. Schlafer, J. Manning, and R. Olshansky, " Measurement of radiative recombination coefficient and carrier leakage in 1.3 μm InGaAsP lasers with lightly doped active layers, " Electron. Lett. 18, 25, pp. 1108-1110 (1982).

[54] G. H. B. Thompson, and G. D. Henshall, " Nonradiative carrier loss and temperature sensitivity of threshold in 1.27 μm (GaIn)(AsP)/InP D.H. lasers, " Electron Lett. 16, 1, pp. 42-44 (1980).

[55] N. K. Dutta, ,and R. J. Nelson, " Temperature dependence of threshold of InGaAsP/InP double heterostructure lasers and Auger recombination, " Appl. Phys. Lett. 38, 6, pp. 407-409 (1981).

[56] Y. Horikoshi, " Temperature dependence of laser threshold current, " Review article in " GaInAsP Alloy Semiconductors " edited by T. P. Pearsall, John Wiley & Sons Ltd., pp. 379-411 (1982).

[57] N. G. Nilsson, " Emperical approximations for the Fermi energy in a semiconductor with parabolic bands, " Appl. Phys. Lett. 33, 7, pp. 653-654 (1978).

[58] N. K. Dutta and R. J. Nelson, " Temperature dependence of the lasing characteristics of the 1.3 μm InGaAsP-InP and GaAs-$Al_{0.36}Ga_{0.64}As$ DH lasers, " IEEE J. Quantum Electron. QE-18, 5, pp. 871-878 (1982).

[59] T. R. Chen, B. Chang, L. C. Chiu, K. L. Yu, S. Margalit, and A. Yariv, " Carrier leakage and temperature dependence of InGaAsP lasers, " Appl. Phys. Lett. 43, 3, pp. 217-218 (1983).

[60] P. J. Anthony, and N. E. Schumaker, " Temperature dependence of the lasing threshold current of double heterostructure injection lasers due to drift current loss, " J. Appl. Phys. 51, 9, pp. 5038-5040 (1980).

[61] M. Yano, Y. Nishitani, K-I. Hori, and M. Takusagawa, " Temperature characteristics of double-carrier-confinement (DCC) heterojunction InGaAsP(l=1.3 μm)/InP lasers, " IEEE J. Quantum Electron. QE-19, 8, pp. 1319-1326 (1983).

[62] G. P. Agrawal and N. K. Dutta, " Semiconductor lasers " 2nd edition, Van Nostrand Reinhold, New York (1993).

[63] P. Chandra, L. A. Coldren, and K. E. Strege, " Refractive index data from $Ga_xIn_{1-x}As_yP_{1-y}$ films, " Electron. Lett. 17, pp. 6-7 (1981).

[64] A. L. Schawlow and C. H. Townes, " Infrared and optical masers, " Phys. Rev. 112, 6, pp. 1940-1949 (1958).

[65] M. W. Fleming, and A. Mooradian, " Fundamental line broadening of single-mode (GaAl)As diode lasers, " Appl. Phys. Lett. 38, 7, pp. 511-513 (1981).

[66] C. H. Henry, " Theory of the linewidth of semiconductor lasers " IEEE J. Quantum Electron. QE-18, 2, pp. 259-264 (1982).

[67] C. H. Henry, " Phase noise in semiconductor lasers, " J. Lightwave Technol. LT-4, 3, pp. 298-311 (1986).

[68] A. Mooradian, " Laser linewidth " Physics Today, pp. 43-48, May (1985).

[69] M. Osinski, and J. Buus, " Linewidth broadening factor in semiconductor lasers-An overview, " IEEE J. Quantum Electron. QE-23, 1, pp. 9-28 (1987).

[70] M. Lax, " Classical noise v. noise in self-sustained oscillators, " Phys. Rev. 160, 2, pp. 290-307 (1967).

[71] C. H. Henry, " Phase noise in semiconductor lasers, " J. Lightwave Tech. 4, 3, pp. 298-311 (1986).

[72] M. Lax, in " Physics of Quantum Electronics " edited by P. L. Kelly, M. Lax, and P. E. Tannenwald, p. 735, McGraw-Hill, New York, (1966).

[73] T. P. Lee, C. A. Burrus, J. A. Copeland, A. G. Dentai, and D. Marcuse, " Short-cavity InGaAsP injection lasers: dependence of mode spectra and single-longitudinal-mode power on cavity length, " IEEE J. Quantum Electron. QE-18, 7, pp. 1101-1112 (1982).

[74] D. Welford and A. Mooradian, " Output power and temperature dependence of the linewidth of single frequency cw (GaAl)As diode lasers, " Appl. Phys. Lett. 40, 10, pp. 865-867 (1982).

[75] N. K. Dutta, " Calculated temperature dependence of threshold current of GaAs-$Al_xGa_{1-x}As$ double heterostructure lasers, " J. Appl. Phys. 52, 1, pp. 70-73 (1981).

Appendix A

List of Symbols

J	Current density
q	Electron charge
d	Active layer thickness
$R(n)$	Recombination rate as a function of carrrier density
n	Carrier density
A_{nr}	Nonradiative recombination coefficient
B	Spontaneous radiative recombination coefficient
C	Nonradiative Auger recombination coefficient
R_{st}	Net rate of stimulated emission
N_{ph}	Photon density
g	Optical gain parameter
c	Speed of light
n_p	Phase index of refraction
n_g	Group index of refration
J_{th}	Threshold current density
n_{th}	Carrier density at threshold
L	Cavity length of the laser device
R	Reflectivity of mirror facet
Γ	Confinement factor
α_m	Loss parameter due to the mirrors
α_{int}	Total internal loss parameter
α_{ac}	Active region internal loss parameter
α_{ex}	Cladding region internal loss parameter
A	Gain coefficient

g_p	Peak gain value
n_o	Injected carrier density at which gain takes a non zero value (onset of population inversion).
α_{loss}	Sum of a_{int} and a_m
α_{in}	Absorption of the unpumped material ($a_{in}=An_o$)
τ_e	Carrier lifetime
τ_p	Photon lifetime
η_i	Internal quantum efficiency
P_{out}	Output power of the laser
h	Planck constant
υ	Photon frequency
v_g	Group velocity
V	Total volume of the active region
I_{th}	Threshold current
I	Current
I_L	Leakage current other than heterobarrier leakage
η_d	External differential quantum efficiency
τ_r	Radiative recombination lifetime
τ_{nr}	Nonradiative recombination lifetime
J_o	Threshold current density at 0 K temperature
T	Temperature
T_o	Characteristic temperature of the laser
m_c	Electron mass
k_B	Boltzmann constant
kT	Thermal energy
ΔE_c	Conduction band discontinuity
E_{fc}	Electron quasi Fermi level measured rom the conduction band edge

D_n	Electron diffusivity
μ_n	Electron mobility
E	Electric field
λ_m	Wavelength of mode "m"
λ_o	Wavelength in free space
ω_m	Frequency of mode "m"
$N_{ph(m)}$	Photon density of mode "m"
ω_o	Gain peak frequency
$\Delta\omega_g$	Frequency spread on either side of the gain peak for which gain is positive
$\Delta\omega_L$	Mode spacing frequency
M	Largest integer in the ratio of Dw_g over Dw_L
$\Delta\omega_s$	FWHM of the spectral envelope
δ	The difference between the loss level and peak gain value
$n_{sp}(\omega)$	Spontaneous photon emission factor as a function of w
β_c	Laser linewidth enhancement factor

Appendix B

List of Publications

[1] K. Mobarhan, M. Razeghi, and R. Blondeau, " GaInAs / GaAs / GaInP buried ridge structure single quantum well laser, " Electronics Letters, 28, 16, pp. 1510-1511 (1992).

[2] K. Mobarhan, M. Razeghi, G. Marquebielle, and E. Vassilaki, " High power, 098 μm GaInAs / GaAs / GaInP multiple quantum well laser, " J. Appl. Phys., 72, 9, pp. 4447-4448 (1992).

[3] K. Mobarhan, C. Jelen, E. Kolev, and M. Razeghi, " Optical, electrical, and structural characterization of GaInAsP / InP layers grown on silicon substrate for 1.35 μm laser applications, " Material Research Society Symposium Proceedings, 281, pp. 369-374 (1993).

[4] K. Mobarhan, C. Jelen, E. Kolev, and M. Razeghi, " GaInAsP / InP 1.35 μm double heterostructure laser grown on silicon substrate by metalorganic chemical vapor deposition, " J. Appl. Phys., 74, 1, pp. 743-745, (1993).

[5] J. Diaz, I. Eliashevich, K. Mobarhan, E. Kolev, L. J. Wang, D. Z. Garbuzov, and M. Razeghi" InGaP / InGaAsP / GaAs 0.808 μm separate confinement laser diodes grown by metalorganic chemical vapor deposition, " IEEE Photonics Technology Letters, 6, 2, pp. 132-134 (1994).